Title

Design of Mechanical Programmability for Vibration-actuated Robots and Shape-changing Laminate Structures

Author

Hakes Weston-Dawkes, William

Publication Date

2022

UNIVERSITY OF CALIFORNIA SAN DIEGO

Design of Mechanical Programmability for Vibration-actuated Robots and Shape-changing Laminate Structures

A dissertation submitted in partial satisfaction of the
requirements for the degree Doctor of Philosophy

in

Engineering Sciences (Mechanical Engineering)

by

William Hakes Weston-Dawkes

Committee in charge:

Professor Michael Tolley, Chair
Professor James Friend
Professor Nick Gravish
Professor Ken Loh
Professor Tania Morimoto

2022

The Dissertation of William Hakes Weston-Dawkes is approved, and it is acceptable in quality and form for publication on microfilm and electronically.

University of California San Diego

2022

TABLE OF CONTENTS

LIST OF FIGURES

LIST OF TABLES

ACKNOWLEDGEMENTS

I'd like to thank my advisor, Dr. Michael Tolley for all of the support and guidance he provided me during the research and writing process. Without his help, the completion of my dissertation would not have been possible. He is always willing to to make himself available for help and advice. It has been an unparalleled pleasure to work with and learn from him.

I would also like to express my deepest appreciation to my committee for sparing their invaluable time providing feedback one my thesis. Without my collaborators, the much of this work would not have been possible. They helped with a whole host of things, including assistance with experiments, fabrication, and project conceptualization. Thank you so much Iman Adibnazari, Yi-Wen Hu, Francis Joseph, Ramzi Majit, Esmeralda Ochoa, Aaron Ong, and Jessica Sandoval. In particular, I'm grateful to Dr. Santiago Horgan for providing expert clinical guidance as well as access to the facilities at the Center for the Future of Surgery. In the same vein, Dr. Shanglei Liu and Dr. Jenny Lam were amazing fonts of knowledge with regards to laparoscopic procedures, without their support and insights, the work on the variable-stiffness retractor would not have been possible. I'm also deeply indebted to Mike Everman and Nick Gravish, their engineering intuition and perspectives were instrumental for the work done on vibration-based adhesion. Thanks to Dr. Sanchez for his insights into some of the fundamental fluid mechanics of the adhesive disk.

My labmates, old and new (too many to fully list here, but they know who they are), were not only great company in the lab, but are also some of the most wonderful friends I could ask for. Everyone in the lab was incredibly supportive and made the lab environment a pleasure to be in. Special thanks to: Caleb Christianson, Dylan Drotman, Paul Glick, Saurabh Jadhav, Tom Kalisky, Emily Lathrop, Michael Ishida, Adriane F. Minori, and Ben Shih.

I'd like to acknowledge the assistance provided by the MAE staff (both current and past) who keep the department running smoothly, in particular I'd like to thank Taylor Nelson, Joana Halnez, J.V. Agnew, and Roxanne Vanderheiden for the professionalism and care that they put into their work.

I owe my deepest thanks to my family - my parents, my brothers, my inlaws, my extended family on the west coast, and my wife who have always stood by me and guided me through my career. They have been a source of unrelenting encouragement and support. Words cannot express the gratitude that I owe them.

Last, but never least, I would like to especially thank my wife, Raquel. She has been an amazing source of support and love throughout my degree. Thank you for sharing this journey with me, for helping me brainstorm and reorient my thoughts countless times, and for always being ready to go on a hike.

I would like to acknowledge financial support for this work from the Office of Naval Research and the Powell Fellowship.

Chapter 2, in full, is a reprint of the material as it appears in IEEE/RSJ Internation Conference on Intelligent Robots and Systems (IROS) 2017. Weston-Dawkes, W.P.; Ong, A.C.; Majit, M.R.A.; Joseph, F.; and Tolley, M.T., The dissertation author was the primary investigator and author of this paper.

Chapter 3, in full, is a reprint of the material as it appears in Advanced Intelligent Systems 2021. Weston-Dawkes, W.P.; Everman, M.; Gravish, N.; Tolley, M. T.; The dissertation author was the primary investigator and author of this paper.

Chapter 4, in part, is currently being prepared for submission for publication of the material. Weston-Dawkes, W.P.; Majit, M.R.A.; Sandoval, J.; Ochoa, E.; Liu, S.; Horgan, S.; Tolley, M.T. The dissertation author was the primary investigator and author of this material.

Chapter 5, in part, has been submitted for publication of the material as it may appear in International Design Engineering Technical Conferences & Computers and Information in Engineering Conference, 2022, Weston-Dawkes, W.P.; Tolley, M.T. The dissertation author was the primary investigator and author of this paper.

VITA

2015	Bachelor of Sciences, University of Maryland, College Park
2015–2021	Research Assistant, University of California San Diego
2022	Doctor of Philosophy, University of California San Diego

PUBLICATIONS

Weston-Dawkes W.P., Everman M., Gravish N., Tolley M. T. “Gas-Lubricated Vibration-Based Adhesion For Robotics”, *Advanced Intelligent Systems*, 3:2100001, 2021.

Weston-Dawkes W.P., Ong A.C., Majit M.R.A., Joseph F., and Tolley M.T. “Towards Rapid Mechanical Customization of cm-scale Self-Folding Agents”, in *2017 IEEE/RSJ International Conference on Intelligent Robots and Systems*, Sept 2017, pp. 4312–4318.

Weston-Dawkes W.P., Everman M., Hu Y.W., Gravish N., Tolley M.T. “Vibration-based Adhesion and Locomotion for Wall-Climbing Robots”, *2019 International Design Engineering Technical Conferences & Computers and Information in Engineering Conference*, Aug 2019, IDETC2019-98509

Weston-Dawkes W.P., “Parallelogram Folding of Stick-Slip Legs for Reliable Self-Assembly”, *Folding in Robotics workshop, IROS*, 2017

ABSTRACT OF THE DISSERTATION

Design of Mechanical Programmability for Vibration-actuated Robots and Shape-changing Laminate Structures

by

William Hakes Weston-Dawkes

Doctor of Philosophy in Engineering Sciences (Mechanical Engineering)

University of California San Diego, 2022

Professor Michael Tolley, Chair

Rigid robotic systems struggle to solve problems that require drastic shape changes, possess high environmental uncertainty, and involve direct interaction with humans. The present work investigates four different approaches to designing mechanically reprogrammable robotic systems. The mechanical properties of the four presented systems are controlled by reprogramming their geometry, structural properties, or dynamic properties during operation. The first study explores the potential of vibration-based locomotion in a self-folded robotic system to characterize and achieve controllable locomotion that is easily incorporated into laminate structures. We describe the extension of two-dimensional bristle-bot models to a three-dimensional model that explores parameters that govern linear and angular velocity, and implement a self-folding laminate-manufactured bristle-bot robot. In the second study, we present a new method for achieving controllable adhesion by vibrating a flexible plate near a surface, which generates a strong and controllable normal attraction force while allowing free motion parallel to the surface. Spatial pressure measurements demonstrate that adhesion is localized to the center of the disc. We developed a mobile robot capable of robustly acquiring payloads and adhering to vertical and inverted surfaces. In the third study, we present a variable stiffness surgical retractor that can be folded and inserted into a patient through a small opening, can change to a stiff state and anchor atraumatically to the body to retract an organ, and can be subsequently refolded and removed from the body. We model the variable stiffness mechanism (layer jamming) to predict the maximum load a retractor can support and compare this to experiments. In the fourth study, we present a model to predict the length scales at which jamming contributes to the overall performance of an inflatable beam, serving as a limb of a hybrid hard/soft robot. We measure the performance of prototype jamming limbs in cantilever loading tests, and experimentally test a quadrupedal system, using experiments to inform the design process. Incorporating jamming reinforcement into inflatable beams provides improved stiffness and graceful failure rather than the catastrophic buckling that normally characterizes inflated cylindrical beams. Together, these studies illuminate the exciting potential of mechanically reprogrammable robotic systems composed of laminate structures.

Chapter 1

Introduction

One of the challenges facing traditional robotics is the ubiquitous presence of uncertainty in both the natural and the built environment. Traditionally manufactured rigid robotic systems struggle to solve problems that require compliance/drastic shape changes, possess high environmental uncertainty, and involve close interactions with humans. These challenges have been tackled by advances in compliant mechanism design (replacing discrete mechanisms with flexures), soft robotic design (replacing rigid materials with soft ones), and origami-inspired design (2D fabrication that enables complex 3D behavior). One overarching approach to dealing with uncertainty, that all of these design advances attempt to provide, is to make a robotic system that is capable of adapting to drastically different environmental conditions or operational requirements. This capability, defined here as mechanical reprogrammability, allows a robotic system to change its geometry, structural properties, or dynamic properties to shift between different functional states. Examples of changing geometry might be folding a structure to add stiffness or create complex 3D motion. Changing the structural properties, such as the stiffness of the underlying material, can allow a robotic system to transition from a completely soft state to a very rigid one. Additionally, investigating the dynamic response of a structure or robotic system in different environments can enable completely novel designs and behaviors.

The new design approaches of compliant mechanisms, soft systems, and origami-inspired design have been enabled by the rise of accessibility of digital manufacturing techniques. 3D printers and laser engravers have become more widely available, with the prices of fused deposition modeling (FDM) printers dropping to below one thousand dollars and CO2 laser engravers to several thousand dollars. The wider availability of manufacturing tools has enlarged the design space for researchers in robotics, whose job it is to figure out how to create both new digital manufacturing methodologies and new robotic systems based on these methods. One general methodology, inspired by micro-electromechanical systems (MEMS), is that of laminate manufacturing, which takes advantage of composite design while also leveraging the precision of digital fabrication. Different functional layers (structural, circuit, power, actuation) are separately machined, aligned, and laminated together in a flat sheet. This sheet can then be assembled into a 3D shape via external manipulation or on-board actuation. Laminate manufacturing broadly falls at the intersection of compliant mechanism design, origami-inspired design, and soft robotics.

This thesis presents four projects that apply laminate manufacturing principles to a broad array of design challenges that represent open problems in robotics and beyond. The first project seeks to create new opportunities for robotic swarms, groups of robots used to address distributed problems, by investigating novel vibration-based locomotion strategies on self-folding robots. The objective of the second project was to describe the potential for and limitations of vibration-based adhesion, specifically applied to wall-climbing robots. The third project seeks to augment the capabilities of soft inflatable robotics using jamming techniques based in laminate manufacturing. The final project assesses the design of a variable stiffness retractor for minimally invasive surgery (MIS). In all of these projects, design philosophies borrowed from laminate manufacturing are used to explore the challenges, both explicit and implicit, that exist in the literature.

Mobility and Manufacture of Robotic Swarms

Limitations of most available manufacturing strategies preclude the rapid fabrication of heterogeneous and sizable robotic collectives. 3D printing, while revolutionary for small scale manufacturing, lacks the ability to be truly multi-material (i.e., to print complete robots) and as long as significant human intervention is required to manufacture robots, a truly reactive swarm of robots is out of reach.

Laminate-manufactured self-folding robots [1, 2] have the potential to enable fully automated fabrication of robotic swarms. Previous examples of laminate-manufactured or smart-composite microstructure based robots demonstrate a wide range of locomotion modalities (running [3], crawling [4], flying [5, 6]), showing the versatility of this manufacturing approach. The incorporation of conventional actuators, such as motors, presents a number of challenges for self-folding robots. In contrast, vibration-based locomotion provides a simple and inexpensive planar locomotion modality; actuators, such as eccentric rotating mass (ERM) motors, are self-contained and easily incorporated into laminate structures via adhesives [1].

Existing robotic systems that leverage vibration-based locomotion such as Kilobot [7, 8] and robots demonstrated in [9] have successfully demonstrated the ability to deterministically control the planar motion of these systems, but move at speeds on the order of mm/s which is unsuitable for tasks such as exploration of a large area. Efficient and directional transmission of vibrational energy from the actuator to the ground can affect the speeds achievable by vibration-based locomotion. The project explores the limits of vibration-based locomotion in a self-folded robotic system to characterize and achieve controllable locomotion that is easily incorporated into laminate structures.

Vibration-based Adhesion for Robotic Wall-Climbing

The project described in this chapter further explores the application of vibration-actuation by investigating how vibration-actuation of flexible structures affords new robotic capabilities. Building on the application of vibration locomotion for self-folding robots, this project investigates a simple instantiation of wall-climbing in a robotic system. Controllable adhesion, the ability to selectively attach or detach from a surface, is an essential capability for many engineered systems, such as materials processing equipment, wall-climbing robots, and pick-and-place machinery. Robots capable of controllable adhesion have applications for inspection and repair, surveillance, and exploration of environments unsuitable for humans [10, 11]. A variety of controllable adhesion techniques have been proposed to enable these use cases, including methods relying on pneumatic, electromagnetic, and dry fibrillar adhesive forces between a robot and a surface. While existing techniques are often effective, they usually require relatively heavy and energy consuming components, and/or intrinsically link high normal and shear adhesion.

Previous approaches have used active pneumatic adhesion (i.e. suction) [12, 13] or strong electromagnets or permanent magnets [14] to demonstrate high adhesive stresses to enable wall-climbing for relatively heavy systems (e.g. $\sigma_{max} = 20.1$ kPa for an individual suction unit weighing 0.8 kg [15]). However, these approaches are, in general, limited to non-porous and ferromagnetic surfaces, respectively. In addition to surface restrictions, these systems usually require additional bulky hardware (i.e. traditional pumps and magnets). Despite these disadvantages, some pneumatic and electromagnetic approaches do have the advantage that they do not require direct contact with surfaces for adhesion. Thus, adhesion can be maintained while the manipulator or mobile robot smoothly slides across the adhering surface. This non- or light-contact mode of adhesion may be advantageous for mobile inspection robots that need to move easily across surfaces.

Nonetheless, the power and weight requirements for pneumatic and electromagnetic adhesion introduce design challenges at smaller scales (i.e. mm to cm scale). In the past two decades, a variety of adhesion methods inspired by biological adhesive systems such as gecko toes (dry fibrillar adhesives [16]) and insect feet (capillary and tunable soft interfacial adhesion, [17, 18, 19]) have been proposed to address these size and weight limitations. Dry fribrillar adhesives use patterned arrays of soft microstructures to induce Van der Waals interactions between the substrate and the microstructure [20, 21, 22, 23, 24]. This approach provides high strength-to-weight performance and requires no energy to maintain adhesion, but is limited to low force angles [25]. Additionally, the adhesive strength of these approaches degrades on dirty surfaces [26, 27]. Capillary adhesion occurs between surfaces through an intermediate wetting layer. Adjusting the wetting layer volume and viscosity can control adhesion force and ultimately enable or disable adhesion to the surface. However, capillary adhesion requires a supply of fluid and surfaces that have appropriate wetting properties (e.g. hydrophilic for a water wetting layer) [28]. Additionally, these systems are subject to degradation and fouling from chemical and particulate contaminants on the surface [29].

These tradeoffs between contact and non-contact adhesives highlight a demand for low-weight, non-contact and low-friction mobile adhesive mechanisms that can be used in fluids such as air and water. This project develops an adhesion mechanism that relies on the fluid-mediated adhesive force between an oscillatory plate and a surface. This lightweight, low-power mechanism provides high normal—but low shear—adhesion, making it uniquely suitable for robotics applications including mobile robots and some manipulation tasks.

Augmenting Inflatable Robotic Limbs with Variable Stiffness

The compliance of soft robots is an advantage for deployment in environments where close proximity to people is unavoidable [30], for systems to be resilient to a harsh environment [31], or when traversing over highly variable terrain [32]. Despite these advantages, soft mobile systems face challenges due to limitations related to their ability to exert or resist significant forces in their environment. The inherent flexibility of soft mobile robots can make it difficult for them to perform certain tasks, such as lifting or moving heavy objects [33].

To address this disadvantage, previous work has implemented various strategies to augment soft structures with the capability to switch between soft and stiff states [34]. These strategies range from thermally driven phase changes in structural elements [35] to pneumatically controlled jamming (granular[36], fiber[37], and layer [38, 39, 40, 41] jamming). Thus, one potential approach to increasing the stiffness for soft mobile systems intended for obstacle heavy environments is the incorporation of layer jamming into inflatable robots. Do *et al.*[42] incorporated jamming into everter-style robots to jam the underlying everter into a variety of configurations, but only demonstrated success in supporting relatively low loads. Shah *et al.* [43]

developed jamming skins that can be formed into 3D shapes for user-specific applications or formed around soft objects for on-demand rigidity. This work did not provide much guidance for what length scales the skins would provide the most benefit, particularly relevant due to changing failure modes with length scales. Another recent work used a plastic mesh embedded in a silicone membrane to create a variable stiffness replacements for rigid robot links. In this case, the focus of their analysis was on human-robot interaction rather than mobile robotic systems [44].

One attractive approach for the design of mobile soft robots is to make them out of inflatable flexible skins, resulting in relatively low-mass, scalable soft robots [45, 46]. However, inflatable structures are prone to buckling failure due to transverse and axial loads [42, 47, 48]. In some cases, this effect can be beneficial. For example, for "everting robots"[49], buckling behavior can be leveraged to navigate obstacle-heavy environments. Despite advantages in specific use cases, exceeding the critical buckling load of inflated structures generally results in large deflections which can be problematic when supporting heavy payloads or when inflatable systems are used for mobile robotics [50] or manipulator arms [51]. The tendency to buckle can be mitigated by increasing the radius of a structure, increasing the internal pressure, or decreasing the overall length, strategies which are unfortunately not feasible for all mobile systems. Inflation pressures are limited by the size and weight of the source of pressure (often a pump), and the intrinsic material strength of the pressure vessel. Depending on the application, such as moving through cluttered environments, a beam with a large radius (i.e., with a low aspect ratio) can be impractical. A preferable solution would be to use a flexible skin for inflatable limbs that increases in stiffness when pressurized to limit buckling.

Variable Stiffness Design for Minimally Invasive Surgical Retraction

Retraction, the act of holding back underlying organs and tissues so that body parts underneath can be operated upon, while straightforward for open surgery, is a significant challenge for minimally invasive surgery (MIS). The retractors used for open surgery are too big to pass through the small incisions used in laparoscopic procedures [52]. Retractors specific for MIS (such as a paddle[53] or a Nathanson liver retractor [54]) have been developed for laparoscopic procedures, but they possess several key limitations: they (1) require a dedicated incision; (2) are dependent on the location and size of the incision; (3) require an additional surgeon or external anchoring to maintain retraction; and, (4) must apply concentrated forces to retract larger internal organs, such as the liver or bowel. Many of these concerns are tied to the inherent rigidity of the available tools, which prevent the surgeon from flexibly accessing the operative site and minimizing additional trauma [55]. Thus, there is a need for soft or variable stiffness retractors that can adapt to the large variety of situations that surgeons may experience in the operating room.

While previous work has explored the promise of jamming based techniques for variable stiffness robotic MIS systems, these studies have not satisfied the requirement to pass through small laproscopic ports. Folding-based approaches can help address this challenge. Origami and folding-based devices have been widely proposed for minimally invasive procedures due to their ability to change from a compact package to a larger functional shape.Folding-based approaches [56] have been demonstrated to improve access during minimally invasive procedures, but there have been no previous works that solve both access and retraction for traditional laparoscopy.

Chapter 2

Towards Rapid Customization of cm-scale Self-folding Agents

Large robotic collectives provide advantages such as resilience to mechanical failure of single agents and increased capabilities for search and coverage based applications. However, a lack of rapid and free-form manufacturing processes remains a barrier to high-volume fabrication of mechanically heterogeneous robotic swarms. Self-folding laser-machined structures have the potential to enable heterogeneous robotic swarms. As an initial step to realizing a functional robotic collective, we focus on the design and characterization of the locomotion of an individual laminate manufactured robot. We look to a vibration-based locomotion technique that uses flexible structures or bristles to enhance the effects of vibration, allowing for fast locomotion (i.e. a “bristle-bot”). However, previous bristle-bot implementations have not allowed for controllable steering behaviors with high locomotion speeds. We describe the extension of existing two dimensional bristle-bot models to a three dimensional model that explores parameters that govern linear and angular velocity. We implement an autonomous laminate-manufactured bristle-bot inspired robot capable of linear velocities of up to 23 cm/s and turning rates of 2 rad/s. Moving towards automated manufacturing, we also demonstrate a self-folding bristle-bot structure that uses a linear compression laminate to achieve a uniform leg fold angle.

2.1 Introduction

Limitations of most available manufacturing strategies preclude the rapid fabrication of heterogeneous and sizable robotic collectives. For many robotic platforms, manufacturing is a time-consuming and single-threaded process. Rapid prototyping techniques, such as 3D printing, have revolutionized small-scale manufacturing, but the fabrication time of 3D printing generally scales with O(L^3) where L is the characteristic length scale of the printed part. Additionally, 3D printing with heterogeneous materials (i.e. to print complete robots) is still an open research question. Conventional large-scale manufacturing techniques, such as injection molding, allow for fabrication of many of one particular part rapidly, but requires the fabrication of expensive molds, limiting design adaptability and customizability. Self-folding via laminate manufacturing [1, 2, 57, 58] bridges the gap between customizable and high-throughput manufacturing and is well suited to the rapid fabrication of robotic swarms.

Laminate-manufactured robots, such as RoACH [3], HAMR [59], Omegabot [60], our previous self-folded inchworm [4], and quadruped [1] robots, and a magnet driven self-folding robot [61] have demonstrated different locomotion methods that are compatible with this manufacturing technique. For example, RoACH and HAMR exhibit crawling alternating tripod gaits, at speeds of approximately 1 body length per second, driven by conventional motors to achieve robust and stable locomotion. Omegabot utilizes shape memory alloys (SMA) wires to drive an inchworm inspired linkage, and the robot developed in [61] uses stick-slip locomotion driven by an external magnet. Flying robots have also been developed using laminate manufacturing [5, 6]. Incorporation of conventional actuators, such as motors, requires additional mechanical complexity, and often some degree of manual intervention during the assembly process. Vibration-based locomotion via eccentric rotating mass (ERM) motors is advantageous as the actuation method is self-contained within the motor housing. Integration of these motors into a laminate design simply requires attachment of the housing to the robot structure, and does not require additional connection to a transmission such as engaging a motor spindle to a linkage [1].

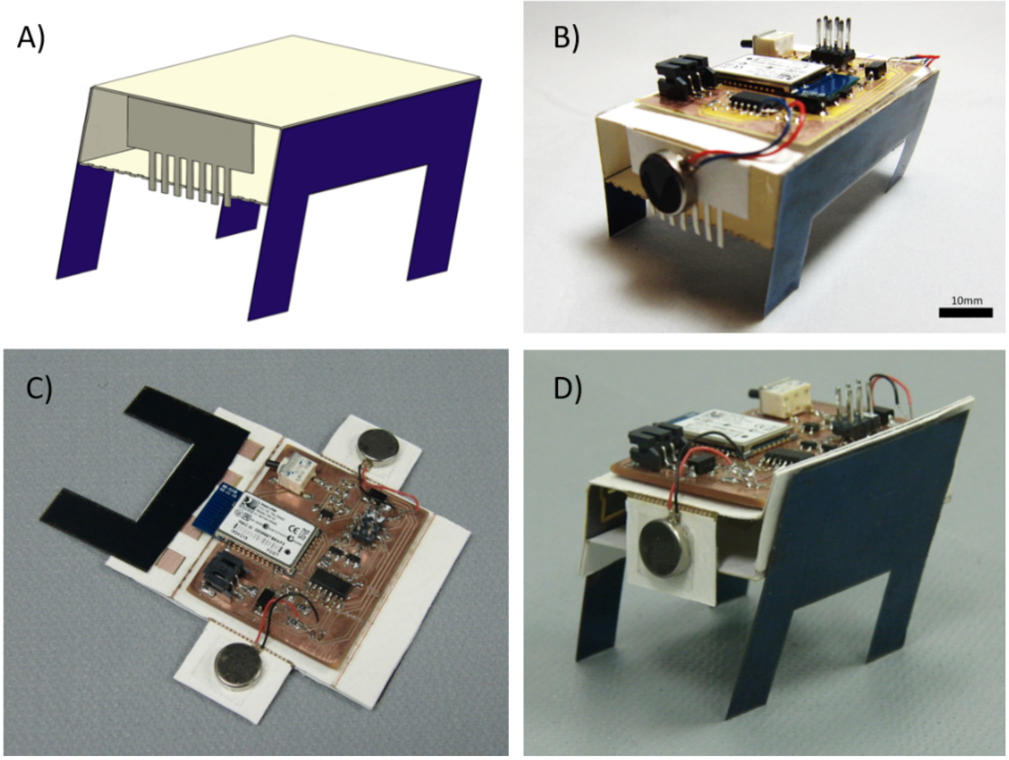

Figure 2.1. Self-deploying laminate manufactured swarm robots A) Computer aided design (CAD) of manually folded robot for characterizing locomotion of bristle-bots. Interchangeable legs allow testing of various leg lengths and side latching allows testing of various leg angles. B) Photo of manually folded, variable angle robot for linear and angular velocity testing. The leg material is laser-machined from spring steel shim stock. The robot body is laser-machined from paperboard. A modular circuit board is affixed to the top. Eccentric rotating mass (ERM) motors are attached to side panels and provide vibrations to drive locomotion. C) Self-folding robot using linear compression SMP to achieve final configuration as manufactured (before folding) D) Self-folding robot, after folding.

Vibration-based locomotion provides a simple and inexpensive planar locomotion modality; actuators are self-contained and easily incorporated into laminate structures via adhesives. Robotic systems that leverage vibration-based locomotion such as Kilobot [7, 8], ViMbot [62], and robots demonstrated in [9] have successfully demonstrated controllability, but move at speeds of on the order of mm/s which is unsuitable for tasks such as exploration of a large area. Vibration-based locomotion that utilizes angled legs to increase linear velocities, (e.g. as seen in bristle-bots) operates on the principle of stick-slip locomotion, where either the robot or the surface on which the robot is placed vibrates to cause deformation in flexible bristles. Due to an intentional angle in the bristles (or legs), this vibration causes the legs to stick and bend as they are compressed, and slip as they relax, resulting in ratchet-like forward locomotion (Fig. 2.2). Previous work on modeling bristle-bots has characterized their motion in two dimensions (horizontal and vertical linear motion) [63, 64] and previous designs have achieved speeds of up to 17 cm/s [63] and 32 cm/s [64], much faster than the controllable vibration-based robots mentioned above.

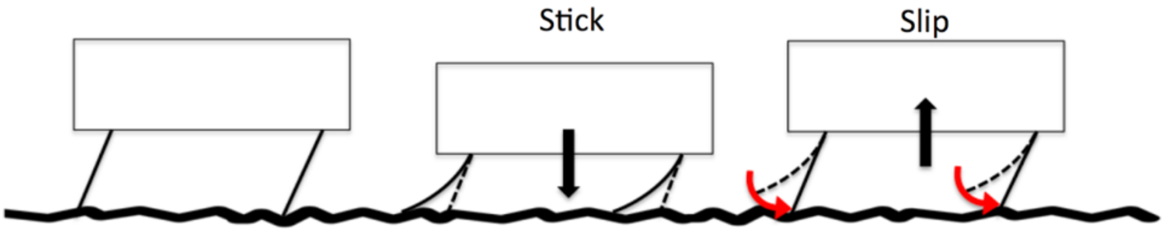

Figure 2.2. Stick-slip locomotion with flexible bristles: A key characteristic in bristle-bot vibration-based locomotion.

A limitation of previous work on bristle-bots is they only describe horizontal and vertical locomotion and ignore turning or rotation in yaw. In this paper, we extend a previous two dimensional model [63] to three dimensions to characterize and achieve controllable locomotion that is easily incorporated into laminate structures. We characterize the following factors that affect the locomotion of bristle-bots: motor frequency, body mass, leg length, and body width.

To begin, we outline the assumptions and equations of the 2D locomotion model that we then use to generate the 3D locomotion model. We then discuss our fabrication process. In particular, we highlight the mechanical and electrical design of a manually-adjustable robotic laminate structure for the velocity testing mentioned above. Additionally, we present work towards a self-folding version of our manually reconfigurable robot structure (Fig. 2.1). We then present the results of our experimental testing, and compare those results to numerical simulation. We end with overall conclusions and suggestion for future work.

2.2 Vibration Actuated Locomotion Designs

In this section, we derive a quantitative model of vibration based locomotion to enable rapid customization of robot design. This provides guidance for initial robot design and for modification of a robot's structure based on its working environment.

2.2.1 2D Modeling

In previous work on modeling bristle-bot locomotion [63], the authors present a model that describes motion in the horizontal and vertical directions. We adapt their model, which provides actuation through either a vertical or horizontal linearly oscillating mass, to use a single mass rotating around the body-fixed y-axis (Fig. 2.3).

In this study, we make many similar assumptions to this previous work, namely:

- The body remains parallel to the ground at all times
- The legs are modelled as mass-less rigid rods connected to the robot body by torsional spring and damping elements
- The legs are modeled as a single equivalent leg under the center of mass of the robot
- Friction is modelled as Coulomb dry friction

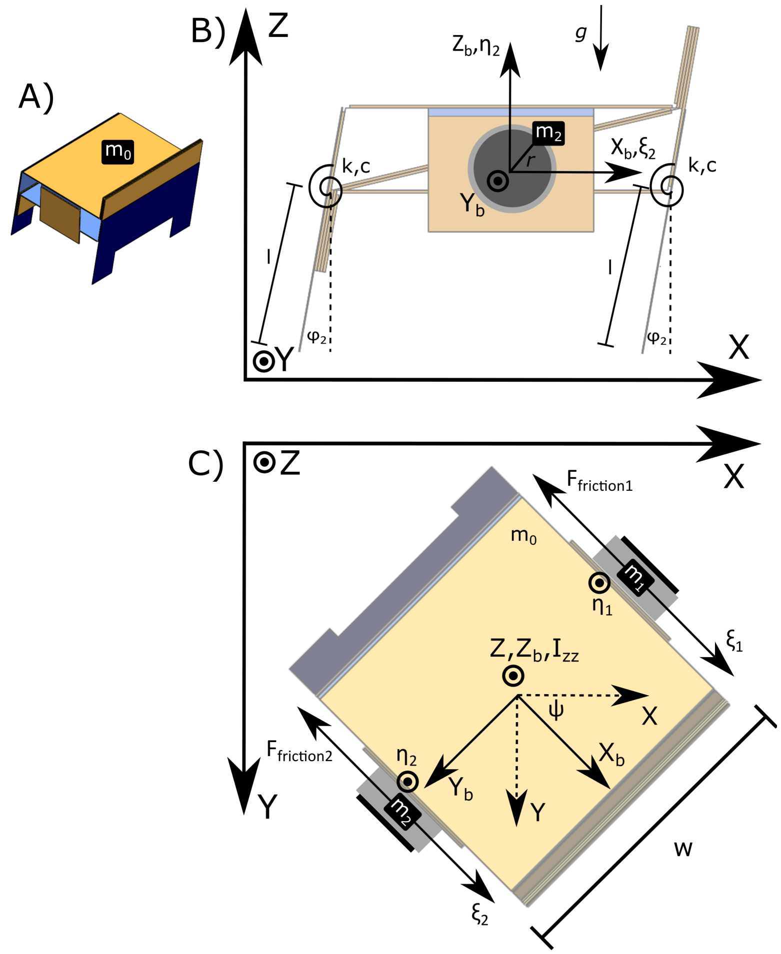

Figure 2.3. Diagram of forces A) Isometric View B) Side View C) Top View

Based on these assumptions, the equations of motion that describe the 2D motion of the robot in the XZ plane are found to be:

$$\begin{aligned} &\ddot{x}_i + \frac{m_i}{m_R}\ddot{\xi}_i = \\ &-\mu\left[g - l\ddot{\varphi}_i\sin\varphi_i - l\dot{\varphi}_i^2 cos\varphi_i + \frac{m_i}{m_R}\ddot{\eta}_i\right] \\ &\cdot\left[\text{sign}(\dot{x}_i - l\dot{\varphi}_i\cos\varphi_i)\right], \end{aligned} \tag{2.1}$$

$$\begin{aligned} &\left[\ddot{\varphi}_i\sin\varphi_i + \dot{\varphi}_i^2\cos\varphi_i - \frac{g}{l} - \frac{m_i}{m_R\cdot l}\ddot{\eta}_i\right]\cdot\sin\varphi_i \\ &+\frac{nc}{m_R\cdot l}\dot{\varphi}_i\cos\varphi_i + \frac{nk}{m_R}\cos\varphi_i(\sin\varphi_i - \sin\varphi_0) = 0. \end{aligned} \tag{2.2}$$

In the above equation, x_i is the displacement in the horizontal direction of the center of mass, φ_i is the angle of the legs with respect to the vertical direction, (Equivalent to vertical displacement), ξ and η are the prescribed horizontal and vertical displacements respectively for the eccentric rotating mass, m_i is the mass of the rotating mass inside the ERM motor, m_R is the total mass of the robot calculated as the ERM plus body mass, m_0, $m_R = \sum_{i=1} m_i + m_0$, l is the leg length, nc is the torsional damping coefficient summed over all legs, nk is the torsional spring constant summed over all legs, φ_0 is the nominal leg angle, μ the coefficient of static friction, g is the acceleration due to gravity.

2.2.2 3D Modeling

We modify the 2D case by incorporating two 2D models that are fixed at a distance w from each other. The rotational motion is described in Equation 2.4.

In this 3D model, we borrow many of the assumptions of the 2D case, with the additional assumptions as follows:

- Rotation of the body occurs purely in yaw, rotation in pitch and roll are negligible

Table 2.1. Default Bristle-bot Parameters

Structure		
Main mass	m_0	17.33 g
Bristle length	l	15 mm
Bristle angle	φ_0	10°
Stiffness	nk	56 N/m
Damping	nc	0.1 $N*s/m$
Excitation		
Prescribed ERM Motion	ξ_i	$A\sin(2\pi f_i t-\phi_i)$
	η_i	$-A\cos(2\pi f_i t-\phi_i)$
ERM Frequency	f_i	95-120 Hz
ERM Phase offset	ϕ_i	0
ERM Amplitude	A	2 mm
ERM Mass	m_i	1.67 g

- Both actuation frequencies, f_1 and f_2, occur in phase (i.e. $\phi_1 = 0$ and $\phi_2 = 0$)

In the 2D case, i was equal to 1; giving one equation describing the motion in x and one equation describing the motion in z for two governing differential equations. However, in 3D we have two sets of equations describing motion in x and z for each side of the bristle-bot. To differentiate the x and z displacement we use the subscript i = 1 for the left side and i = 2 for the right side. This results in four equations in x and z for each 3D bristle-bot model in addition to an equation describing rotation in yaw (Equation 2.4). For clarity, the friction forces that appear in the yaw equation are expressed separately in Equation 2.3.

$$\begin{aligned} F_{Friction_i} = \\ -m_R\cdot\mu\left[g-l\ddot{\varphi}_i\sin\varphi_i-l\dot{\varphi}_i^2 cos\varphi_i+\frac{m_i}{m_R}\ddot{\eta}_i\right] \\ \cdot\left[\operatorname{sign}(\dot{x}_i-l\dot{\varphi}_i\cos\varphi_i)\right], \end{aligned} \tag{2.3}$$

Moment balance around center of mass:

$$\ddot{\psi} = \frac{1}{I_{zz}} \cdot \frac{w}{2} \cdot \left[m_1 \ddot{\xi}_1 - m_2 \ddot{\xi}_2 + \sum_{i=1}^{2} F_{Friction_i} \right]. \tag{2.4}$$

where:

- ψ Yaw angle displacement, rotation around the z-axis
- I_{zz} is the mass moment of inertia around the z-axis
- w is the robot body width

2.3 Laminate Robot Fabrication

To verify our models, we prototyped a manually-adjustable laminate robot design to test the various physical parameters outlined in the above model. Subsequently, we fabricated a self-folding robot as a step towards automated swarm assembly.

2.3.1 Self-Folding Composite Laminates

Composite laminates are assemblies of layers of different materials which, when joined, provide desirable engineering characteristics or additional functionality. Various methods to actuate self-folding composite laminates for self-assembly in [2, 65], and [66, 67] have demonstrated the extended capabilities of laminate manufacturing on the millimeter scale. Throughout the prototyping process, we constructed our composite laminates from four material classes.

- Structural materials: paperboard and spring steel shim stock
- Flexural material: copper-clad kapton (Pyralux AR181200R, Dupont), and polyethylene terephthalate (PET) film

- Shape memory polymer (SMP) material: pre-strained polystyrene (PSPS) (KSF50-C, Grafix)
- Adhesive material: high-temperature silicone adhesive (IS-7876, ARclad)

Structural materials add rigidity and define the permissible strains of self-folding structures. By designing the structural layer with pre-defined crease patterns, we can achieve specified folding behavior. Previous work has presented a general, algorithmic approach to the design of all the layers of a self-folding laminate, including the parameters for the crease patterns to achieve a desired self-folding 3D geometry[68, 69].

Our composite layers consisted of two spring steel legs connected to an adjustable four-bar linkage composed of two paperboard layers, (Fig. 2.4). Flexural material was used to connect the hinges of the linkage. The material serves two functions: it serves as a circuit layer for the electronics, and also as passive flexural hinges. We used PET as the flexural material in our modular testing robot. Lastly, a shape memory polymer was required for the self-folding behavior [2], for which we used a 250 μm thick sheet of PSPS.

2.3.2 Manually-Adjustable Robot Design

To perform the locomotion characterization, we used a test setup with a manually reconfigurable robot body. Using a parallelogram four-bar linkage for the body, we could uniformly alter the angles of the legs for different tests by shifting the side locking mechanisms (Fig. 2.4). The legs were interchangeable for testing various leg lengths. We used a CNC laser cutter (Universal Laser Systems PLS6MW) to cut 350 μm thick paperboard for the body and 0.127mm (0.005 inch) thick shim stock for the legs.

2.3.3 Electronic Circuit Design and Fabrication

We fabricated custom in-house circuits to provide motor control and power regulation. For the characterization tests, we fabricated a rigid PCB for convenience when interchanging the

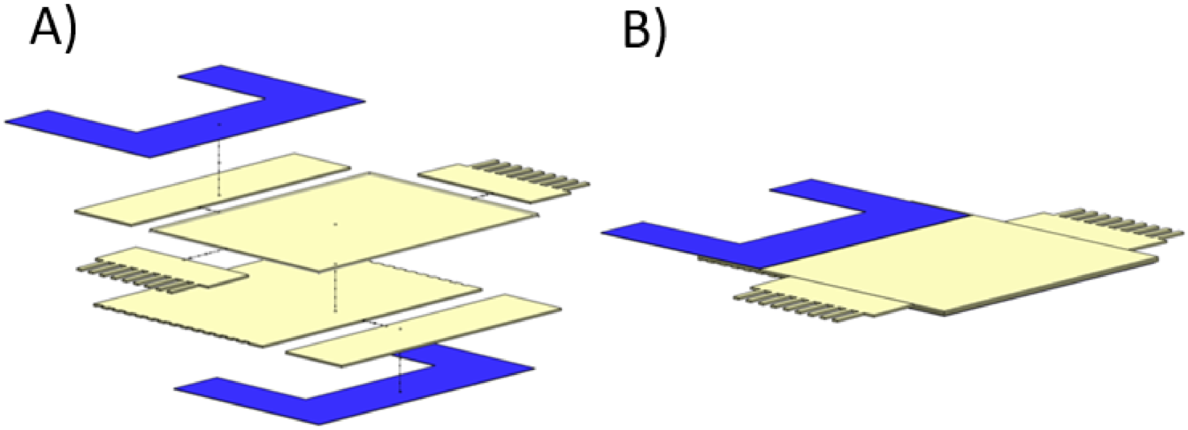

Figure 2.4. Layer arrangement of modular robot body. A) Exploded view of structural layers. Light-colored layers are fabricated from paperboard and dark-colored layers are fabricated from spring steel shim stock. B) The assembled laminate composite, before folding.

robot body. However, for the self-folding robot, we embedded a flexible circuit layer within the laminate composite to achieve electrically-activated self-folding, similar to the heating method of the previous self-folding crawler [1].

We designed the circuit and board layout in EagleCAD and printed a mask using a solid-ink printer (Xerox Colorqube 8580) on Pyralux. We followed a copper etching protocol with ferric chloride to dissolve the exposed copper regions and then removed the solid-ink mask and soldered on surface-mount components. Our circuit design used a simple DC-motor driving circuit controlled by an Atmel ATtiny24 and powered by a 3.7V lithium-polymer battery regulated down to 3.3V (Fig. 2.5).

2.3.4 Self-Folding Robot Design

We developed a self-folding actuation method based on the previously mentioned manually-adjustable four-bar linkage (Fig. 2.7). In this design, folding of the four-bar linkage is achieved by a single linear compression laminate structure that is incorporated into the main robot linkage (Fig. 2.6E). We choose a four-bar parallelogram linkage to mechanically enforce all legs to fold to the same angle; eliminating the potential error that could be introduced by

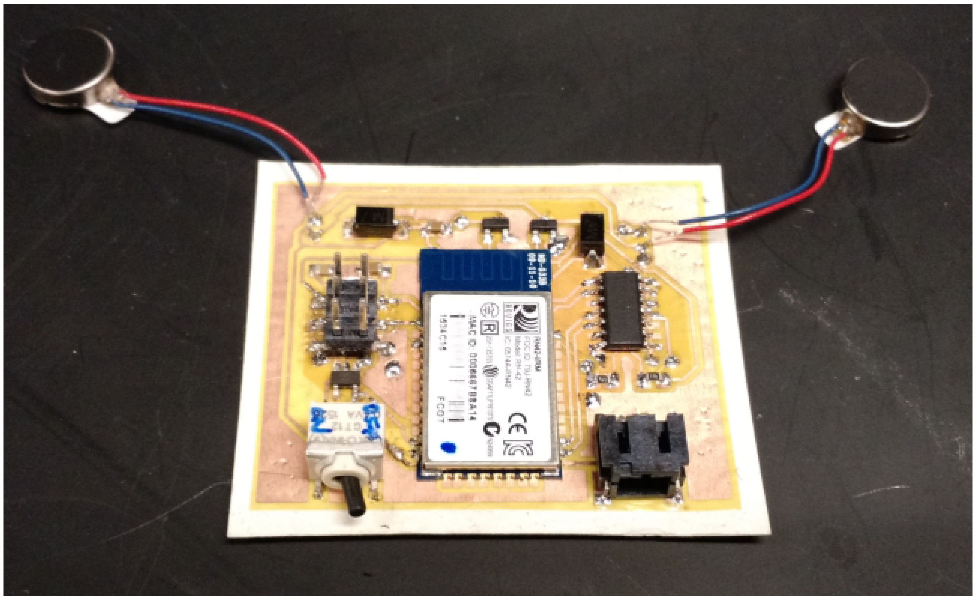

Figure 2.5. Custom in-house fabricated control board used for testing the modular robot to characterize bristle-bot parameters. A simple motor driving circuit was controlled by a programmable ATtiny24.

multiple inter-dependent folding steps.

A heating circuit is incorporated into the top flexible layer. Joule heating of the linear compression element (Fig. 2.7A and Fig. 2.7B) folds the four-bar linkage and two flaps that rotate ERM motors into position.

There are many examples of self-folding achieved by applying torques at the locations of folding (i.e. the hinges) [1, 58, 61, 60, 65, 67]. However, this limits the amount of torque that can be applied to achieve folding as the moment arm remains relatively small. We developed a laminate structure to achieve larger deformations at higher torques than are achievable by locally heat-activated PSPS. The principle is similar to actuation by pouch motors demonstrated in [70].

Based on the flat structure and the desired final fold angle, we calculated the gap required to fully fold:

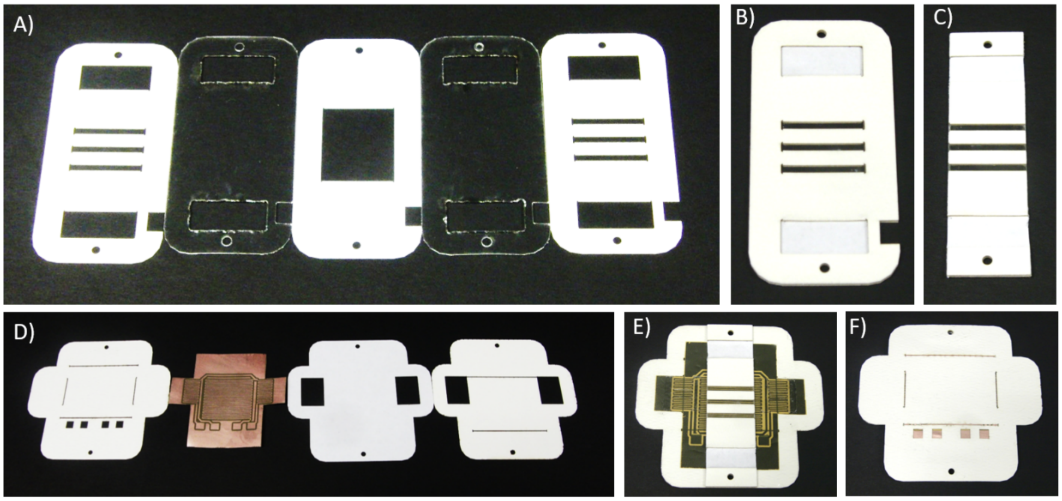

Figure 2.6. Lamination of the self-folding robot design A) Linear compression element layers from left to right: paperboard, PSPS, copypaper, PSPS, paperboard. Adhesive layers (silicone adhesive) are omitted B) Laminated layers of linear compression element C) Partially released linear compression element prior to incorporation into the four-bar laminate. D) four-bar structure layers from left to right: paperboard, copper-clad kapton heating layer, copypaper, paperboard. Adhesive layers are omitted. E) Partially laminated design demonstrating incorporation of linear compression element. F) Laminated structure prior to release from surrounding support and subsequent addition of legs and electronics.

$$Gap = CD + BC - \sqrt{CD^2 + BC^2 - 2 \cdot CD \cdot BC \cdot \cos\theta} \tag{2.5}$$

Due to the bi-directional contraction of activated PSPS, large areas of unconstrained shrinking often result in out-of-plane twisting, which can affect the folding behavior. To mitigate this issue, we designed multiple small gaps of unconstrained PSPS that sum up to the calculated gap size.

We prototyped the robot design in CAD software and imported the planar construction lines into a recently developed laminate design software tool (popupCAD [69]). In this software, individual layers were designed and support material was automatically generated (Fig. 2.6(A,D)).

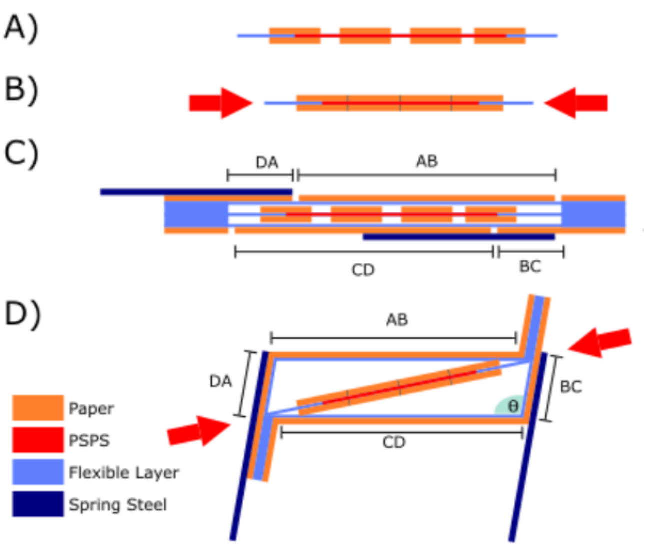

Figure 2.7. A laminate composite robotic design based on a self-folding four-bar linkage. This linkage provides a reliable and consistent fold angle for all legs. If legs were not mechanically linked, closed-loop control would be necessary to ensure uniform folding across the structure [9]. Heating circuits are incorporated in flexural layer. A) Side view of linear compression elements. B) Gaps between paper layer close upon heating. C) Full laminate design D) Upon heating structure folds via diagonal compression element.

The power for folding is provided from an external power supply. Holes were designed in the top structural layer to provide access to serpentine heating traces. A custom circuit board was designed to provide temporary electrical contact while folding, and subsequent release due to heating hot-melt adhesive similar to the process described in [9]. Self-folding via heating of PSPS is energy intensive, typically drawing several watts over the time span of one to two minutes. We chose to provide the energy to fold from an external supply; this allowed the self-folding robot to operate with a smaller battery voltage and energy capacity and thus overall robot mass.

2.4 Experimental Results

We experimentally validated these simulation results with four sets of tests. Three tests investigated the effect of robot mass, motor actuation frequency, and leg length on linear velocity. The last test looked at the effect of body width on angular velocity. Model validation was performed via motion capture from video (Fig. 2.8) of robots fabricated with different geometric parameters or driven at several motor frequencies. Position data was extracted from the video taken from above. Average velocity measurements were taken to be the average displacement over two seconds. Three trials are performed for each result presented below.

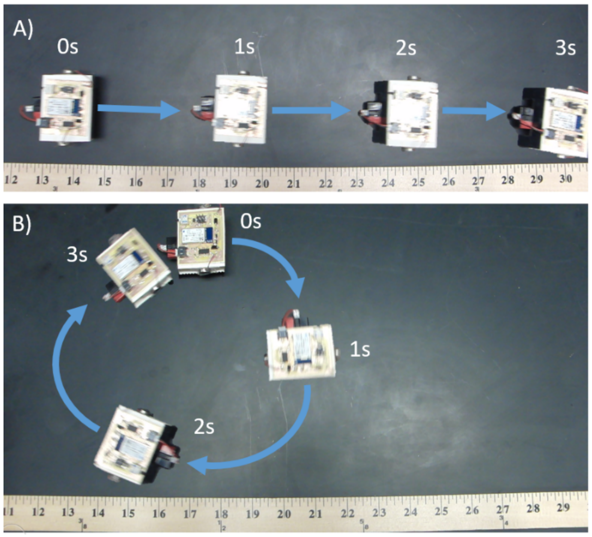

Figure 2.8. Images extracted and overlaid from overhead video taken of robot locomotion. Position data over a two second period was averaged to get velocity measurements for each trial. Three trials were performed for each data point. A) Linear velocity test, both motors on B) Angular velocity test, only left motor on.

2.4.1 Linear Velocity

For this set of tests we varied three parameter sets: robot mass, robot actuation frequency, and robot leg length.

Based on the 2D model, we present several numerical simulations, performed using Matlab's ode15s function, and compare these to experimental results to show how the mass of the body of the robot, actuation frequency, and leg length all affect the linear velocity of the robot, $\dot{x}_1$. The default parameters used are listed in the Table 2.1.

The spring steel legs were designed to have good adhesion to the robot structure as well as contact the ground in a single plane. Thus they were designed as two sets of mechanically linked legs in the shape of an inverted U (Fig. 2.9d). Rather than analytically calculating the spring constant, *nc*, of the legs based on the u-shape, the spring constant for the numerical simulation was used as a parameter to fit the results of the simulation to the experimental data. This fit assumed a linear relationship between leg length and the leg spring constant.

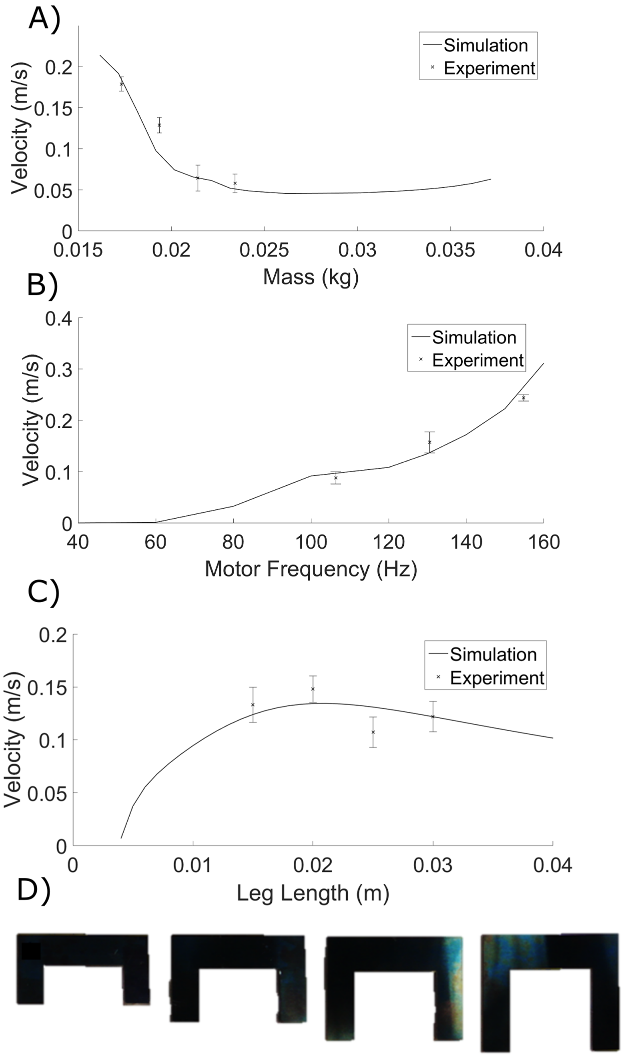

Figure 2.9. Comparison of experimental and simulation results for linear velocity as a function of geometric and actuation parameters A) Linear velocity vs. robot mass. B) Linear velocity vs. actuation frequency. C) Linear velocity vs. robot leg length. D) Robot legs of varying length laser-machined from spring steel shim stock.

As the mass increased, the normal force increased and the inertia of the robot body dominated the dynamics to the point where the forward locomotion decreases to a near constant value (Fig. 2.9a). The upper range of mass values tested is limited by the static stability of the robot. Since the legs are angled, additional weight will shift the center of mass from beneath the area enclosed by the bristles, eventually causing the robot to tip over.

As actuation frequency increased, the ERM motor rotated faster and increased the rate at which stick-slip occurs, (Fig. 2.9b). The maximum frequency in these tests was limited by the maximum allowable driving voltage for the ERM motor. At low frequencies, the rotational force imparted by the motor were unable to overcome the robot body mass and the surface friction. Once the force due to the rotation exceeded the static body and friction forces, locomotion began and velocity increased with frequency. In the simulation results, we saw a slight jump in expected average velocity at approximately 100 Hz. This is most likely due to the non-linearity in the model dynamics.

As the leg length was increased, the linear velocity increased, peaked, and then decreased (Fig. 2.9c). An increased leg length can be though of as increasing the possible step-length of the robot. However, after the leg length is increased past a certain point the average velocity decreased. This was due to the length of the legs also impacting the spring and damping constants of the modeled torsional springs and dampers. As length is increased, the spring constant decreases and shifts the resonant frequency. At shorter leg lengths, the spring constant increased and viscous damping dominated locomotion; at longer leg lengths, the robot body and leg motion became highly oscillatory and under-damped.

2.4.2 Angular Velocity

For this test, we sought to understand how the width of the body of the robot affected the angular velocity. From the experimental results, we observed a maximum angular velocity of approximately 2 rad/s at a robot body width of 5.08 centimeters (2 inches; Fig. 2.10). The existence of a maximum turning rate was likely due to the balance of the moment of inertia of the robot body and moments applied by the rotating mass. As the width initially increased, the torque applied by the ERM motors increased at a faster rate than the moment of inertia; however, as the width continued to increase the inertia increased with the square of the width.

This ultimately decreased the average turning rate of the overall system.

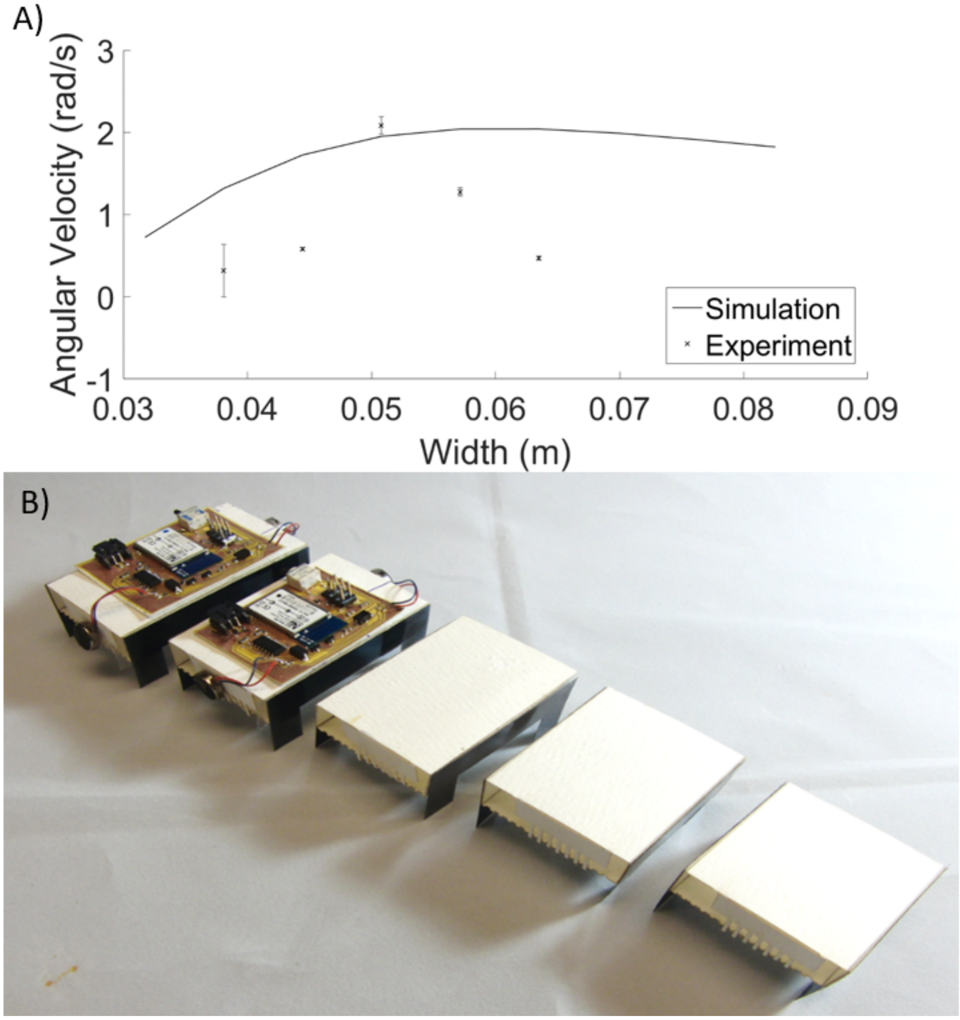

Figure 2.10. Graphical results and robot structures that were changed during this experiment. A) Comparison of experimental and simulation results for angular velocity vs width. B) Fabricated robots with various widths.

This model over-predicted the angular velocity of the robot by approximately a factor of six at certain values for the width of the robot body. This is most likely a result of many of the model assumptions, such as body rotation being limited to the z-axis. Additionally, lateral friction forces are not considered, possibly contributing to the over estimation of turning rate.

2.5 Conclusions

This work presents a locomotion characterization of a self-folding laminate bristle-bot design. The presented model provides qualitative information about velocity trends that can be used to guide the design of a heterogeneous robotic swarm. We additionally presented a self-folding technique that uses an SMP actuated linear compression laminate structure to achieve consistent leg folding for an individual swarm robot.

Future work will investigate how the robot structure can be tailored to a given payload or environment. For example, by increasing or decreasing the mass of the system, the resonant frequency will shift resulting in a change of peak locomotion speed. Parameters such as leg length and material can be used to keep the resonant frequency within the operating range of the motors. To better understand how these parameters affect resonant frequency, we plan to look at the frequency response of the average linear locomotion.

Better predictions of locomotion behavior could be achieved by using alternative damping and friction models. For instance, in this model we assumed viscous damping and Coulomb dry friction. Given different leg materials and surface frictions these assumptions might not hold up.

Additional work includes further developing the capability to deploy several self-folding laminate robots simultaneously and have them complete a coverage or search task with on-board sensing. We plan to investigate different wireless communication modalities, localization algorithms, and swarm control techniques as steps towards this goal.

Chapter 2, in full, is a reprint of the material as it appears in IEEE/RSJ Internation Conference on Intelligent Robots and Systems (IROS) 2017. Weston-Dawkes, W.P.; Ong, A.C.; Majit, M.R.A.; Joseph, F.; and Tolley, M.T., The dissertation author was the primary investigator and author of this paper.

Chapter 3

Gas-Lubricated Vibration-Based Adhesion in Robotics

3.1 Introduction

Controllable adhesion, the ability to selectively attach or detach from a surface, is an essential capability for many engineered systems, such as materials processing equipment, wall-climbing robots, and pick-and-place machinery. Robots capable of controllable adhesion have applications for inspection and repair, surveillance, and exploration of environments unsuitable for humans [10, 11]. A variety of controllable adhesion techniques have been proposed to enable these use cases, including methods relying on pneumatic, electromagnetic, and dry fibrillar adhesive forces between a robot and a surface. While existing techniques are often effective, they usually require relatively heavy and energy consuming components, and/or intrinsically link high normal and shear adhesion.

In this work we develop an adhesion mechanism that relies on the fluid-mediated adhesive force between an oscillatory plate and a surface. This lightweight, low-power mechanism provides high normal—but low shear—adhesion, making it uniquely suitable for robotics applications including mobile robots and some manipulation tasks.

Previous approaches have used active pneumatic adhesion (i.e. suction) [12, 13] or strong electromagnets or permanent magnets [14] to demonstrate high adhesive stresses to enable wall-climbing for relatively heavy systems (e.g. $\sigma_{max} = 20.1$ kPa for an individual suction unit weighing 0.8 kg [15]). However, these approaches are, in general, limited to non-porous and ferromagnetic surfaces, respectively. In addition to surface restrictions, these systems usually require additional bulky hardware (i.e. traditional pumps and magnets). Despite these disadvantages, some pneumatic and electromagnetic approaches do have the advantage that they do not require direct contact with surfaces for adhesion. Thus, adhesion can be maintained while the manipulator or mobile robot smoothly slides across the adhering surface. This non- or light-contact mode of adhesion may be advantageous for mobile inspection robots that need to move easily across surfaces.

Active pneumatic adhesion is advantageous in that pumps are commercially available and are relatively straightforward to control and integrate into a physical system. However, at small scales these advantages are lost as the manufacturing of MEMS micropumps [71] requires specialized high-precision equipment. Some studies have investigated small-scale pneumatic fluidic adhesion [72], but controllable adhesion has not been demonstrated.

While electromagnetic adhesion requires compatible ferromagnetic surfaces, electrostatic adhesion, or electroadhesion, is applicable to non-ferrous surfaces. Electroadhesion generates an adhesive force via applying a high voltage (hundreds to thousands of volts) to a patterned conductor [73, 74, 75, 76]. The high voltage generates a localized electric field that—when placed in close proximity to a substrate—causes an adhesive force. Electroadhesion provides large forces on a variety of surfaces and consumes very low power. However, the performance of electroadhesives decreases on rough substrates and is susceptible to the accumulation of dirt or dust on the adhesion interface [77] although recent work has demonstrated an electrostatic cleaning method that shows improved performance on contaminated surfaces [78]. Furthermore, the high-voltages required for electroadhesion lead to challenges with portability, safety, and miniaturization.

The power and weight requirements for pneumatic and electromagnetic adhesion have made it challenging to design systems at smaller scales (i.e. mm to cm scale) that use these strategies. In the past two decades, a variety of adhesion methods inspired by biological adhesive

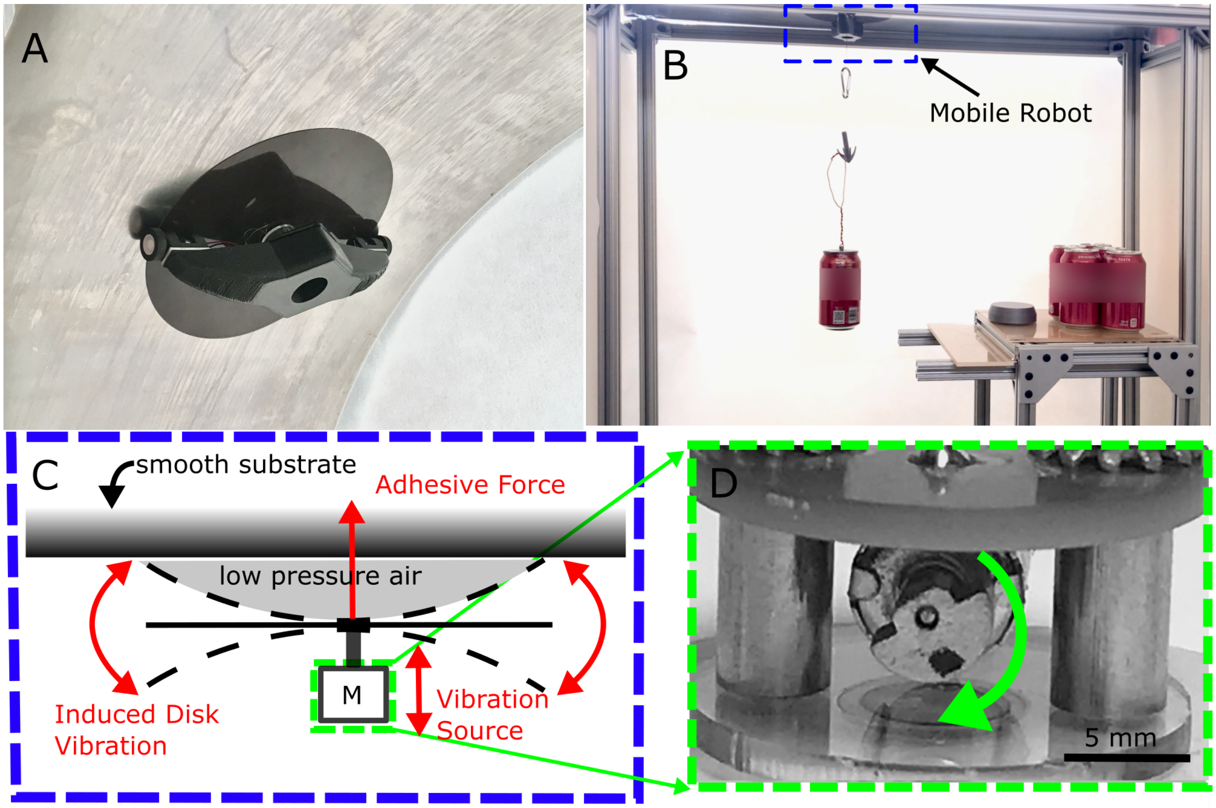

Figure 3.1. A flexible disk is capable of spontaneously generating an adhesive force if excited by a vibration motor when in close proximity to a surface. We used this mechanism to design a mobile robot capable of controllable and low-friction adhesion to surfaces at any orientation. (A) A two-wheel direct-drive robot uses a 6.9 cm radius vibrating disk and two drive wheels to traverse a curved, overhanging surface. (B) The mobile robot is capable of supporting over 3.8 N when excited with a small eccentric rotating mass (ERM) vibration motor. (C) In air, a vibrating flexible disk, placed in close proximity to a substrate, will generate a negative pressure in the thin gas film. The negative pressure region generates a substantial adhesive force that provides high normal adhesion with low resistance to lateral movement (figure not to scale, the gas film is less than 1 mm thick, see Figure 3.6 for detailed measurements). (D) Close-up of an ERM motor showing the eccentric mass than generates a sinusoidally varying vertical force when rotated.

systems such as gecko toes (dry fibrillar adhesives [16]) and insect feet (capillary and tunable soft interfacial adhesion, [17, 18, 19]) have been proposed to address these size and weight limitations. Dry fribrillar adhesives use patterned arrays of soft microstructures to induce Van der Waals interactions between the substrate and the microstructure [20, 21, 22, 23, 24]. This approach provides high strength-to-weight performance and requires no energy to maintain adhesion, but is limited to low force angles [25]. Additionally, the adhesive strength of these approaches degrades on dirty surfaces [26, 27]. Capillary adhesion occurs between surfaces through an intermediate wetting layer. Adjusting the wetting layer volume and viscosity can control adhesion force and ultimately enable or disable adhesion to the surface. However, capillary adhesion requires a supply of fluid, surfaces that have appropriate wetting properties (e.g. hydrophilic for a water wetting layer) [28], and are subject to degradation and fouling from chemical and particulate contaminants on the surface [29].

Hybrid systems that employ both dry fibrillar adhesives and electroadhesives have been shown to improve overall adhesion, especially on rough surfaces [79]. However, many of the previously mentioned limitations remain. Biomimmetic suction for marine environments has expanded the capabilities of controllable adhesive suction disks by allowing them to adhere to a wider variety of substrate types and roughnesses [80]. Similarly, capillary forces in combination with fibrillar structures can enhance adhesion on dry, hydrophilic surfaces [81]. Critically, fibrillar based adhesives require contact with the surface and often achieve adhesion in combination with high friction. Thus, these adhesives do not enable smooth and easy sliding of manipulators or robots across the adhering surface.

These tradeoffs between contact and non-contact adhesives highlight a demand for low-weight, non-contact and low-friction mobile adhesive mechanisms that can be used in fluids such as air and water. One such potential for fluid-mediated non-contact adhesion is through the suction force between two smooth, rigid plates, immersed in a fluid. When two surfaces immersed in an incompressible fluid are separated there is an adhesive force, often called Stefan adhesion, generated between the two surfaces. This force results from the motion of fluid as it fills the gap. However, because Stefan adhesion is generally modeled to scale with the relative normal motion between the surfaces, it cannot provide a steady-state adhesive force. In this work we demonstrate that a persistent adhesive force can, however, be generated between a flexible disk and a stationary surface by oscillating the disk in air. To the best of our knowledge this effect has not been employed previously to achieve controllable adhesion.

We explore a novel gas-lubricated controllable adhesion technique that uses vibration to generate high adhesive forces with commercially available hardware (Figure 3.1A). We perform static and quasistatic loading tests to investigate the maximum supportable load of a flexible disk excited by an eccentric rotating mass (ERM) motor (Figure 3.1B-C). We test a range of disk radii and motor driving frequencies to assess the effect on the maximum adhesive strength. We measure the radial pressure gradient in the fluid film for a representative adhesive strength test and compare it with the micron-scale displacement over time of the vibrating disk for several cases of static loads. Finally, we present a two-wheeled direct-drive robotic instantiation to highlight the design principles and capabilities of this adhesion method. By developing a low-weight active suction strategy that is simple to manufacture, we aim to expand the toolbox of controllable adhesion and illuminate opportunities to build new hybrid adhesion systems.

3.2 Design Principles

Analytical models for lubrication theory problems show a heavy dependence on the thickness of the lubricating fluid film. For the well-known case of Stefan adhesion[82], the resulting force varies with $1/h^3$. In general most analytical models prescribe the thickness of the fluid film and this is done in practice by controlling the flowrate or the pressure of the air in the case of an aerostatic bearing or by controlling the gap via some external mechanism [83]. When we brought a vibrating plate in close proximity to a smooth surface, the system spontaneously adhered and a steady-state fluid film emerged. Thus if the geometric and control parameters were chosen correctly, the physical system would inherently maintain a low-pressure region of ambient air and a gas film with an average thickness on the scale of hundreds of microns (Figure 3.6).

The mobile robot consists of two primary subsystems: 1) a flexible disc with a vibration source that excites vibrations normal to the surface in order to generate adhesion, and 2) a drive system that provides stable contact between traction wheels and a surface to enable locomotion. In the following subsections, we describe in detail the design and evaluation of each of these subsystems.

3.2.1 Adhesive subsystem

Vibration Source

To generate vibration of the adhesive disc we used vibration motors (commonly used to generate haptic feedback). In the majority of our experiments, we used eccentric rotating mass (ERM) motors as they provided the ability to control the amplitude of the maximum acceleration by pulse-width modulation (PWM) of the input voltage. The vibration in these motors is generated by rotating a mass; as a result, they provide an oscillatory force that is not confined to a specific axis of motion. Instead, when the rotational axis is parallel to the surface of the vibrating plate, the ERM provides oscillatory forces that vary sinusoidally with time in the orthogonal and transverse directions. Precise frequency control requires some kind of feedback, either by use of an encoder, measurement of back electromotive force (EMF), or by counting commutation spikes. In adhesion experiments we used a more precise linear resonant actuator (LRA) to generate plate vibration. LRAs provide excitation along a single axis and require an AC signal to drive, meaning that the frequency can be controlled open loop. However, the low vibrating mass of these systems also means that generating large vibration amplitudes requires the system to be operating at a resonance frequency. For this reason, we limited the use of LRAs to characterization experiments that required vibration in only a single direction.

Flexible Disk

The vibration source is mounted to a flexible disk to generate vibrational motion near the adhesive surface. There are three main design parameters for a uniform flexible disk: 1) disk material, 2) disk thickness, and 3) disk radius. The first two parameters have a significant effect on the bending stiffness of the disk and thus will influence the vertical deflection of the disk under vibration. Thicker disks require higher oscillatory forces from the motor to generate plate bending and deflection. Altering the disk radius will change the disk area and, consequently, the resistance to lateral movement and normal motion will change. Changing the radius will also change the stiffness of the disk.

To gain insight into how the geometric properties of the disc influence the bending and ultimately the vibration properties, we use the equation for symmetric bending of a clamped disk to estimate the effect of the above parameters on the stiffness of the disk [84]. The stiffness for a circular plate, subject to symmetric bending, of Young's modulus, E, Poisson ratio ν, thickness, t, and radius R is given below:

$$k = \frac{16\pi E t^3}{12(1-\nu^2)R^2} \tag{3.1}$$

This equation provides initial insight into the scaling of bending deflection of circular plates under vibration. Minor changes to the thickness of the disk can be used to tune the stiffness of this disk to match the vibration amplitude range of our motor.

For the experiments described in the following sections, we used the above equation to choose values for R that ensure each disk had equivalent stiffness across tests. We used flexible plastic shim stock material of prescribed thickness, t, and used the derived relationship $k_1 = \frac{t_1^3}{R_1^2} = \frac{t_2^3}{R_2^2} = k_2$ to estimate values for the radius of that will give an equivalent stiffness for fixed thicknesses of flexible shim stock material. For shim stock thicknesses of $t = [101.6, 127, 190, 254, 318]$ um, we calculated the values of $R = [1.75, 2.45, 4.5, 6.93, 9.68]$ cm.

3.2.2 Drive Subsystem

We seek to use vibration-based adhesion for mobile locomotion on vertical and inverted surfaces. The normal interaction force between the vibrating plate and surface is adhesive; thus, a drive system is required to generate traction to move laterally along the surface. We measured the transverse friction due to shear in the thin fluid layer between the disk and an acrylic surface (Figure 3.2). For a polyester disk of radius 4.5 cm, we measured a maximum transverse force of 10 mN. This low friction force is consistent with the fact that gas bearings are often used to

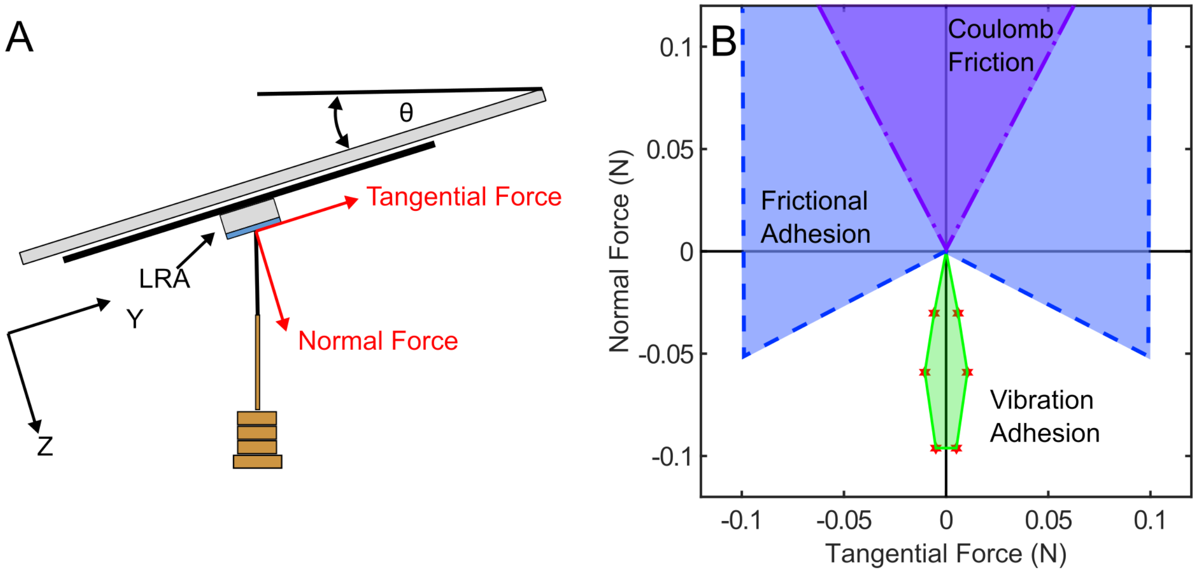

Figure 3.2. Experimental results measuring the maximum available tangential and normal force for vibration-based adhesion in comparison to commonly used adhesive mechanisms. In contrast to other approaches, vibration adhesion uniquely provides strong normal adhesion coupled with low resistance to tangential forces. (A) Tests were performed on an inverted acrylic substrate using a LRA motor on a disk with a radius of 2.45 cm. (B) Experimentally measured limits are indicated by red stars. Force vectors which pass outside the green area cause the disk to slip laterally or detach from the surface. Representative regions of adhesive capabilities are shown in blue for isotropic frictional adhesion and purple for Coulomb friction.

reduce sliding friction in precision machinery. For disks with a larger radius, we could expect this value to scale with R^2 (disk area), but at small disk sizes the mass of the whole system (50-60 g) is an order of magnitude larger then the shear force in the fluid film.

To drive up a wall or across a ceiling using wheeled locomotion, the wheels must be able to generate sufficient traction to overcome any losses due to viscous fluid drag (surface friction under the disk), wheel hub friction, and the weight of the system itself (in the case of vertical climbing). Our measurements of surface friction illustrate that vibration-based adhesion generates low friction, making it suitable for smooth locomotion across vertical and inverted surfaces. To aid motor selection, we developed a simple statics model of the limiting vertical and inverted locomotion cases to determine the necessary torque for the drive motors as well as the necessary normal force at the wheels.

We used a spring element to both isolate the mass of the drive assembly from vibrations and to apply preload to wheels. Additionally, since the disk itself was flexible, the center of the disk was expected to deflect under load. Thus, the spring was required to apply preload continuously throughout the range of deflection of the disk to properly isolate the mass of the drive assembly. Furthermore, the force of the spring was required to either exceed the weight of only the drive subsystem (for the case of inverted horizontal adhesion) or to generate wheel friction that exceeded the total weight of the system as well as the weight of the payload (for the case of vertical climbing).

Inverted Horizontal Case

To evaluate the limits on locomotion on an inverted horizontal surface, we conduct a static force balance. A free-body diagram is included in the Appendix (Figure A1). We find

$$\begin{gathered} \sum F_z = 0 = m_{tot} a_z = F_{adh} - F_n - m_{motor} g - m_{chassis} g - m_{payload} g \\ \sum F_x = 0 = m_{tot} a_x = F_f - F_{shear} \end{gathered} \tag{3.2}$$

where m_{motor} is the mass of the vibration source and flexible disk, $m_{chassis}$ is the mass of the chassis, drive electronics, orthoplanar spring, and the drive motors. F_f is the friction between the wheels and the substrate, F_n is the normal force between the wheels and the substrate, F_{shear} is the lateral force due to shear flow in the thin gas film, and F_{adh} is the adhesive force exerted between the disk and the surface.

From the force balance in x in Equation 3.2, we can see that we only require the friction from the wheels to overcome the shear resistance from the fluid layer. Since the fluid shear force is very small (see Figure 3.2), for motion, we need only ensure the wheels make contact with the surface. The motor choice is then determined by the desired drive dynamics.

Looking now at the force balance in z in Equation 3.2, we see that a higher normal force on the wheel corresponds to a lower payload capability. Due to the inherent flexibility of the disk, we know that the whole system will deflect several millimeters away from the surface when under load. Thus we need to adjust both the preload on the drive wheels as well as the initial deflection of the spring element to ensure that the wheels maintain contact under the full range of possible loads and the corresponding disk deflections.

Vertical Case

The case of vertical climbing in general is more challenging then adhesion to an invered surface due to the presence of moments that cause adhesives to peel off a surface[85]. This can be mitigated by designing a wall-climbing system to keep its mass as close to the surface as possible. For the purpose of this analysis, we omit the moment balance. If we just consider the static force balance (Figure A1) we find

$$\begin{gathered}\sum F_x = 0 = m_{tot} a_x = F_{adh} - F_n \\ \sum F_z = 0 = m_{tot} a_z = F_f - F_{shear} - m_{motor} g - m_{chassis} g - m_{payload} g.\end{gathered} \tag{3.3}$$

From the force balance in x in Equation 3.3, we see that the requirements on motor torque and wheel friction become much stricter than in the horizontal case. The driving friction from the wheels now must overcome the mass of the entire assembly. This case requires a much higher normal force on the wheels than the previous case. Conversely, looking at the force balance in z in Equation 3.3, we now see that the adhesion force only needs to resist the normal force of the drive wheels.

Based on this analysis, there is a clear tradeoff between designing for vertical climbing and designing for locomotion on inverted horizontal surfaces. During vertical climbing, the system requires sufficient preload on the drive wheels to generate enough friction to overcome the mass of the system and some negligible shear force. However, in the inverted horizontal case, any preload beyond that required to overcome the very low shear force will decrease that maximum payload. Thus, the design of the internal spring element will determine the range of surface orientations (vertical, inverted horizontal, etc.) that the system will be capable of traversing and the corresponding maximum payloads for each orientation.

3.3 Results

To investigate the concept of gas-lubricated vibration-based adhesion for robotics, we built two experimental systems: 1) A stationary system, comprising a vibration source and flexible disk, that was used to investigate the adhesive properties of this phenomena; and 2) a mobile system, additionally incorporating a two-wheeled direct drive mechanism with mechanical isolation, that was used to investigate the design considerations for locomotion. The stationary system consisted of a flexible disk made of laser-machined polyester shim stock bonded to an acrylic adapter plate with threaded holes. The vibration source, an ERM motor mounted to a custom printed circuit board (PCB), was then rigidly connected to the acrylic plate via two threaded spacers and lock nuts. Power was supplied to the system via an external power supply unit (PSU). The mobile system used the same elements as the stationary system, but additionally attached a 3D printed chassis containing drive electronics, batteries, a drive train, and a custom laser-machined orthoplanar spring to the custom PCB. Off-the-shelf remote controlled (RC) components allowed for remote operation of the robot. We used the stationary system to measure the adhesive forces, stress, and toughness as a function of disk radius and vibration frequency. We then used the mobile system to test the ability of the system to maintain adhesion while driving over flat and curved surfaces at various inclinations and while dynamically capturing a payload.

3.3.1 Stationary adhesion experiments

Measurement of Adhesion vs Displacement

To measure the normal adhesive strength of the vibrating flexible disk, we quasistatically displaced an inextensible nylon string attached to the center of the disk, away from the surface (at a rate of 0.2 mm/min) until the disk fully detached from the surface. We recorded the maximum adhesion strength while varying two parameters: 1) the driving frequency of the ERM motor and 2) the radius of the disk (Figure 3.4). The adhesive force and displacement were measured with

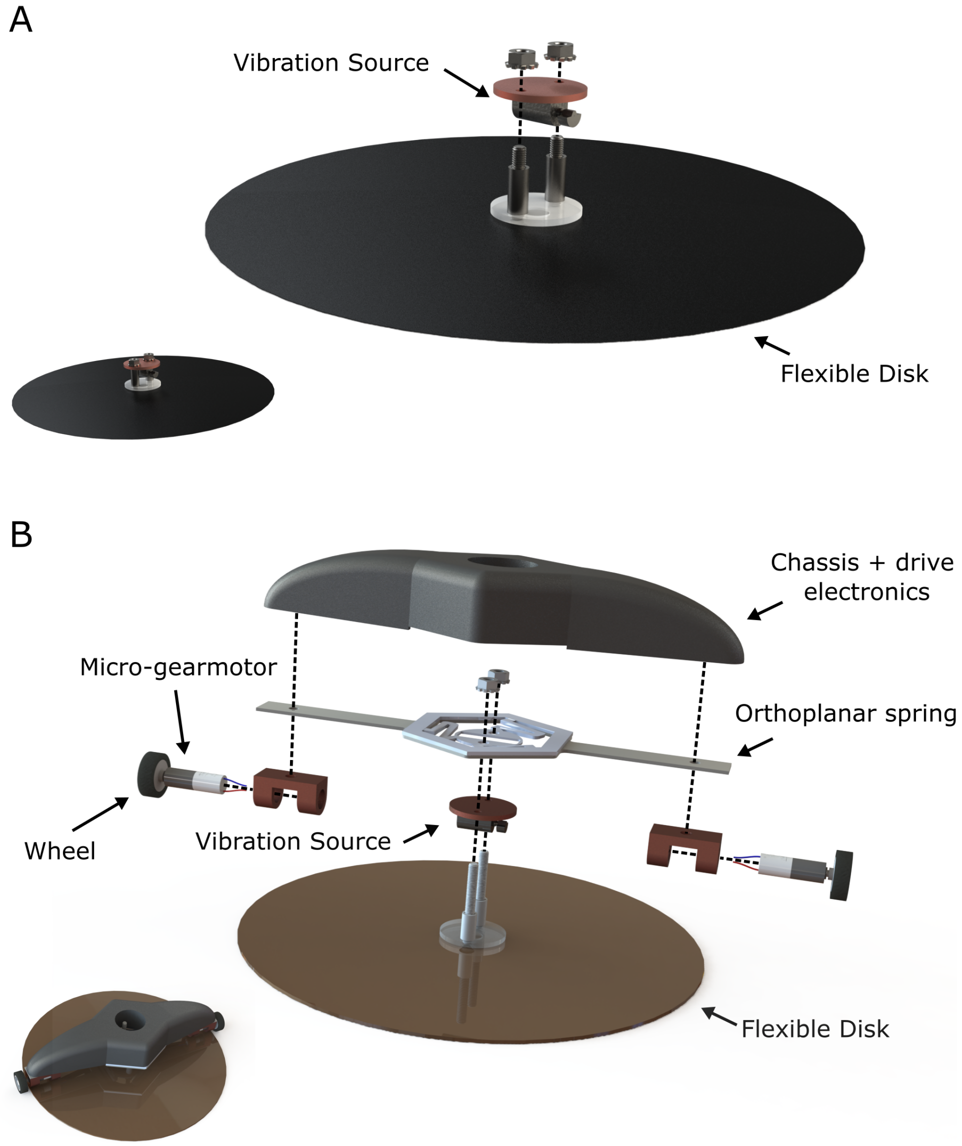

Figure 3.3. Computer-aided design renderings and exploded views of the two systems that were used for experimental testing. (A) The stationary system consisted of a ERM motor that served as a vibration source and an interchangeable laser-machined polyester disk. Power for the vibration motor was provided using an external PSU. (B) The mobile system which additionally incorporated a drive subsystem that was mechanically isolated from the disk and the vibration source. An onboard battery and circuit provided power and remote control functionality.

a tensile tester (3367, Instron). As a substrate for all tests, we chose a 25 cm by 25 cm by 0.65 cm acrylic sheet that was mounted to a fixed aluminum frame using vibration damping mounts. We attached the acrylic substrate assembly to the lower fixture of the tensile tester. The nylon string connected the top of the actuation module to the upper fixture of the tensile tester. We used a nylon string as our top fixture to allow for extension without limiting the ability of the disk to vibrate. Any lateral motion of the vibrating disk on the acrylic substrate was prevented using four metal dowels placed around the edge of the disk.

We measured the effect of frequency on adhesion (Figure 3.4B) using a disk with radius $R = 4.5$ cm. ERM motors provide large vibration amplitudes, but operate over a limited frequency range (approximately 70 to 300 Hz). We observed that when the disk was excited at frequencies below 150 Hz, no adhesion was achieved at this size of disk. To drive our physical system continuously above 230 Hz required driving the motor above its maximum rated power and resulted in failure due to overheating. However, at lower frequencies (below 230 Hz), closer to the maximum rated wattage, we observed no degradation in performance (i.e. the vibration motor operated for 40 minutes without a noticeable reduction in adhesion). Over the first three frequencies tested (174 - 190 Hz), the maximum load increased linearly with frequency; beyond this point, the maximum load settled to a constant value of approximately 5 N. We assume that at approximately 200 Hz, the disk had a natural frequency of vibration, and increasing the excitation frequency beyond 200 Hz decreased the amplitude of the dynamic response of the disk.

By comparing the average maximum load for various disk sizes, we can examine the effect of disk radius on adhesion (Figure 3.4A and 3.4C). Disk thicknesses for each radius were chosen to maintain a constant bending stiffness as predicted by Equation 3.1.

As the disk radius increased, we observed an increase in the maximum load up to a radius of $R = 6.93$ cm, after which the maximum load decreased.

An alternative measure of adhesive capability is adhesive toughness or adhesive energy (i.e. the amount of energy required to induce adhesive failure) [86]. Adhesive toughness is a measure of the robustness of adhesion under dynamic or sudden loading. We observe that the pull-off energy, calculated as the area under the force-displacement curve, as a function of radius follows the same qualitative trend as that for maximum load, but with a more pronounced

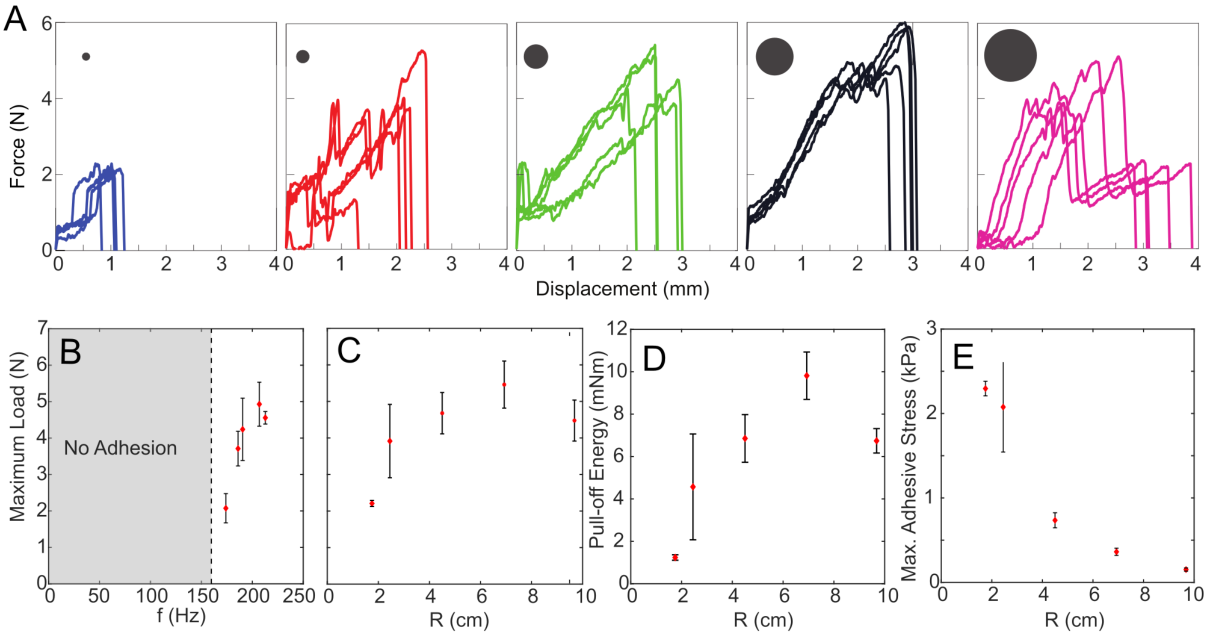

Figure 3.4. Measurement of Adhesion vs Varying Frequency and Radius (A) Effect of radius on maximum normal adhesion force. Adhesion force is measured versus normal displacement for five trials across five different disc sizes. From left to right, disc radius is $R = [1.75, 2.45, 4.5, 6.93, 9.68]$ cm and gray circles show relative (not to scale) disc sizes. (B-E) Experimental results of (B) max load vs ERM motor frequency (n = 3), (C) max load vs disk radius with a fixed disk stiffness (n = 3), (D) pull-off energy vs disk radius, and (E) max adhesive stress vs radius. Error bars represent standard deviation and n represents the number of trials.

optimum at a disk radius $R = 6.93$ cm.

We normalized the maximum supported load by the area of the disk to get a maximum adhesive stress (Figure 3.4D). As the radius was increased, we observed a monotonic decrease in the average value for maximum adhesive stress. Thus, to support higher loads it would be more space efficient to use multiple smaller sized disks then one larger disk (although this configuration would likely be much less energy efficient). In particular, a disk of radius 2.45 cm had approximately an order of magnitude higher adhesive stress than that of a disk of radius 9.69 cm.

For many of the experiments for the stationary system (Figure 3.4), we observed large variation across trials. We expect that this variation is likely due to the randomness inherent in a vibration-based actuation method. Similar to material testing curves we expect to see considerable variations between trials due to an element of stochasticity in the phenomena.

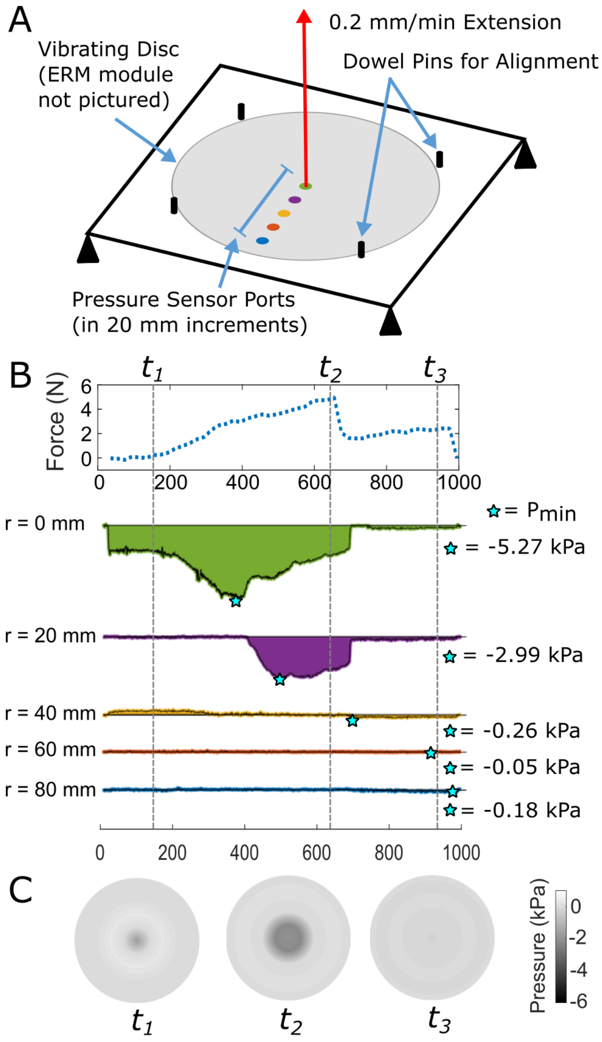

Figure 3.5. Representative trial of an adhesive strength test for a disk with R = 9.7 cm. (A) Schematic of experimental setup. Five pressure sensors were connected to the underside of ports in an acrylic substrate. A fixed extension rate of 0.2 mm/min (applied to the center of the adhesive disk) enforced a quasistatic displacement that increased until adhesive failure occurred. (B) Time series data of force and pressure (at all five ports) for a single trial. A moving average filter (2 s sample window) was applied to the pressure readings to average out any intercycle variations. (C) Snapshots of interpolated pressure gradients (assuming axisymmetric pressure) taken at three times throughout the test. See supplemental video for a continuous visualization of the change in pressure gradient during the test.

Direct Measurement of Suction Pressure and Gap Distance

We measured the pressure gradient in the thin fluid film between the flexible disk and the acrylic substrate with piezoresistive silicon pressure sensors (SSCDANN150PAAA3, Honeywell) at five discrete points along the radial direction (placed in ports lasercut into the acylic substrate at distances in the radial direction of *r* = 0, 20, 40, 60, 80 mm) (Figure 3.5A). The same experimental procedure employed for the adhesion vs displacement tests was used for these tests. An extension test without the ports for the five sensors verified that the addition of the ports did not significantly affect the load bearing capability of the vibrating disk. We sampled pressure sensor readings at a rate of 500 Hz and measured the vibration frequency of the disk with a high speed camera (VEO 410L, Phantom) to be approximately 200 Hz.

From *t* = 0 to 175 s, the tensile tester took up slack in the string. During this time, the disk did not experience any appreciable applied load. Despite this, the pressure distribution in the fluid film under the disk showed significant negative pressure generation at the center (*r* = 0 mm), a slight positive pressure at *r* = 40, and approximately atmospheric pressure at all other sampled locations. At around *t* = 200 s, the system experienced increased loading, and the magnitude of the pressure in the center increased. At *t* = 400 s the magnitude of the pressure in the center decreased and the greater area of the disk experienced negative pressures. We saw this reflected in the sensor placed at *r* = 20 mm. As the flexible disk was pulled farther from the surface, the gradient became relatively flat from *r* = 0 mm to *r* = 20 mm. At *t* = 630 s, (Figure 3.5B) the measured force dropped considerably. The maximum force measured before that time (approximately 5 N) was never recovered. We expect that this was due to a partial detachment event where a larger area of the disk peeled off the surface. Partial displacement would result in decreased tension in the string and a lower force measurement. The system mass was approximately 14 g (not including the power supply); thus the system was able to support a maximum mass of greater than 35× its own weight during the test.

As expected from fluids lubrication theory, the maximum negative pressure occurred at the center of the disk and decreased to atmospheric pressure at the edge of the disk [87]. The localization of the negative pressure, and consequently the load bearing capability, to 4.3% of the total area of the disk (Figure 3.5C) was unexpected. Only after total extension was increased to a critical point (approx. t = 630 s) did the negative pressure gradient became less steep throughout the air film.

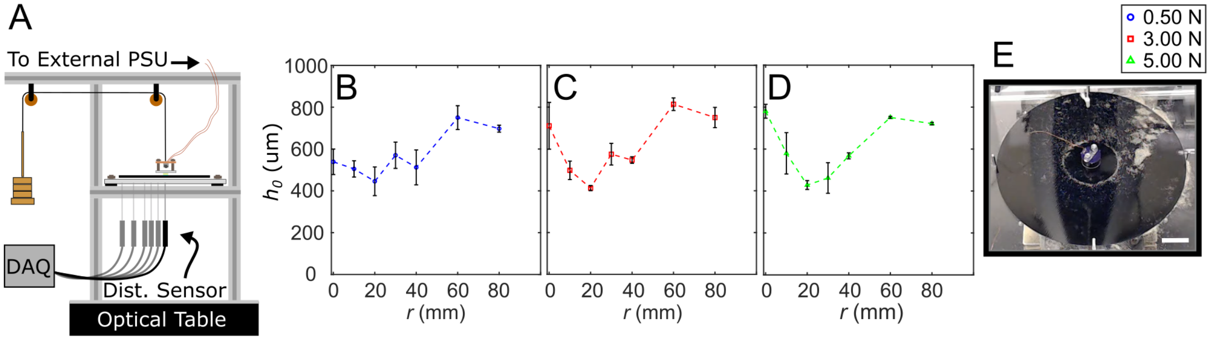

Figure 3.6. Representative data showing steady-state displacement for a R = 9.69 cm vibrating disk subjected to a static load. (A) Schematic of experimental setup. An optical sensor was used to measure both average displacement and vibration amplitude at discrete points (r = 0, 10, 20, 30, 40, 60, 80 mm) along the radial direction. Steady-state displacement as a function of radius for three static loads (B) 0.50 N (C) 3.00 N (D) 5.00 N (n = 10). (E) The Chladni pattern [88] for a static loading test ($F_{applied} \approx 5$ N) revealed areas of low-vibration amplitude where sand collected on the disk. There was a large amount of sand at approximately r = 30 mm, which correlates with the low average displacement at 30 mm for the 5 N loading case.

Using the signal from the pressure sensors, we created an interpolated field of the pressure acting over the full area of the disk. By integrating this pressure over the disk area, we obtained a value for total force that we compared to the force measured by the tensile tester. Prior to loading, the interpolated pressure signal did not show a net suction force on the disk. Once the disk was loaded, the estimated net force on the disk was the same sign and order of magnitude as the value measured on the load cell (Table A1), indicating that the dominant adhesion mechanism is the vacuum pressure generated beneath the disk. It is expected that sampling at more points along the radial direction would result in a estimated net force that is closer to that measured on the load cell.

To further understand how force was generated, we measured the displacement (with respect to the acrylic substrate) of the vibrating disk, subject to a static loading condition. To measure the displacement, we placed fiber optic laser displacement sensors (D21-Q, Philtec, Inc.) through the ports cut into the acrylic substrate and sealed the sensors in place using hot melt adhesive. We measured the steady-state response at seven locations ($r = 0$, 10, 20, 30, 40, 60 and 80 mm) and tested three loading conditions ($F = 50$, 300, 600 g suspended from pulleys) for a single disk design ($R = 9.69$ cm) (Figure 3.6A).

The steady state displacement response (Figure 3.6B-D) showed that at $r = 0$ mm (the point that the load was applied) the overall displacement increased with greater static load. The measured displacement was a minimum at $r = 20$ mm for all loading cases. At $r = 40$ mm, the displacement from the surface was greater, but not as large as the $r = 0$ mm case. Farther out at $r = 60$ mm and 80 mm the thickness of the fluid film was significantly greater than that of the inner-most portions. These displacement responses can be qualitatively visualized using a Chladni pattern [88], which uses fine granular media to visualize vibrational nodes (Figure 3.6E). Sand was poured on the disk during an extension test, performed at a rate of 10 mm/min. At $r = 30$ mm, we observed a circle of sand, indicating a nodal region. The location of the nodal region qualitatively matches where the previously measured pressure gradient is the steepest. It is possible that the presence of a nodal region is limiting the flow of air between the inner region of the disk and the outermost region of the disk at higher loads.

Vertical Climbing of Stationary Disk Design

We observed that for certain disk radii and orientation of the ERM motor, the previously described stationary system climbed up inclines, vertical surfaces, and overhangs. We optically tracked how the linear velocity of a disk with a radius of 1.75 cm ($R = 1.75$ cm) changed as surface inclination increased. For seven different surface orientations (starting at horizontal and ending with inverted horizontal), three trials were performed. The minimum measured velocity (~ 15 mm/s) occurred at 90 degrees (vertical surface). The maximum measured velocity (~ 27 mm/s) occurred at 120 (slight overhang). The inclination dependent velocity measured in these experiments was likely due to asymmetry in the thin fluid film.

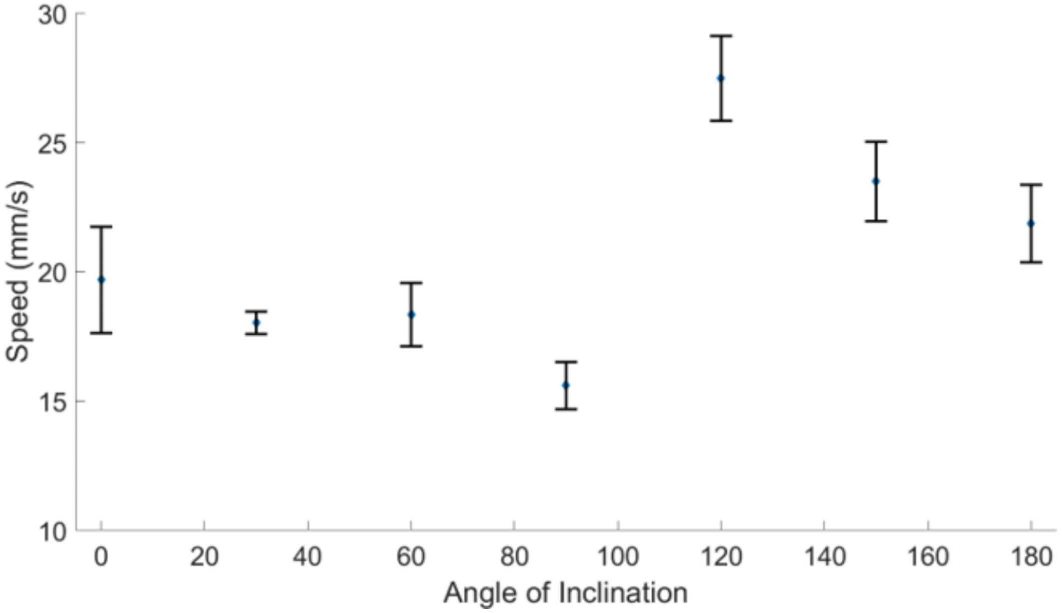

Figure 3.7. Linear Velocity vs Surface Inclination. The surfaces tested ranged from horizontal (0°) to vertical (90°) to inverted horizontal (180°). Three trials were performed for each angle of inclination. The error bars are the standard deviation of the tests.

3.3.2 Mobile Robot Experiments

To understand the capabilities and limitations of this adhesion mechanism for robotics, we used the analyses and experiments described above to design a mobile robot that used the gas-lubricated vibration-based adhesive mechanism. In this design, we added a drive subsystem to the stationary adhesive mechanism described above. We mechanically isolated the drive system from the vibration source to maintain the performance of the adhesive system.

Payload Acquisition

To demonstrate the potential of the mobile adhesive robot to be used in a low-cost gantry-less crane system (e.g. for applications such as warehouse or in-home automation), we tested the ability of the mobile system to dynamically acquire a ∼3.8 N load (a soda can) while adhering to an inverted surface. For this demonstration, the mobile system was equipped with a hook to acquire a payload.

In this experiment, we remotely directed the mobile robotic system to drive along an inverted horizontal surface, hook onto a payload, and drive forward until the payload was no longer supported by an elevated platform. We observed that the dynamic loading caused by dragging the payload off the surface caused the adhesive disk to slide forward and backward along the inverted horizontal surface. This highlights a benefit of using a lubricated adhesion method as the adhesion strength is not significantly affected by transverse loads, such as those imposed by this method of payload acquisition. After the payload was acquired, we were able to resume driving the mobile robotic system along the surface, indicating that the system maintained sufficient pre-load on the wheels.

Previous iterations of the mobile robot design did not have either sufficient pre-load or static displacement of the orthoplanar spring to accomplish this task. When the wheels lost contact due to the acquisition of the payload, adhesion was not stable and failed shortly after payload acquisition (in approx. 5 to 10 s). We believe that when the wheels lost contact with the surface, the mass of the chassis was under-constrained and consequently decreased the amplitude of the vibration of the flexible disk, leading to adhesion failure.

Vertical Climbing

Climbing vertical surfaces poses a specific set of challenges for wall-climbing robots. Perhaps most notably, many adhesion strategies tend to fail due to peeling moments that result from off-axis loads. In this experiment, we drove our mobile robotic system up the side of a wooden cabinet. We started the test by placing the mobile system on the vertical surface with the vibration motor turned on. Pre-load was manually applied to the center of the disk until adhesion was achieved (approx. 5 s). We observed that with sufficient pre-load applied to the wheels via a spring element, we were able to both maintain adhesion and generate enough friction to overcome the weight of the system and drive up the surface of the cabinet. The inherent stiffness

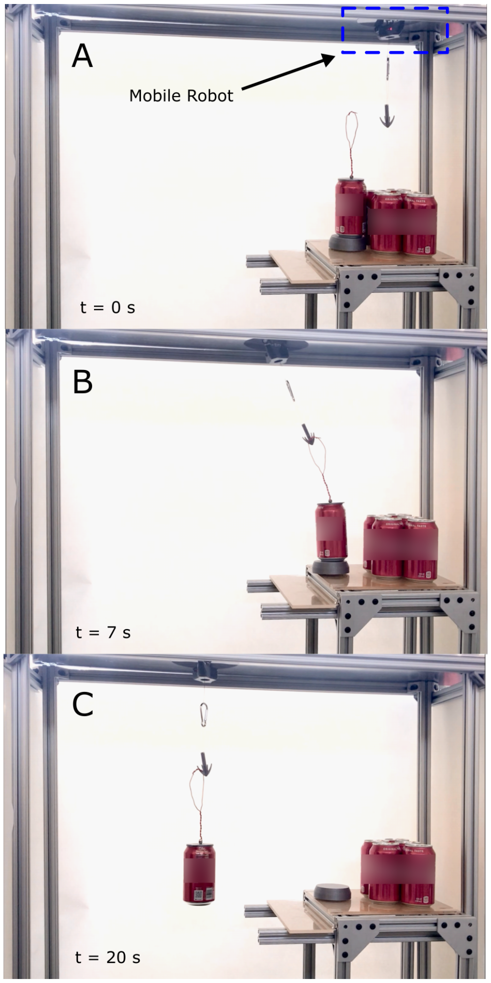

Figure 3.8. Payload-acquisition experiment. By combining the vibrating adhesive disk with a drive system, we created a mobile robot capable of carrying loads untethered on inverted flat surfaces. (A) With the disk vibrating, the robot adhered to an inverted surface. (B) Using two drive wheels pressed against the inverted surface with springs, the robot drove towards a $\sim$5 N [$\sim$ 0.5 kg] load. (C) With a suspended hook, the robot dynamically acquired the load, carrying on a path determined by the differential drive wheels.

of the disk counteracted any peeling moments that could have caused loss of adhesion (previous wall-climbing robots have accomplished the same thing with a pre-loaded “tail” [77]).

Locomotion on Curved Surfaces

In addition to enabling gas-lubricated vibration-based adhesion, we observed that the flexibility of the disk provided robust adhesion to non-planar surfaces with large radii of curvature. To demonstrate this capability with our mobile system, we drove the robot around the interior

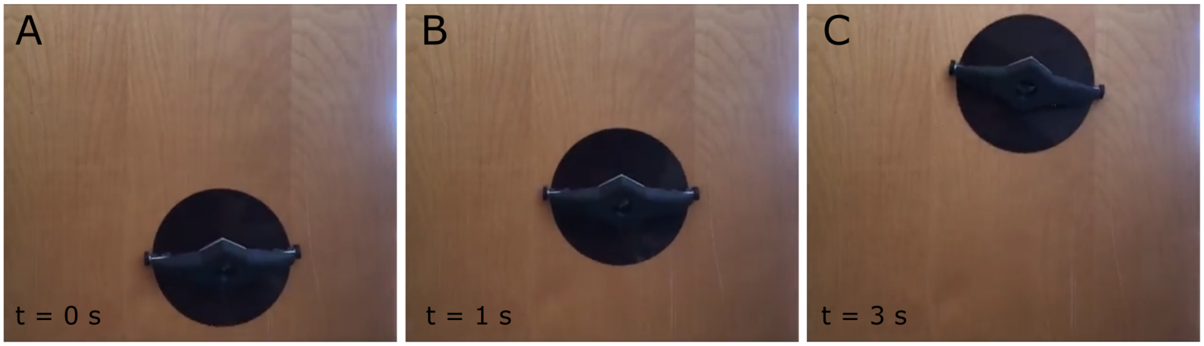

Figure 3.9. Vertical climbing demonstration on a varnished wooden cabinet. An orthoplanar spring provided sufficient pre-load on wheels to enable vertical climbing.

of a horizontal 0.9 m diameter cylinder (Figure 3.10). We began the test by placing the mobile robot at the bottom of the cylinder. We then turned the vibration motor on and applied pre-load manually to the center of the disk until it adhered to the surface. The mobile system drove counterclockwise along the interior of the cylinder in approximately 56 s. Traversing the first half of the cylinder, going from horizontal to vertical to inverted horizontal, took 46 s. Traversing the second half of the cylinder took approximately 14 s. This makes intuitive sense as it is more difficult for the drive motors to work against gravity than with it. Attempts to rotate the mobile system in place on the curved surface using differential drive steering caused the adhesion to fail. Adhesion failure was likely due to our method of mounting the drive wheels, which lacked independent suspension. As a result, any deviation from a locally straight line on a curved surface caused the pre-load to increase past the adhesive strength of the disk.

3.4 Derivation of Vibration Adhesion Equations and Calculation of Stresses

Derivation of Equation 3.8

We can redefine the payload terms in both the inverted horizontal (Equation 3.2) and vertical cases (Equation 3.3) to include the weight of the motor and chassis.

$$\overline{F}_{payload} = m_{payload}g + m_{motor}g + m_{chassis}g \tag{3.4}$$

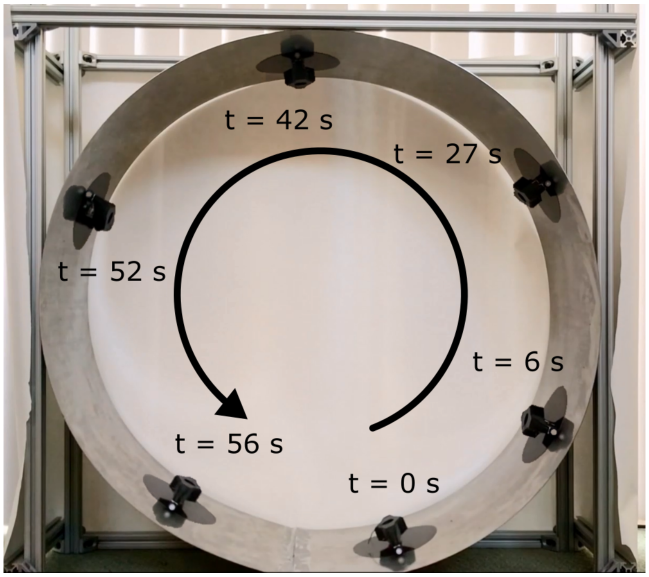

Figure 3.10. Due to the flexible nature of the disk, the mobile robotic system was able to conform to curved surfaces and generate sufficient negative pressures to stay adhered to the inside surface of a horizontal cylinder for a full 360° range of surface orientations.

For the inverted horizontal case we also let the force due to adhesion be the maximum value recorded for the disk. For the inverted case this is written as:

$$\overline{F}_{payload} = F_{max-adhesion} - F_n. \tag{3.5}$$

For the vertical case this is written as:

$$\overline{F}_{payload} = \mu F_n. \tag{3.6}$$

Setting the normal force from both Equation 3.5 and 3.6 and simplifing we arrive at Equation 3.8.

Calculation of Specific Adhesive Stress from [15]

We calculated the specific adhesive stress from the data presented in Table II of the manuscript for a single zero pressure difference (ZPD) suction unit. Of the three configurations of ZPD suction units presented in the table, the one with the highest specific adhesive stress

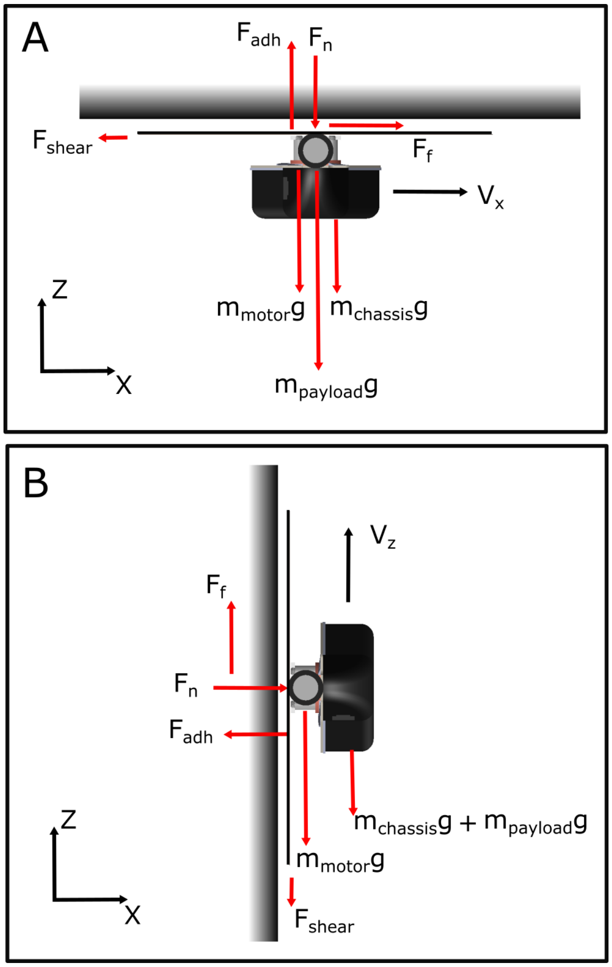

Figure 3.11. Simplified free body diagram to compare forces for vertical climbing and adhesion to inverted horizontal surfaces (A) Inverted Horizontal Case (B) Vertical Case

(Robotic arm) is used for comparison. Consequently, we used $R_0 = 65$ mm to calculate the total area of the suction unit, $m = 0.8$ kg as the mass of the unit, and $F_s = 267$ N as the adhesive force.

$$\frac{\sigma_{max}}{m_{assembly}} = \frac{F_s}{m\pi R_0^2} = 25.1 \text{ kPa kg}^{-1} \tag{3.7}$$

Table 3.1. Sampling discretely at different times during the test shown in Figure 3.5, we can use the linearly interpolated pressure signal to estimate the proportion of the load that is supported by the negative pressure in the thin fluid film.

Time (s)	$P_{r=0}$	$P_{r=20}$	$P_{r=40}$	$P_{r=60}$	$P_{r=80}$	$F_{interp.}$ **(N)**	$F_{r=0}$ **(N)**
200	-2.51	0.4	0.21	0.04	0.06	1.33	0.46
400	-3.74	-1.94	0.01	0.27	-0.23	-7.23	3.09
600	-1.83	-2.1	-0.05	0	0.03	-6.41	4.35
900	-0.03	-0.05	-0.09	-0.04	-0.24	-3.08	2.12

3.5 Discussion

3.5.1 Payload for both vertical climbing and inverted horizontal case

The maximum payload the mobile system could support while traversing both inverted and vertical surfaces was limited primarily by the maximum adhesive force that the disk was capable of generating and secondarily by the coefficient of friction between the wheels and the surface material.

$$\overline{F}_{payload} = \frac{\mu F_{max-adhesion}}{(1+\mu)} \tag{3.8}$$

Analytically, we can see that as the magnitude of μ increases, the normalized payload force approaches the maximum adhesion force. However, it is unlikely for μ to be much larger than one. Assuming a value of approximately unity for μ, we see that the maximum payload force for both inverted horizontal and vertical locomotion is approximately half the maximum adhesion force that the disk is capable of generating. If operation were limited to either vertical climbing or inverted horizontal operation, then the payload could match the maximum adhesive force, with some small offset for system mass.

3.5.2 Scalability of the size and number of adhesive disks

A disk of radius 6.93 cm performed the best for both the maximum supported load and maximum pull-off energy; however, the disk with the smallest area had the highest adhesive stress. Depending on the application, it could be advantageous to combine several disk geometries to achieve the desired load capacity and resilience to disturbances.

Due to the relatively low viscosity of air, we expect that as the radius of the adhesive disk decreases, the weight of the vibration source starts to exceed the adhesive strength of the disk. This limitation could be addressed by employing alternate excitation strategies such as piezoelectrics. As the radius of the disk is increased there are several factors that could limit the maximum achievable adhesion force. It could be that more viscous losses are introduced as the disk radius increases and so we do in fact get maximum adhesion for a relatively small disk. Alternatively, if we assume that the size of the vibration source would need to be scaled up as the radius of the disk is increased, we might expect the mass of the system to scale with l^3 whereas the adhesive strength of the disk will scale with l^2.

3.5.3 Limited frequency sweep and dynamic response

Due to our choice of vibration motor, we were limited in the frequencies we could test. At low voltages, the motor generated low frequency vibrations but adhesion was not successful. At voltages higher than 5 V, the motors failed due to overheating, as they were being operated continuously above their maximum rated power. Future work could use different actuators to investigate a wider range of frequencies and the corresponding dynamic responses of the disk.

3.5.4 Substrate Roughness

The surfaces used for this work were relatively smooth and lacked significant asperities. Qualitatively, we found that the system adhered only to relatively smooth surfaces (acrylic, medium density fiberboard, curved, sheet metal, glass), but not rougher surfaces (e.g. stone, bricks, open cell foam). In our experiments, we measured the maximum fluid layer thickness to be 800 μm. We found surface roughness to effectively increase the thickness of the fluid layer, consequently limiting the maximum supportable load. We leave a detailed investigation of the effect of surface roughness to future work.

3.5.5 Limitations of Vibration-based adhesion

As discussed in this paper, gas lubricated vibration-based adhesion is promising for robotic applications, but also faces some fundamental limitations. First, the vibrations required for adhesion are within the range of audible frequencies and as a result, robots that employ this mechanism are inherently quite noisy (during testing our system produced a maximum of 88.9 dB(A) of mechanical noise). One solution would be to use these robots in spaces that are not occupied by humans. Another would be to add a noise barrier such as noise insulation foam. Another limitation is that to stay adhered to a surface this system requires energy to be continuously expended, in contrast to controllable adhesion techniques such as dry fibrillar adhesives which passively adhere and require energy expenditure for removal. We additionally found that our system was robust to minor voids in the substrate, but failed to maintain adhesion on very porous materials such as open-cell foam. Furthermore, it is unclear whether this adhesion method would work underwater or in a liquid working medium rather than a gas. We expect that both the stiffness of the disk and the amplitude of the vibration force would need to be scaled appropriately to compensate for strong hydrodynamic forces. If these adaptations were successful, they could open up a wide range of additional use cases for underwater adhesion.

3.6 Conclusions

In this work, we presented and characterized a novel, controllable adhesion method for robotics with high specific normal adhesive stress (i.e. $\sigma_{max}/m_{assembly} = 26.2$ KPa/Kg for our prototype system), comparable to other methods (active suction: $\sigma_{max}/m_{assembly} = 25.1$ KPa/Kg [15] and hybrid electrostatic and gecko-inspired adhesive: $\sigma_{max}/m_{assembly} = 25.7$ KPa/Kg [85]). In contrast to other controllable adhesion techniques in the literature (e.g. those based on dry fribrillar adhesives, magnetorheological fluids, or electroadhesives), the system was simple to manufacture and leveraged commercially available components to generate high specific normal adhesive stresses with low resistance to shear motion. In our experiments measuring pressure distribution, we observed that the negative pressure produced in a small central region of the vibrating disk balanced the applied load. In the experiments measuring the displacement of the disk, we saw that the delineation of the inner region and outer region approximately matched the location of the minimum fluid film thickness. Additionally, we experimentally observed that axisymmetric vibrational patterns are not a necessary condition for adhesion. We hypothesize that the flexibility of the disk allows for the formation of these nodal patterns under a relatively small excitation force, and that these nodal regions enable the generation of a small adhesive region at the center of the disk by limiting the flow of air between the inner and outer regions. Further work remains to be done to fully quantify the effects of surface roughness and curvature on adhesion. To allow for this adhesion technique to support larger loads for applications such as warehouse fulfillment or in-home automation, a better understanding of the scalability of this effect with the size and number of adhesive disks is needed.

Chapter 3, in full, is a reprint of the material as it appears in Advanced Intelligent Systems 2021. Weston-Dawkes, W.P.; Everman, M.; Gravish, N.; Tolley, M. T.; The dissertation author was the primary investigator and author of this paper.

Chapter 4

Intracorporeal Variable Stiffness Retractor

Retractors for laproscopic surgery face competing challenges: they must be sufficiently soft to be (1) deployed and removed through a small opening and (2) to be manipulated into a desired configuration, but also (3) sufficiently rigid to affix tissue during an operation. Existing designs focus on one of these requirements, but generally fail to achieve all three. We developed a soft foldable retractor that addresses all three of the above requirements by changing its flexural stiffness from relatively soft to relatively rigid by making use of an effect known as layer jamming. In the soft state, it can be folded and inserted through a small opening, and manipulated by laproscopic tools into a desired configuration, and then jammed into a rigid state to retract tissue during an operation. In this work we examine the ability of this jamming retractor to address the challenges of access, atraumatic anchoring, high-force retraction, and removal. We model the jamming phenomena to predict the maximum load a deformed layer jamming device can support and we compare this to experimental data. We use the geometric constraints imposed by a trocar to understand the fundamental limits on the maximum supportable load. We show that jamming-based approaches require a 10 mm trocar or bigger to be able to support 7.5 N loads (the estimated load of a human liver). In contrast to existing laparoscopic retractors, we present a solution to atraumatic anchoring within the body through the incorporation of a patterned high-friction surface. We measure the effect of patterning, surface condition, and preload. Finally, we quantify how the force required to remove the device from the abdominal cavity can be greatly reduced with features that cause the device to self-fold while passing through the trocar. These results allow us to assess the perioperative viability of our device for use in laparoscopic surgical procedures involving liver retraction.

4.1 Introduction

Retraction, the act of holding back underlying organs and tissues so that body parts underneath can be operated upon, while straightforward for open surgery, is a significant challenge for minimally invasive surgery (MIS). The retractors used for open surgery are too big to pass through the small incisions used in laparoscopic procedures [52]. Retractors specific for MIS (such as a paddle [53] or a Nathanson liver retractor [54]) have been developed for laparoscopic procedures, but they possess several key limitations: they (1) require a dedicated incision; (2) dependency on the location and size of the incision; (3) require an additional surgeon or external anchoring to maintain retraction, (4) must apply concentrated forces to retract larger internal organs, such as the liver or bowel. Many of these concerns are tied to the inherent rigidity of the available tools, which prevent the surgeon from flexibly accessing the operative site and minimizing additional trauma [55]. Thus, there is a need for soft or variable stiffness retractors that can adapt to the large variety of situations that surgeons may experience in the operating room.

To that end, several research groups have focused on creating variable stiffness tools for MIS. These devices can change between a soft state, for low force manipulation by laparoscopic tools, and a rigid state, to hold organs in place during an operation [34]. The STIFF-FLOP project [89, 90] incorporated both soft active control, via fluidic actuators [32], and variable stiffness structures, via granular jamming [36]. This allowed them to pump fluid into the actuators to direct their device within the body and also apply a vacuum to the granules in the main structure of the device to freeze it in place for a surgical procedure. Several other groups have investigated layer-based jamming [40] for endoscopy [91] and retraction [92]. Rather than a collection rough particles (e.g., coffee grounds), that stiffen when confined in a granular jamming system, layer jamming uses stacks of high-friction layers in an airtight pouch to achieve a similar effect. Layer jamming thus provides an advantage over granular jamming in bending because when granules contained in a soft membrane are in tension, they will tend to unjam [37]. However, layer jamming based-devices are generally limited to bending and twisting deformations (whereas systems based on granular jamming tend to be suited for compression loads). Thus the particular use case for each jamming method should be chosen to take advantage of their strengths. One strength that has not previosly been explored is the potential of miniaturization for layer jamming.

While previous work has explored the promise of jamming based techniques for variable stiffness robotic MIS systems, they have not satisfied the requirement to pass through small laproscopic ports. Folding-based approaches can help address this challenge. Origami and folding-based devices have been widely proposed for minimally invasive procedures due to their ability to change from a compact package to a larger functional shape. One such design involved ingesting a pill with a robot that deployed into a larger functional shape within the body for the purpose of patching stomach wounds [93]. A pneumatically actuated origami-based retractor for single-port laparoscopy has also been developed [94]. One of the fundamental challenges of designing origami-inspired robots and mechanisms, a compared to traditional rigid robots, is that both the deployed 3D shape and the original 2D geometries are tightly integrated with material choice, mechanism design, and fabrication methods [95, 96]. Origami-inspired approaches have also been combined with layer or laminar jamming techniques to take advantage of both the intrinsic change in stiffness from jamming, but also increases in stiffness due to changing between different folded configurations [97]. Banerjee *et al.* [98] developed an origami fan inspired retractor with layer jamming elements. This design had built-in tactile sensing, which aimed to reduce trauma to the patient, but its large overall size limited its applicability to MIS. Folding-based approaches [56] have been demonstrated to improve access during minimally invasive procedures, but there have been no previous works that solve both access and retraction for traditional laparoscopy.

In this work, we present the engineering design and analysis of a foldable layer jamming soft retractor targeting traditional laparoscopy (where all devices must pass through a trocar with diameter 12 mm or smaller). We focus on the particular task of retraction of the liver for upper gastroinstestinal (GI) surgeries as the liver presents a particularly challenging (i.e., large) loading case. The paper presents the following contributions: (1) analysis of design considerations for access, deployment, and removal (2) a method for the fabrication of the proposed retractor [99] (3) comparisons between the predicted and experimental performance of the retractor during retraction, anchoring, and removal. The above contributions serve to investigate how the interplay of the operational requirements (i.e. insertion, deployment, and removal) of laparoscopic surgery affects the space of feasible variable stiffness retractor designs.

4.2 Design Considerations for Laparoscopic Retraction

A surgical device used in laparoscopic surgery must (1) be able to pass into the abdominal cavity, (2) perform it's designed function, and then (3) be easily removed from the body. For existing rigid surgical instruments, there exist a discrete number of controllable degrees of freedom, making them predictable in their behavior, but limited in terms of possible configurations. However, soft devices have infinite degrees of freedom. While this affords unprecedented flexibility during deployment within the body, it creates unique challenges especially when fulfilling geometric requirements imposed by (1) and (3). The interplay between geometric constraints and other performance requirements provide unique design considerations for soft surgical devices.

4.2.1 Geometric Constraints of the Trocar

One of the core principles of MIS is that by minimizing trauma to a patient, it is possible to decrease the risk of post-operative complications, to speed up recovery times, and to reduce the lengths of hospital stays [55]. In extraluminal surgery, surgeons create small incisions

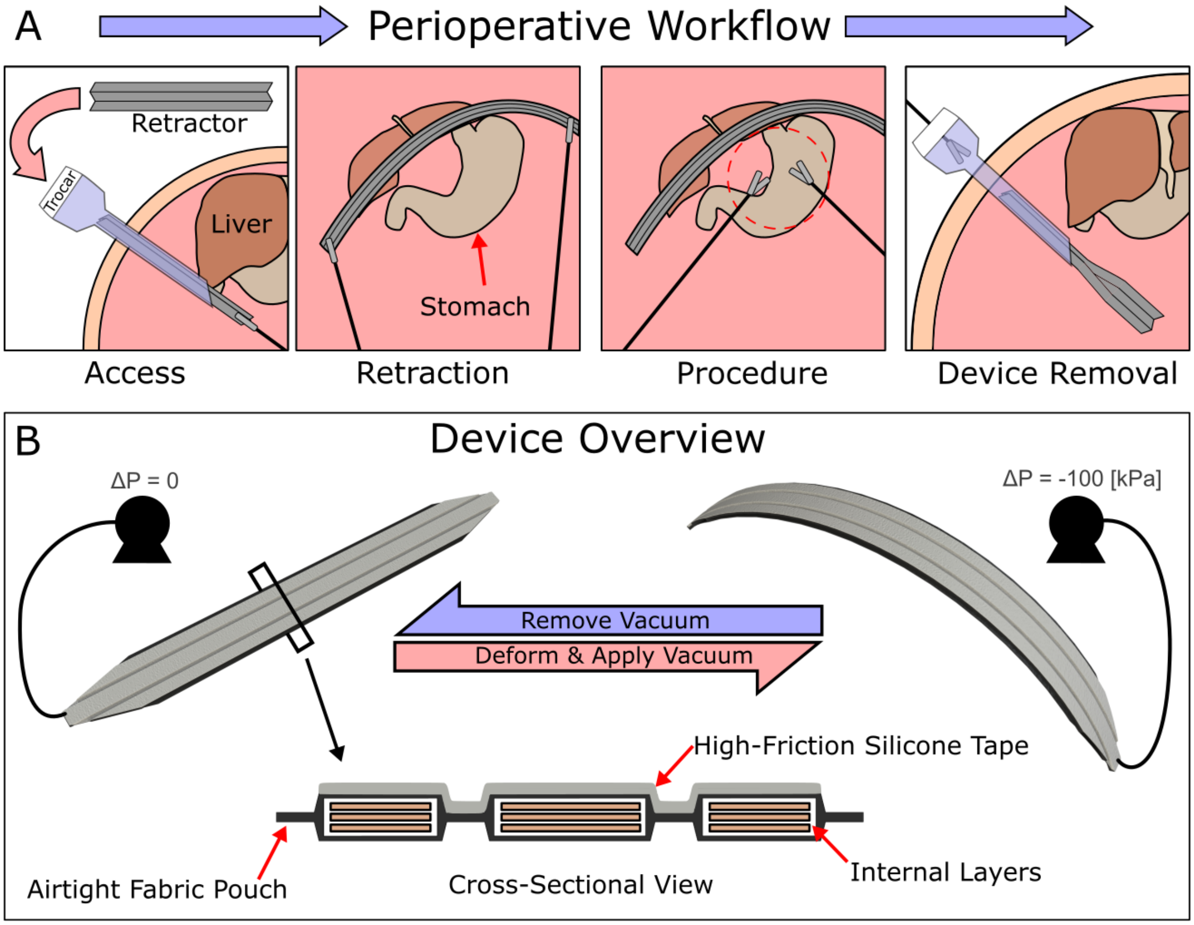

Figure 4.1. Envisioned workflow and principle of operation for variable stiffness soft retractor (A) The retractor first folds down to a small size to be inserted via MIS port. The surgeon manipulates the device into place and then jams the device to hold state. The surgeon completes the procedure and removes the device through the original port. (B) The overall stiffness of the device is controlled by an external vacuum pump. When a vacuum is pulled, the ambient atmospheric pressure causes the layers to jam together, freezing the device in position. To atraumatically anchor against the abdominal wall, we designed a high-friction patterned silicone surface on one side of the device. The device is comprised of three discrete jamming sections, which allow the device to pass through a trocar.

where they insert temporary ports, called trocars. Trocars are the main tool through which a surgeon insufflates the body cavity and passes surgical tools and cameras into the body during a laparoscopic procedure. The diameter of the trocar is dependent on the type of tool required for the procedure. For surgeries using trocars with outer diameters less than 10 mm, the trocar can be removed after the surgery and incisions are left to heal without further intervention. However, for larger trocars, it is recommended to suture the incision closed – with bigger holes there is greater risk for complications. This additional step adds more potential risk for post-operative complications and simply increases the time to complete a surgical operation.

Given these constraints, the design of a soft device passing through a trocar should seek to minimize the required trocar diameter, with special consideration towards developing a device smaller than 10 mm. Due to the goal of achieving a small cross-section, we chose to focus our analysis on a device with three sections that folds up into "Z" or accordion shape to pass through the trocar. We explored incorporating additional actuation into the device, but the limitations of the cross-sectional area of the trocar meant that any space devoted to actuation of the device would come at the cost of load bearing capability.

4.2.2 Loading due to Organs and Effect on Jamming Performance

To better understand how the retractor performs when it is deployed within the body, we want to predict how much the device deflects, when jammed, under loading by an internal organ (e.g. the liver or bowel). Any significant deflection (e.g. greater than 1 cm) is undesirable as the operation site could become blocked. When loaded, a jammed device transitions between fully jammed elastic deformation (i.e. no relative movement between layers) and fully unjammed plastic deformation (i.e. relative movement between all layers). Since the maximum acceptable deflection is small, we chose to model deflection from zero deflection to the deflection corresponding to the onset of plastic deformation in the device.

To predict the onset of plastic deformation in a jamming beam (i.e. when the internal transverse shear stresses exceed the frictional resistance between the layers), we use the formula presented in Jadhav *et al.* [37]

$$\tau_{induced} \leq \mu_s \Delta P \tag{4.1}$$

where $\tau_{induced}$ is the internal transverse shear stress induced via external loading, μ_s is the coefficient of static friction, and ΔP is the pressure experienced by the jamming layers. When the left and right side of EQ. (4.1) are equal, we expect to observe a transition in structure behavior from behaving as a bulk material to behaving as an arrangement of parallel structures, resulting in a decrease of stiffness. For a cantilever beam, we expect the difference between the stiffness of the jammed structure, compared to the unjammed structure, to vary with n^2 where n is the number of internal jamming layers. Thus, for a fixed device thickness, we can increase the number of layers to ensure that the unjammed state requires low force to manipulate and has no potential to bruise or damage any internal organs during positioning.

4.2.3 Anchoring within the Abdominal Cavity

Another significant consideration for deployment is how the device is anchored within the body. The prediction from the previous section will only be valid if the device has sufficient anchoring to prevent it from slipping out of place when loaded. There are a number of both internal and external anchoring methods that have been used to anchor retractors in position for laparoscopic procedures. The primary advantage of internal anchoring over external anchoring is that the latter often requires additional incisions or trocars. Existing internal anchoring methods include suturing or clipping the device to the abdominal wall [92]. To develop an atraumatic anchoring method, we took inspiration from metal retractors used in open surgery which lift organs and rest against the abdominal wall. For MIS applications, we enhanced the gripping ability of the device to stay fixed to lubricated surfaces. We designed a patterned high-friction tape that channeled fluid away from the interface between the abdominal walls and our retractor, much like the treads in car tires allow for contact between the rubber wheel and the asphalt even during wet conditions.

4.2.4 Removal via Induced Folding

Removal of an underactuated soft retractor provides a completely different set of problems as compared to deployment; the difficulties of removal are often neglected or ignored in discussions of other soft MIS systems. While it is straighforward for a surgeon to fold our retractor by hand for insertion, it is near impossible for the surgeon to re-fold the device inside the abdominal cavity using laparoscopic tools. Rather than adding another active component to the device to aid in removal, we found that we could take advantage of the interaction of one end of the retractor with the beveled end of the trocar. A trocar ends in 45 degree bevel, which aids in the process of passing through the abdominal wall. We found that by adding a taper to the end of the device, we could get the device to self-fold into the original accordion shape as we pulled it against the trocar while rotating the device about it's long axis. This finding was particularly exciting because a simple change in the base geometry (i.e., adding a tapered end to the retractor) gave it a completely new behavior.

4.3 Fabrication of Retractor

The previous section addressed high level design considerations and constraints associated with retractors designed for MIS, particularly laparoscopy. We briefly presented our overall approach. In the present section, we present fabrication details for the variable stiffness retractor.

4.3.1 Layer Jamming Chamber

To fabricate the main body of the retractor, we laser cut two layers of airtight heat-sealable taffeta fabric (4.3 oz/sq. yd., Seattle Fabrics), a single layer of high-temperature plastic film (to use as a mask during the heat-sealing process), multiple layers of matte plastic film to use as the internal jamming layers, and a single layer of patterned silicone tape.

The layers were aligned using external features and heat sealed using a heat-press (at 350°F), leaving each tapered end open. The internal mask was removed, and stacked jamming layers were inserted into each of the three sections. A rubber tube was inserted into a laser-cut hole in the taffeta and sealed with hot-melt adhesive. Then each end of the device was sealed and checked for leaks, after which the patterned silicone tape was adhered to one side of the soft retractor (Fig. 4.1B).

4.3.2 Patterned Silicone Tape

Animals such as tree frogs [100], clingfish [81], and remoras [80] employ soft microstructures adapted from existing anatomy to improve capillary adhesion and ensure effective adhesion under wet surface conditions.

Choosing patterns inspired from nature and previous scientific works, we patterned high-friction silicone tape (JemmTrac 4563 Traction Tape, Jemmco) using a laser micromachining system (PLS6MW, Universal Laser Systems) and adhered the tape to one side of the main body of the retractor. After rastering, a vector cut was used to cut the outline. The tape was then removed from the acrylic backing and attached to the retractor.

4.4 Modeling Trocar Imposed Limitations on Performance

In this section, we aim to concretely assess how the geometric constraints of the trocar affect the range of feasible retractor designs. For simplicity, we are assuming that the device is comprised of one or more parallel sections that are folded manually to fit through the trocar at the start of the surgical procedure. We start by performing a finite element analysis (FEA) to find designs that fulfill design criteria and then we experimentally test a subset of those designs to see if they meet the criteria.

4.4.1 FEA Methodology

From the analytical relationship EQ. (4.1), we know that the onset of plastic deformation in a jamming device depends on the maximum transverse shear stress,$\tau_{induced}$, the static coefficient of friction, μ_s, and the pressure difference, ΔP. For a given material, the best ΔP we can achieve is dependent on atmospheric pressure, approximately 100 kPa. We assume the retractor is jammed in the shape of a circular arch. Thus, we want to understand the distribution of transverse shear stress in a circular arch. While an analytical formulation for a circular arch with clamped edges exists [101], we chose to use FEA instead. As human anatomy can vary

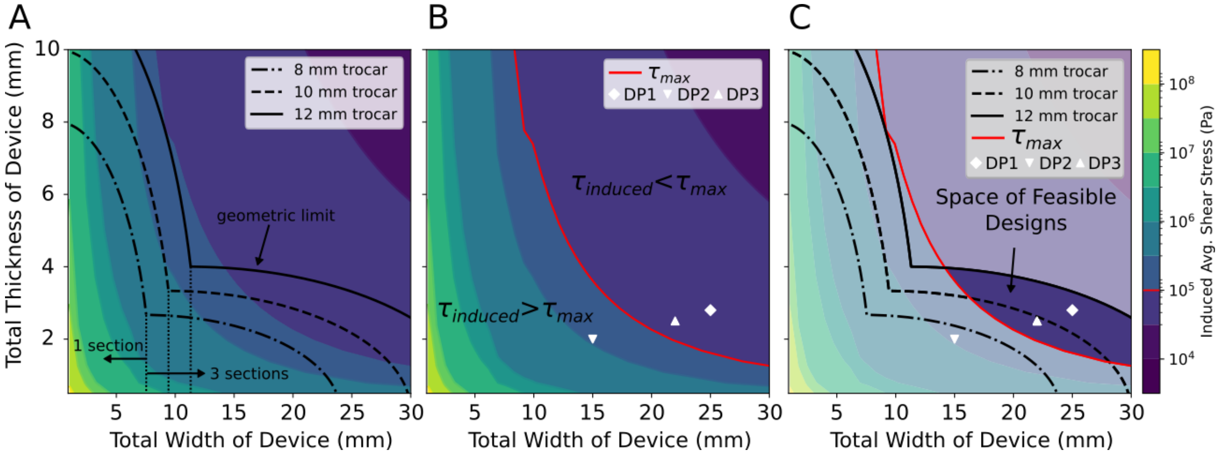

Figure 4.2. To determine the limits of performance of the retractor when jammed into an arch, we used FEA to calculate the internal transverse shear stress induced by a 7.5 N load over a range of device widths and thicknesses. (A) Different geometric constraints due to laparoscopic ports are shown with black lines. Acceptable geometries fall below and to the left of the black lines. Also shown is when a device needs three sections, and thus folding, to fit through the trocar vs one section. (B) The critical shear stress, τ_{max}, is shown as a red line dividing device geometries that will stay fully jammed from those which will have slip between layers. Three design points are highlighted, two of which were expected to adequately support a 7.5 N load, and one which was expected to plastically deform. (C) Critical geometric and performance limits from (A) and (B) are overlaid to show the region of feasible designs.

widely between individuals, the use of FEA would enable this approach to be more widely applicable in future work.

As viewed from above, the liver is composed of two lobes (left and right). For laparoscopic upper GI surgery, we need to be able to retract the left lobe of the liver. To roughly estimate the proportion of the liver weight we need to support, we model the liver as a propped cantilever beam. Assuming the mass of the liver is 1/3 of its width away from the wall, we find the reaction force on the retractor to be 2/3 of the liver's total weight. For standard liver weights in the adult population, we calculated the expected load due to the left lobe of the liver to be approximately 7.5 N.

When comparing the FEA results to experimental results, we can treat the jammed retractor as behaving like a solid arch. We then predict the deflection behavior based on the maximum deflection observed at the center of the simulated arch due to loading up to 7.5 N.

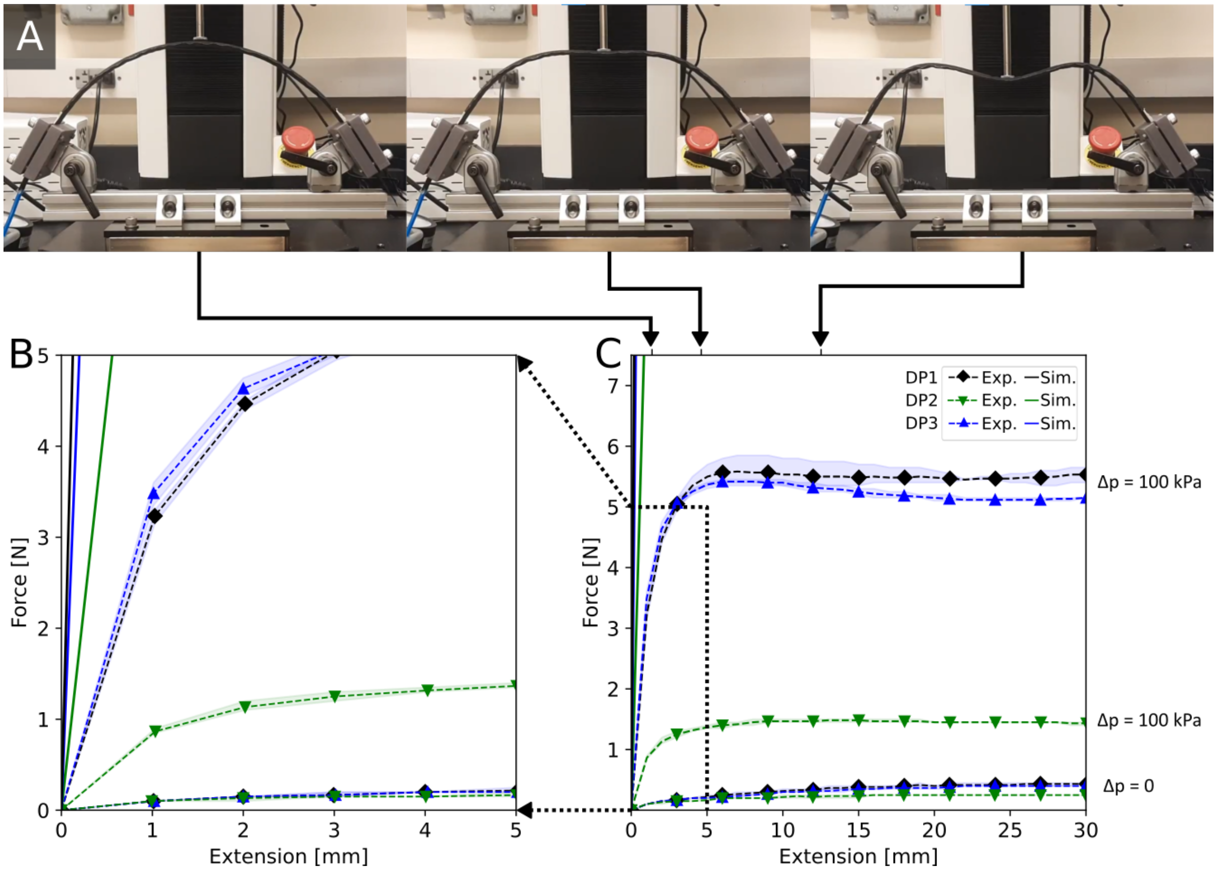

Figure 4.3. To validate the predictions made during FEA modeling, we performed experimental tests using previously defined design points (Fig. 4.2B). (A) A retractor with clamped ends was placed into an arch shape and was quasi-statically deformed and the reaction force measured. (B) Results shown in (C) are magnified to show initial force-deflection behavior. (C) Experimentally measured force-displacement curves for devices corresponding to design points (DP1, DP2, DP3), loaded in both the jammed ($\Delta P = 100kPa$) and unjammed ($\Delta P = 0kPa$) states. Also plotted is the FEA force-deflection prediction for a jammed beam, modeled as a bulk material, to compare the the initial slopes measured experimental.

4.4.2 Experimental Methodology

To compare the predictions of our FEA model to experimental data, we performed a quasi-static three-point bending test of the retractor (Fig. 4.3A). A 1 mm/s deflection was applied and the resultant force was measured for three devices with different widths and thicknesses. Each device was tested in both the jammed (ΔP = 100 kPa) and unjammed state.

4.4.3 Results

Overlaying the geometric limits imposed by trocars of varying diameters highlights the transition from a device with one section to a device with three sections (Fig. 4.2A). Just this information on it's own is not sufficient to conclude how many sections are necessary for this device, it merely provides an upper limit on acceptable geometries. needs to be concurrently considered with the performance required during deployment within the body.

We calculated the maximum acceptable internal stress (Fig. 4.2B) using Eqn. 4.1, which gave us a maximum induced shear stress, τ_{max}, on the order of 10^5. For the purpose of comparison to experimental data, we define three design points (DP1: (W = 25 mm, t = 2.8 mm), DP2: (W = 22 mm, t = 2.5 mm), DP3: (W = 15 mm, t = 2 mm)). Design point 1 and 3 are designed to fit through 12 mm and 10 mm trocars respectively and support a 7.5 N load, but design point 2 only satisfies the geometric constraints of the trocar.

By overlaying the two constraints of trocar size and jamming failure (Fig. 4.2C), we see that a jamming device with one rectangular section does not provide enough beam material in terms of either the width or the thickness to limit the maximum transverse shear stress. Based on these results, we concluded that a device with three parallel sections was necessary to hold the predicted load of the liver. we see that designing a retractor of this design to fit through a trocar with a diameter of 8 mm is not feasible for an estimated load of 7.5 N. A 10 mm trocar is barely within the acceptable performance regime, and a 12 mm trocar has a much wider set of acceptable designs.

4.4.4 Discussion

We are not just taking advantage of layer jamming–the shape that a surgeon manipulates the device into, a circular arch, changes the distribution of the induced stresses. Also, since the original layers are flat, we also expect the device to reach jamming failure at a lower loading condition as the individual layers want to spring back into their original state.

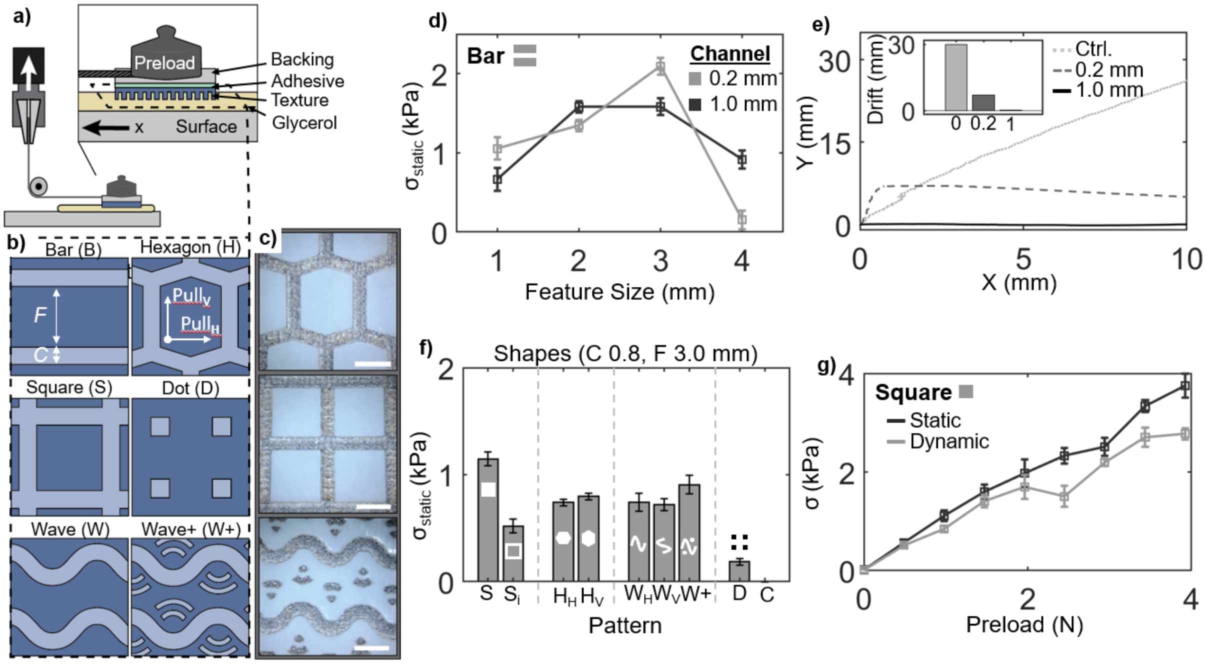

Figure 4.4. Design and quantification of the friction pads. a) A schematic of the experimental setup of the friction shear tests. Inset: A frictional texture is adhered to an acrylic backing. b) Schematics of the frictional textures are represented as follows: Bars (B), elongated hexagons (H), squares (S), discrete dots (D), wave patterns (W), or fingerprint-inspired wave and concentric circles (W+). Subscript H denotes that the texture was pulled horizontally, orthogonal to the direction of elongation. Subscript V denotes that the texture was pulled vertically, along the direction of elongation. c) Micrographs (top to bottom) of elongated hexagons, squares, and wave+. Scale bar, 2 mm. d) The effect of feature size (mm) on the static shear stress (kPa) of the frictional texture, performed for a horizontal bar texture with a channel width of either 0.2 mm (light gray) or 1.0 mm (dark gray). e) Visual tracking and characterization of drift of the surface textures during an x-displacement of 10 mm. X and Y positions (mm) were plotted for the control texture (C, 0.0 mm; light gray, dotted), a horizontal bar texture with a channel width of 0.2 mm (dark gray, dashed), and a horizontal bar texture with a channel width of 1.0 mm (black, solid). Inset: Maximum drift in the y-direction (mm) for the channel widths of 0.0, 0.2, and 1.0 mm, respectively. f) Static shear stress (kPa) for different surface texture types, given a preload of 0.98 N (100 g). g) Effect of preload (N) on the shear stress (kPa) achieved by the frictional texture. The static and dynamic shear stresses are represented as dark gray and light gray, respectively.

4.5 Effect of Patterned Silicone Tape on Fluid Channeling and Shear Adhesion

4.5.1 Experimental Methodology

A universal testing machine recorded the load resulting from the frictional pads when pulled in shear. A preload is applied to the acrylic backing and pulled in the *x*-direction along a smooth acrylic surface. The acrylic surface is coated in a layer of glycerol to approximate the contributions of secretions in the experimental setup. The tested patterns were as follows: Square (S), inverted square (Si), hexagon pulled horizontally (Hh), hexagon pulled vertically (HV), wave pulled horizontally (WH), wave pulled vertically (WV), wave and concentric circles (Wa), dots (D), and control (C). All feature sizes are 3 mm and channel width of 0.8 mm.

4.5.2 Results

To understand the limitations of our anchoring approach, we tested a variety of patterns to channel fluid, some based on existing literature and some based on patterns seen in nature. We were primarily concerned with the static shear stress as a function of pattern design and preload. In Fig. 4.4D, we investigate the effect that changing feature size and channel width has on the static shear stress. For the bar patterned pulled horizontally, we observed lower shear resistance for small and large feature sizes. For small feature sizes, we expected good fluid channeling, but had less of the silicone in contact with the acrylic surface. For large features (F = 4 mm), we expected the fluid channeling to happen more slowly. For these samples with 0.2 mm channels (F = 4 mm, C = 0.2 mm), they experienced poorer fluid channeling as compared to the sample with 1 mm channels. On the other hand, for small feature sizes (F = 1 mm), the sample with a 0.2 mm channel width performed somewhat better than the sample with 1 mm channel width. For both of these samples, we either saw a maximum (at F = 3 mm for C = 0.2 mm) or could predict a maximum (at F = 2.5 mm for C = 1 mm). Assuming that the other etched patterns followed a similar trend of the relationship between fluid channeling and available contact area allowed us to choose a set feature and channel width to compare performance across patterns (F = 3 mm, C = 0.8 mm).

We compared the static transverse shear stress for our selected patterns (see Fig. 4.4F). As anticipated, the control had a shear stress near zero, as no fluid channeling occurred in the non-patterned design. The dot pattern (D) also had a low static transverse shear stress. This was expected as the pattern was not fully connected to the edges of the sample, limiting the potential for fluid channeling. We observed that changing the direction of pulling for (H) and (W) patterns did not significantly affect the measured shear stress. However, adding additional concentric circle patterns to the wave pattern (W to W+) showed minor improvement for the channel and feature sizes tested. We saw a dramatic difference between the measured shear stress for the square (S) and the inverted square (Si). The (Si) pattern was similar to the dot pattern in that each of the etched channels in the pattern was isolated from the others, preventing fluid channeling and resulting in low static shear stress. The (S) pattern performed the best over all of the tested patterns, providing a static shear stress of approximately 1.1 kPa.

Figure 4.4G compares static and dynamic shear stress as a function of preload for the (S) pattern. We observed a monotonic increase in static shear stress as preload increased; at no preload the shear stress dropped to zero for both static and dynamic measurements. For all preloads, we observed that the static shear stress was larger than the dynamic shear stress.

We also considered how long it took for fluid to be channeled away from the silicone-acrylic interface, which we visualized by the drift, or movement away from the pulling force, vs. test extension. The control pattern (unpatterned tape) experienced drift in y over the full extension in x (Fig. 4.4E). The channel size also affected the speed of fluid channeling. The 1 mm channel size sample experienced no drift, indicating that fluid channeling happened almost immediately, whereas the sample with 0.2 mm channel size showed only 7 mm of drift before the drift stopped. In this case, we saw the sample starting to get pulled back in line with the direction of extension.

4.5.3 Discussion

For successful retraction, it is critical to assess whether the device itself deforms as well as relative movement of the whole device within the abdominal cavity (i.e. sliding due to loading). We can look at Fig. 4.4G and the expected reaction forces for a given set of retractor configurations to determine the required contact area between the retractor and the abdominal wall to withstand the reaction forces the device would experience. The forces experienced by the device during retraction can be resolved into local normal and transverse forces where the retractor comes into contact with the abdominal wall. As long as the friction between the abdominal wall exceeds the transverse loading, the device will stay in a fixed location.

$$\sigma_{static}(F_n)A_{contact} \leq F_t \tag{4.2}$$

where F_n is the preload imposed by the reaction forces, $A_{contact}$ is the total contact area between the retractor and the abdominal wall, and F_t is the transverse loading imposed by the reaction forces.

4.6 Effect of Taper Angle on Removal Force and Induced Folding

During an iterative series of tests with surgeons, we noticed that it was very difficult to remove the device after it was deployed into the abdominal cavity. We thus explored a variety of active and passive solutions to get the retractor to return to a compact shape for removal.

4.6.1 Experimental Methodology

Six samples with different taper angles were tested (Fig. 4.5). Taper angle was measured with respect to the end of the central chamber with 180 degrees corresponding to no taper. Sections were filled with shim stock internal layers to achieve a specific thickness. A 3D printed 12 mm trocar was attached to a brushless direct current (BLDC) motor via a timing belt. Rather

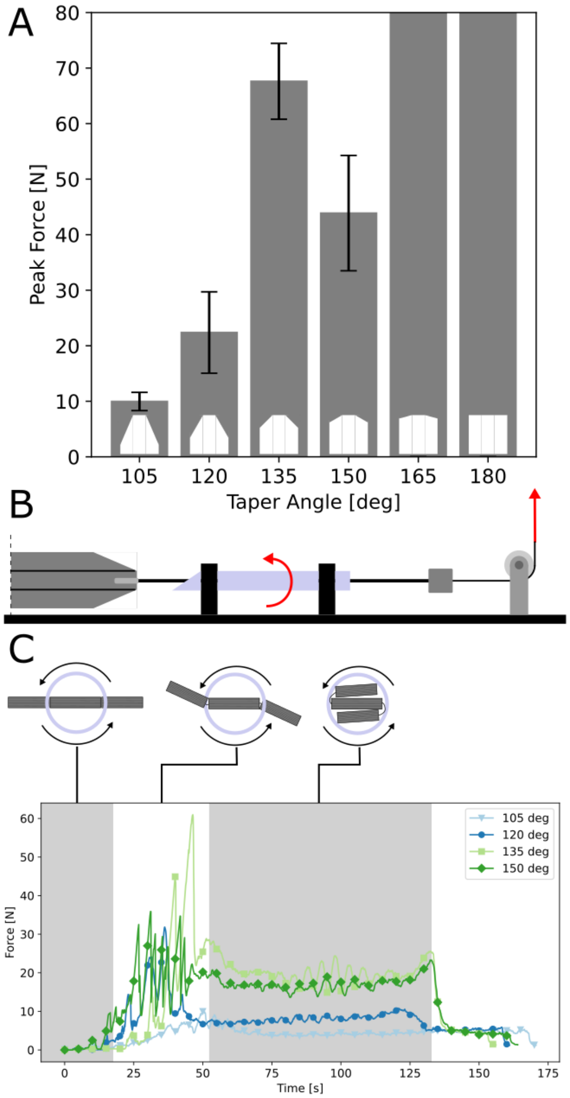

Figure 4.5. Quantification of Effect of Taper Angle on Removal of Device (A) The peak force required to pull the device through a trocar is measured as a function of taper angle. Average values across three trials are plotted with error bars indicating the standard deviation. Samples with 165 deg and 180 deg tapers were not able to pass through the trocar. (B) Schematic of experimental setup. A 3D printed trocar was rotated at a speed of 0.1 rev/s while a retractor was pulled through the trocar at a rate of 1 mm/s. A BLDC motor controlled the rate of trocar rotation while the retractor was pulled using a mechanical testing machine. (C) Representative timeseries of pull tests for each taper angle. Peak force is observed right before the device transitions from partially folded to fully folded.

than rotating the retractor (as we observed surgeons doing intuitively during removal), we chose to rotate the trocar itself. Rotation of the trocar rather than the sample device was experimentally more straightforward and consistent. The trocar was rotated at a rate of 0.1 rev/s to reduce the likelihood of dynamics affecting our measurement. The center section of the device was clamped with a modified double-action atraumatic laparoscopic grasper, which was pulled along a rail via a universal mechanical testing machine at a rate of 1 mm/s (Fig. 4.5B). We measured the force vs time and performed the test until the device had fully passed through the trocar. These tests were performed dry, with no lubricating fluid. Our primary goal with these tests was to better understand what caused the device to not be successfully removed. We anticipated removal to depend on taper angle as well as rotation and extension speed, but we were unsure how important these factors were. We were also curious to see when during removal failure would occur and how much pulling force a surgeon would need to exert.

4.6.2 Results

Our results showed that the geometry of the end of the device had a large effect on the ability of the device to self-fold during retraction, and thus on the force required to remove the device. Of the six taper angles tested, only the four steepest were able to successfully pass through the trocar. For taper angles of 165 deg and 180 deg (no taper) the device was not able to self-fold, and the resultant force caused the laparoscopic tool to lose its grip. In the annotated plot of force over time in Fig 4.5C, we saw that the device started in a flat state. A peak force occurred while the device was no longer flat but not completely self-folded. Once the device folded, the measured force dropped dramatically across all tapered designs. An additional and final drop occurred once the device exited the trocar. One unexpected result that we observed for the 135 and 150 deg taper was that the force after induced folding had occurred was higher on average than that experienced by the retractors with the 105 and 120 deg tapers. We observed relatively large variation in peak force within each sample, which we attribute to the stochastic nature of the varying contact between the trocar and the sample. In spite of the inherent stochasticity, we noted qualitative similarities in how the devices behaved at key times across all tests.

4.6.3 Discussion

We qualitatively found that while the rate of rotation was not important for our extension speed (1 mm/s), some rotation was necessary. When we fixed the trocar in place, no significant folding behavior occurred and the grasper lost it's grip on the device. While most of the taper angles were able to pass through the trocar, the measured peak force for the shallower taper angles (135° and 150°) was very high. Even though we expect the peak forces to be lower in general for surgery, as the device would likely get covered in bodily secretions, forces on the order of 40 N seem impractical. There is likely some dependence on the type of grasper chosen. If the side sections end up overlapping significantly with the grasper, we anticipate this could hinder both the ability of the device to self-fold, effectively increasing the cross-section of the retractor at the point of overlap. We observed a steady-state difference between the measured forces for 135 and 150 deg taper vs 105 and 120 deg taper. We hypothesize that the higher force could be attributed to a difference in how much induced folding occurred or how well the fold gets propagated down the length of the device.

4.7 Conclusions and Avenues for Future Work

In this work, we investigated the novel application of origami-inspired device to retraction in laparoscopic surgery. While previous work has investigated using layer jamming [92] for similar surgical use cases, it focused on the capability of the device to perform retraction during the operation. While soft and variable stiffness systems can provide some key advantages over rigid surgical tools, none of the previous work addressed the intrinsic challenges and limitations imposed by getting such a device into and out of a patient's body. In the present work, we have shown that the geometric constraints of the trocar necessitate a folding approach for a layer jamming device that leaves little room for both jamming and secondary actuation. With the overall goal of improving the capabilities of surgeons while minimizing trauma, we investigated how to atraumatically anchor our self-folding layer jammed retractor within the body. To this end, we leveraged inspiration from biological systems as well as the inherent compliance in the underlying structure to develop a novel anchoring solution that has the potential to reduce trauma as compared to other proposed soft robotic approaches.

A hallmark of soft robotic systems is the tight integration of actuation, structure, and sensing. Questions about geometry, material choice, and fabrication method have to be answered in concert and a single design element performs multiple different functions. We found that adding a taper to the end our our device, enabled the retractor to fold back to it's undeployed shape when pulled against the beveled end of a trocar. Rather than adding internal actuation, which would limit the amount of space we could devote to jamming layers, removing material from the device enabled a whole new behavior.

In this work, we focused on the retraction of the liver as it is the largest internal organ in the body and thus pushed the load bearing capabilities of our device to its limits. However, there is nothing in the design of our device that especially targets the liver. We anticipate that as long as the surgical team has a clear idea of viable anchoring points in the abdominal cavity, this device could be used in a much wider variety of laparoscopic procedures.

In future work, a better estimate of the liver's load on the device would be useful. We assumed that the device was loaded at its center point and the weight of the liver was equal on either side. Further tests of the device with liver phantoms in high-fidelity surgical simulators or in cadaver models would give us a much better sense of the performance of the device. In our model, we did not account for the fact that the patient is usually placed in a steep reverse Trendelenburg position during operations such as laparoscopic sleeve gastrectomy [102], which would change the direction of loading, of the liver, on the retractor. As far as anchoring and pattern design goes, future work should investigate how substrates with different stiffness (matched to what we expect to see in the human body), affect the static shear stress. Also it would be valuable to assess how stable different patterns are to twisting loads, combined loading conditions, and adhesion to surfaces with curvature.

Chapter 4, in part is currently being prepared for submission for publication of the material. Weston-Dawkes, W.P.; Majit, M.R.A.; Sandoval, J.; Ochoa, E.; Liu, S.; Horgan, S.; Tolley, M.T. The dissertation author was the primary investigator and author of this material.

Chapter 5

Jamming Reinforced Inflatable Beams for Mobile Robotics

5.1 Introduction

Soft mobile systems face deployment challenges due to limitations related to their ability to exert or resist significant forces in their environment. The compliance of soft systems is touted as an advantage for deployment in environments where close proximity to people is unavoidable [30], for systems to be resilient to a harsh environment [31], or when traversing over highly variable terrain [32]. At the same time, their inherent flexibility can make it difficult to perform certain tasks, such as lifting or moving heavy objects [33].

Inflatable structures in particular are prone to buckling failure due to transverse and axial loads [42, 47, 48]. For inverting robots, buckling behavior can be leveraged to navigate obstacle-heavy environments [49]. However, exceeding the critical buckling load results in large deflections which can be problematic when supporting heavy payloads or when inflatable systems are used for mobile robotics [50] or manipulator arms [51]. The tendency to buckle can be mitigated by increasing the radius of a structure, increasing the internal pressure, or decreasing the overall length. However, these mitigations are not always feasible for mobile systems. Inflation pressures are limited by the size and weight of the pump, and the intrinsic material strength of the pressure vessel. Depending on the application, such as moving through cluttered environments, a beam with a large radius can be impractical. The ideal solution would be to use a flexible skin for inflatable limbs that increases in stiffness when pressurized to limit buckling.

Previous work has taken various strategies to augment soft structures with the capability to switch between soft and stiff states [34]. These strategies range from thermally driven phase changes in structural elements [35] to pneumatically controlled jamming (granular [36], fiber [37], and layer [38, 39, 40, 41] jamming). Thus, one potential approach to increasing the stiffness for soft mobile systems intended for obstacle heavy environments is incorporation of layer jamming into inflatable robots. Do *et al.*[42] incorporated jamming into everter-style robots to jam the underlying everter into a variety of configurations, but only demonstrated success in supporting relatively low loads. Shah *et al.* [43] developed jamming skins that can be formed into 3D shapes for user-specific applications or formed around soft objects for on-demand rigidity. This work did not provide much guidance for what length scales the skins would provide the most benefit, particularly relevant due to changing failure modes with length scales. Another recent work used a plastic mesh embedded in a silicone membrane to create a variable stiffness replacement for rigid robot links. In this case, the focus of their analysis was on human-robot interaction rather than mobile robotic systems [44].

Here, we present a model based on elementary beam theory to predict the scales over which jamming contributes to resilience against buckling failure. Additionally, we explore ways to leverage this approach for novel applications of mobile robotic systems. We present a novel method to fabricate a layer jamming reinforced beam to use as a variable stiffness structural element. Through both modeling and experimental methods, we investigate how failure and deflection of an inflatable beam effects the performance of both a single beam and a mobile robotic system.

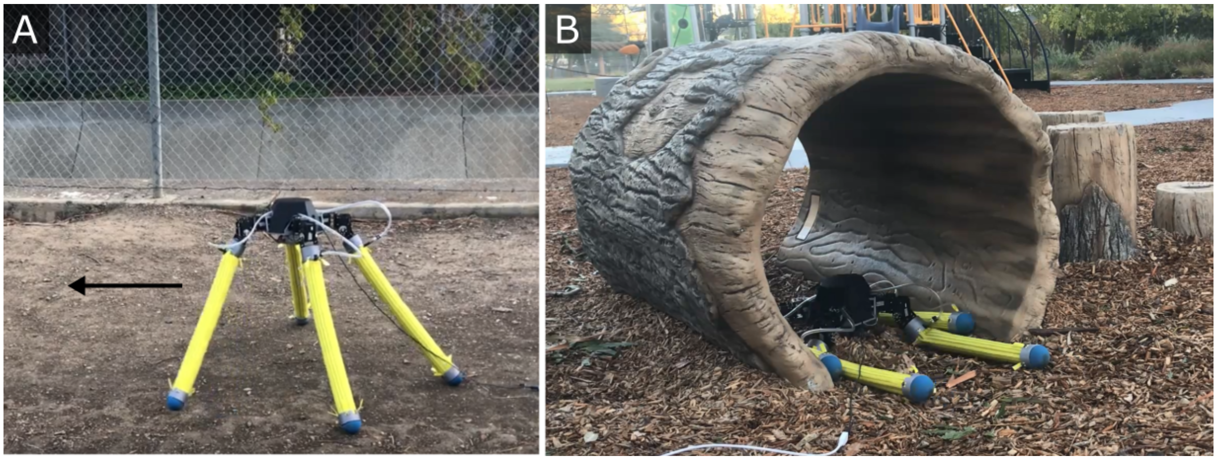

Figure 5.1. Photos of an eight-degree-of-freedom quadrupedal robotic platform with jamming-reinforced inflatable beams limbs. Layer jamming sections run longitudinally along each leg to improve the stiffness of the high-aspect ratio beams when they are pressurized without compromising the desired low-stiffness state of the deflated beams, allowing for navigation of constrained environments. (A) Legs are pressurized to provide improved locomotion speeds and better obstacle traversal capabilities. (B) Depressurizing the limbs allows the robotic system to move through environments that would be inaccessible to a larger rigid robot.

5.2 Design and Fabrication

The following sections describe the fabrication of a single, inflatable beam with layer-jamming components, as well as the implementation of the beams as legs in a quadrupedal mobile robotic system.

5.2.1 Single Beam

Inflatable limbs were fabricated from layers of Oxford fabric (200 D. Solarmax Uncoated, Seattle Fabrics Inc) and 127 micron thick textured polycarbonate film (2NJK4, Grainger) around a rubber inner tube. Each leg consisted of eight panels of fabric. The panels were sewn together to form a double-layer fabric tube with the fibers of the fabric oriented along the longitudinal and radial directions. Dividing lines along the longitudinal axis of the tube ensured that the jamming layers stayed in place during operation. We inserted a double layer of 53 - 66 mm wide bike inner tubing, cut to length, into the fabric sleeve and then fixed an internal 3D printed cap into each end of the bike inner tubing. We inserted 10 stacked 0.5 mm by 500 mm by .127 mm layers of polycarbonate film into each section between the fabric layers and added an external 3D printed cap, fastened to the fabric tube, to fully seal the bike inner tubing (Fig. 5.2). The existing Schrader valve from the bike inner tuber was used to supply pressurized air to the leg.

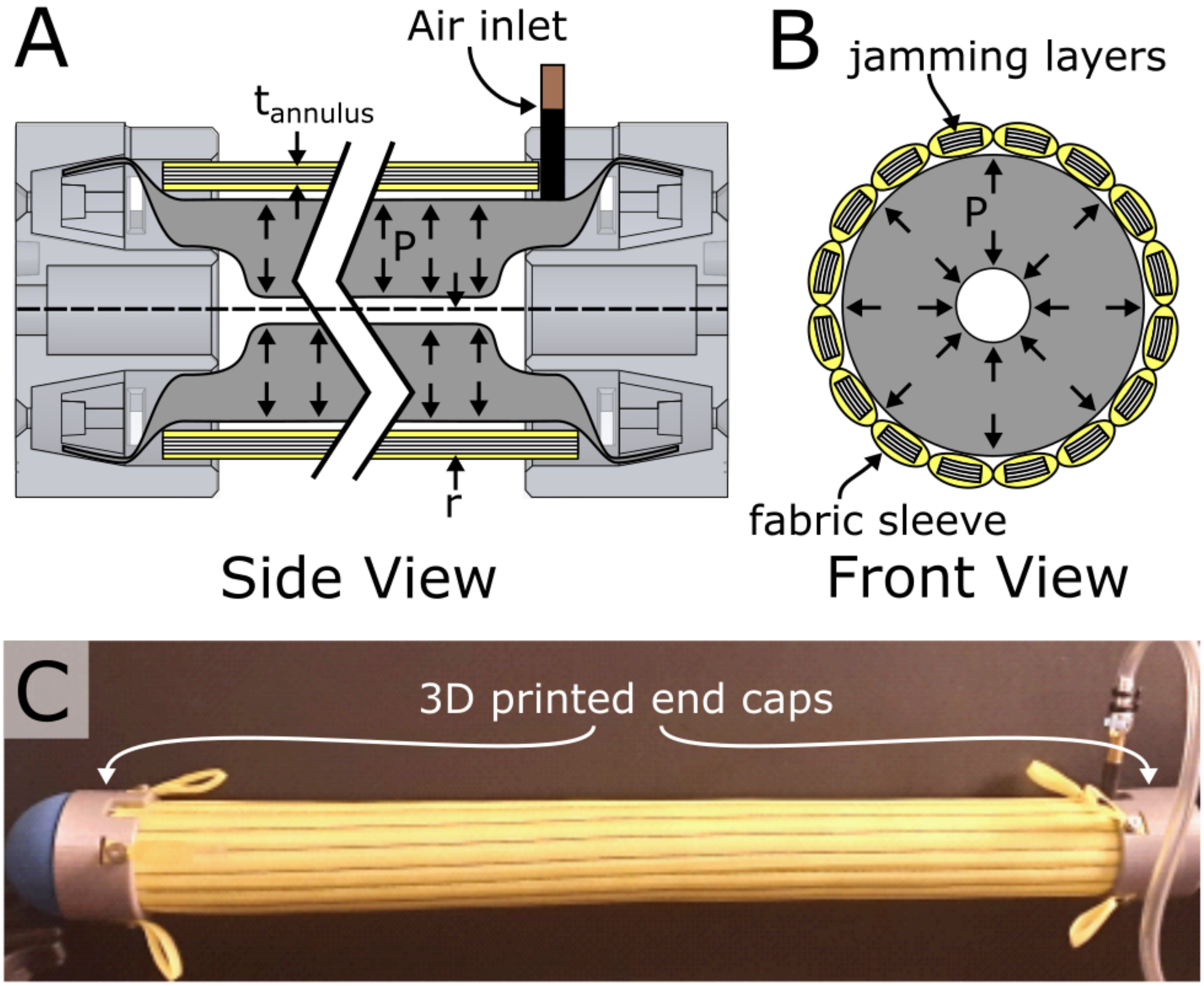

Figure 5.2. (A) Side View and (B) Front View schematic of inflatable beam: 16 sewn pouches hold longitudinally-oriented layer jamming sections consisting of 0.5 mm by 500 mm by .127 mm layers of polycarbonate film. (C) Physical instantiation of the inflatable, variable stiffness legs: threaded inserts in the 3D-printed end caps allow the beam to be fastened rigidly to an actuator at the base.

5.2.2 Mobile System

We tested the legs on a quadrupedal system to investigate how basic locomotion gaits and beam inflation affect the movement of the overall system. Each leg was controlled by two servos which actuated the swing and lift degrees of freedom (Fig. 5.3). The servos were Dynamixel MX-64T driven by an Arbotix-M microcontroller. Each servo ran off 12 V and had a stall torque of 6.4 Nm. We used the included Arduino libraries to control the mobile system via commands sent over the serial port. The legs were pressurized using an off-board air compressor. To provide contact with the ground, racquetballs were cut in half and affixed to the distal end of each leg. The full system weighed 3.6 kg.

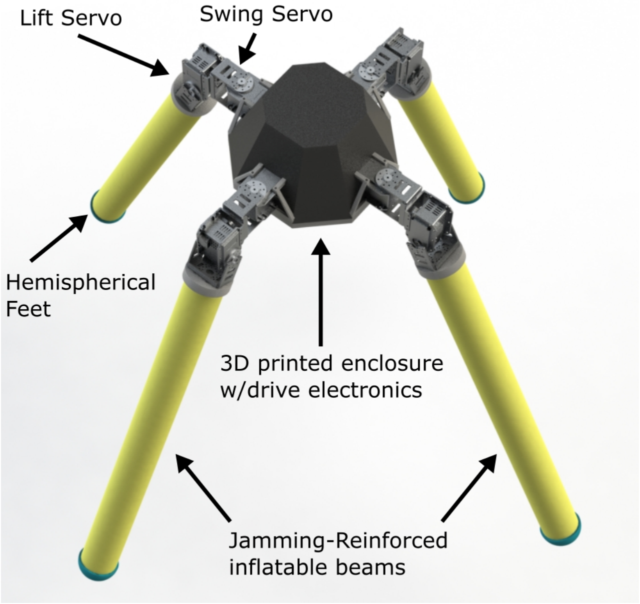

Figure 5.3. CAD render of mobile robotic system. All electronics, tubing, and power are stored in the 3D-printed base. An off-board pump provided initial inflation prior to all locomotion tests. Legs were pressurized in parallel to the same pressure. Racquetballs cut in half were used as feet.

5.3 Modeling

To determine at which length scales jamming provides the most benefit, we apply previously developed models on critical failure loads for inflatable beams and jammed layers.

5.3.1 Buckling Failure in Inflatable Beams

Substantial research attention has been devoted to developing models of cylindrical inflatable beams. These range from looking at modeling everter robots interacting with environments [103], to investigating the potential of cylindrical inflatable beams for aerospace structures [47, 48], and as low-mass robotic links [104, 51]. Here, we apply these models to investigate where jamming is most beneficial in our proposed mobile robot. For a thin-walled pressurized fabric beam, the radial loads that induce buckling failure can be predicted using the following formula [105]:

$$F_{maxradial} = \frac{\pi \Delta p r^3}{L} \tag{5.1}$$

where Δp is the pressure difference between the beam and its environment, r is the radius of the beam, and L is the length of the beam. Due to the negligible thickness of the fabric, we expect to see failure due to shear stresses rather than normal stress.

5.3.2 Jamming Failure in Annular Beams

We can also calculate the induced transverse shear stress due to radial loading of an annular beam. This calculation lets us predict the range of designs and loads for which the layer jamming skin transitions from behaving like a bulk material (i.e., with layers perfectly adhered together) to a softer material (due to the onset of slipping between the jamming layers). We refer to the latter case as “jamming failure”. For a cantilever beam loaded at the tip, the maximum induced shear stress is:

$$\tau_{max} = \frac{V_{max} Q}{bI} \tag{5.2}$$

where V_{max} is the maximum shear force in the beam, Q is the first moment of area above the neutral axis, b is the thickness of beam at the neutral axis, and I is the second moment of area for the beam. To predict the upper bound of jamming performance, we set the induced shear stress equal to the shear resistance of the jamming layers [37]:

$$\tau_{resistance} = \mu_s \Delta p = \frac{VQ}{bI} \tag{5.3}$$

where μ_s is the static friction between jamming layers. Rearranging this equation, we solve for the load that induces jamming failure:

$$F_{max\,jamming} = V = \frac{\mu_s \Delta p b I}{Q} \tag{5.4}$$

5.3.3 Critical Force Surface

To gain an intuitive sense for when failure of the layer jamming skin contributes to the failure of the beam, we want to determine the contribution of layer jamming at different length scales. To do so, we plot the two maximum forces calculated from Eqn. 5.1 and from Eqn. 5.4 for a given set of dimensional parameters (r,t,L). For a beam of a given set of dimensional parameters, we can compare the predicted maximum value from each of the two curves, which indicates which phenomena is contributing more to the overall strength of the beam (Fig. 5.4). We observe from both the previous equations that both of these effects (inflation and jamming) scale linearly with the gage pressure. For this analysis, the internal pressure is assumed to be constant ($\Delta P = 100$ kPa). The maximum force before jamming failure starts is linearly dependent on μ_s, thus for ease of scaling these results to different layer materials we assume the static coefficient of friction of the jamming layers to be a constant value of $\mu_s = 1$. We assume the additional loading provided by the mass of the jamming layers is negligible.

For a slimmer beam ($r = 2.5$ cm), shown in Fig. 5.4A, jamming becomes the dominant strengthening phenomena starting at approximately $L = 0.5$ m for a beam annulus thickness of $t = 1.27$ mm. Increasing the thickness of the annulus means that jamming contributed more at shorter lengths and decreasing the thickness to $t = 0.5$ mm means that jamming is not expected to contribute equivalently to the strength of the beam until $L = 1.4$ m. For wider beams ($r = 5$ cm), shown in Fig. 5.4B, the significance of the contribution of jamming layers is much less. However, for longer beams jamming provides a lower bound on the strength. For wide short beams, jamming provides negligible additional stiffness above that provided by inflation. We predict that incorporating jamming layers into inflatable beams could be valuable for cases when you want a long slender beam that needs to support loads on the order of 10^1 N.

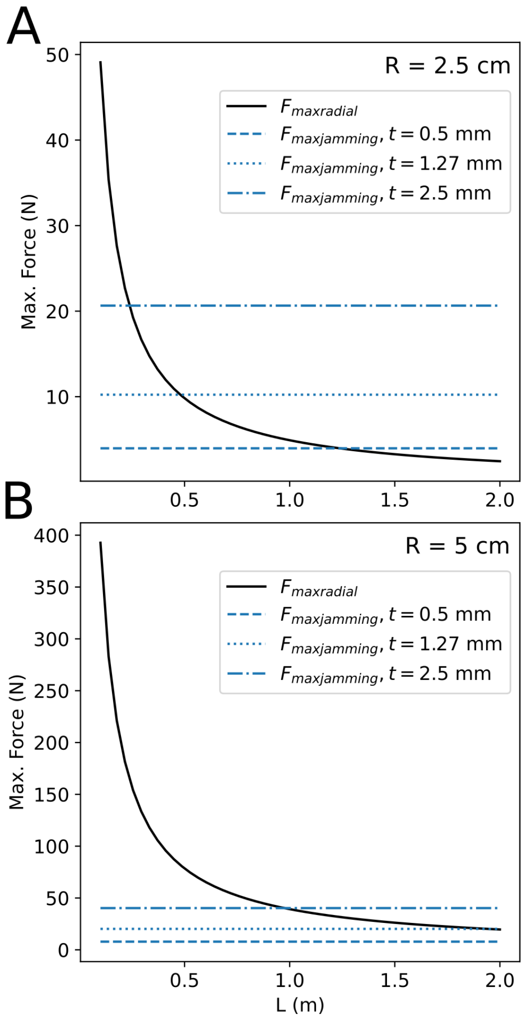

Figure 5.4. The total maximum force a jamming reinforced inflatable beam is assumed to be the superposition of Eqn. 5.1 and Eqn. 5.4. Here we compare the relative contribution of jamming with respect to the inherent strength of an inflatable beam. Where $F_{maxradial}$ intersects with $F_{maxjamming}$, we expect both effects to contribute equally (1:1) to the strength of the beam. We perform this comparison for annular beams of varying length, thickness, radii, 2.5 cm (A) and 5 cm (B). The static friction coefficient is assumed to be 1 ($\mu_s = 1$) and the gage pressure to be 100 kPa ($\Delta P = 100 * 10^3$ Pa).

Below the upper limit on the jamming force, we expect the beam to behave elastically; any subsequent force induces plastic deformation behavior as the jamming layers dissipate energy as they slide past each other[37]. Since this deformation occurs as the result of shifting internal layers, the beam can be reset to its original state by deflating and re-inflating the structure. We anticipate that the onset of jamming failure is not necessarily indicative of buckling failure. We expect that by incorporating layers, we change the deformation behavior from buckling to a more gradual deflection as the beam plastically deforms.

5.4 Experimental Results and Discussion

Results are presented for the investigation of the performance of a single beam as well as implementation in a mobile robotic system.

5.4.1 Single Beam Experiments

Verification of positive pressure jamming

To verify the positive pressure-based layer jamming, we performed a three-point bending test where we compared an inflated beam with and without jamming layers (Fig. 5.5). We applied 15 mm of quasi-static displacement via a mechanical testing machine and measured resulting force. Stiffness was calculated as the average of the slope of the force-deflection curve. As we increased the internal pressure, we observed an increase in the difference of measured stiffness between the beam with layers and the beam without layers. This result makes sense as we expect jamming failure to onset at higher forces for increased internal pressures.

Cantilever Comparison

In this experiment (Fig. 5.6), we assessed whether including jamming layers had a appreciable effect on the buckling behavior of a statically loaded inflatable cantilever beam. When buckling failure occurs, we anticipate a dramatic increase in the measured deflection, indicating a catastrophic failure. We performed this test by hanging set weights off the tip of a 25 cm long cantilever beam, $r = 2.5$ cm, with and without layers, at two different values of Δp. For this geometry of inflatable beam, we expect buckling to onset at approximately 5 N for $\Delta p = 50$ kPa and 10 N for $\Delta p = 100$ kPa.

We observed experimentally that the incorporation of jamming layers did not prevent

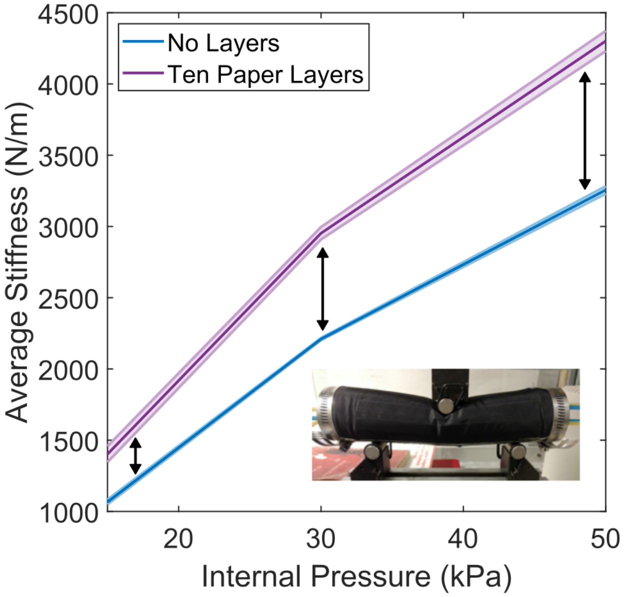

Figure 5.5. Stiffness vs internal pressure, measured with a three-point loading test (Beam dimensions: $L = 15$ cm, $r = 5$ cm).

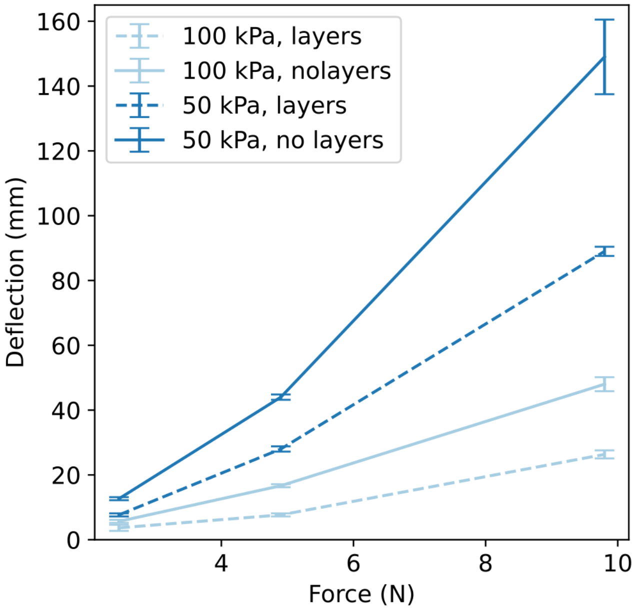

Figure 5.6. Deflection of an inflatable cantilevered beam (L = 25 cm, r = 2.5 cm) with respect to changes in load, internal pressure, and presence of jamming layers. For each condition three trials were performed (n = 3); error bars indicate standard deviation.

large deflections (Fig. 5.6). At 50 kPa with a 10 N load, the tip deflected nearly 160 mm in total, which is representative of the typical buckling behavior for inflated fabric beams. By incorporating layers, we still saw a relatively large deflection of approximately 80 mm at a 10 N load. Similarly at 5 N and 50 kPa, we observed a twofold decrease in deflection as compared to the cases with and without layers. This trend appears to also hold at higher pressures, but with lower overall deflections.

These results indicate that we were not able to prevent buckling failure merely by incorporating jamming layers; however, we *were* able to provide a significant decrease in the total deflection. By incorporating jamming layers, we allowed jamming-reinforced beams to experience a more graceful failure rather than a drastic buckling failure.

This characteristic shift in how the beam deforms under load could be particularly useful for a robotic system carrying sensitive payloads on a mobile platform over uneven terrain. For instance, if strain sensing were incorporated into the legs, the onset of buckling failure could be detected before it failed catastrophically, allowing the robot to change its gait or the loading on the legs to avoid future failures.

5.4.2 Locomotion Demonstration

Gait Selection

We chose a diagonal couplet gait inspired by the locomotion of chelonians[106]. This gait has been found to be an efficient method of locomotion for quadrupeds with slow actuation speeds or without additional actuation at the ankles. The legs move in opposite pairs with a 36 degree phase offset between the front and back legs (Fig. 5.7). Each leg moves for 40% of the gait cycle. The left foreleg moves at the start of the gait; after 10% of the gait cycle, the right rear leg starts moving. At 50% of the gait cycle, the first couplet stops and the second couplet consisting of the right foreleg and and left rear leg starts. At one point in the gait, only two feet are on the ground meaning that this gait is not stable; however, the arrangement of legs ensures that the robot will simply pitch forward through a relatively small angle onto a foot that is in the

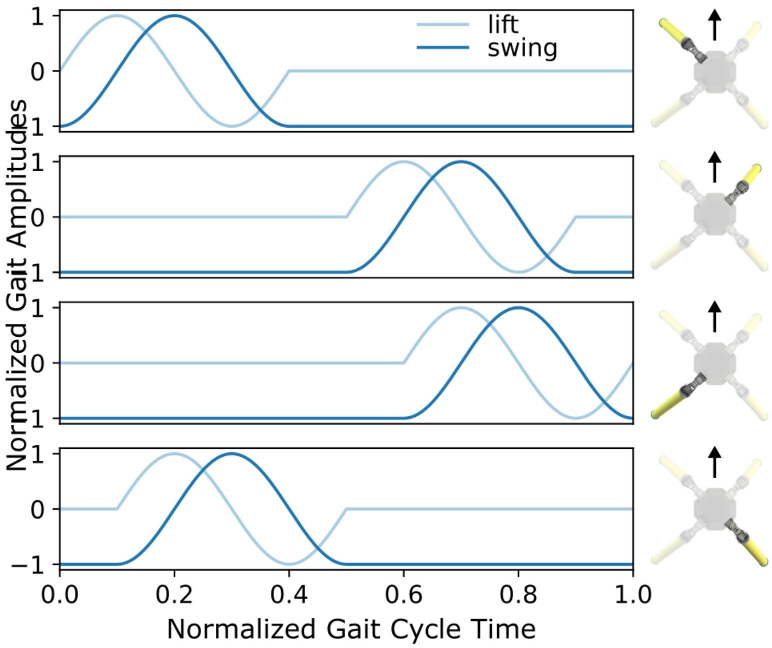

Figure 5.7. Position vs time for each limb over one gait cycle. A diagonal couplet gait was used to test the locomotion capabilities of the mobile robot. Position control of a sinusoidal trajectory was used to control the servos.

air.

Locomotion with Pressurized Legs

For these tests the legs were pressurized to 100 kPa via an external compressor which was subsequently disconnected for untethered pneumatic operation. The gait was performed open-loop over an uneven dirt surface. We observed that the mobile system tended to only have one leg in the air at any given point in time, indicating that the system had tipped forward onto either of the forelegs during the movement of each couplet. During this test, we also observed that the legs shifted in their proximal sockets over the course of several gait cycles. This shift can be seen by comparing the relative angles of the legs between the robot at time t = 0 and t = 12 s (Fig. 5.8A). This shift resulted in the robot sinking lower to the ground over the course of the test and likely increased the relative transverse loading on the legs. Comparing the displacement between that start and the end of the test we find the locomotion speed of the mobile system to be 1 cm/s.

While there are many rigid systems at this scale that are capable of moving faster than 1 cm/s [107, 108, 109], this speed compares favorably to pneumatically actuated soft robots at this scale, which suffer from slower actuation due to longer inflation times for larger actuator volumes [110]. Although volume effects can be mitigated to a certain extent by using pumps with higher flowrate, larger pumps are not always feasible for an untethered system to carry.

Locomotion with Unpressurized Legs

For these tests, we depressurized the legs and placed the robot at the entrance of a cylindrical constriction ($r \sim 50$ cm) too small for the robot with pressurized legs to move through (Fig. 5.8B). The same chelonian-inspired gait was used. The depressurized legs were angled backwards and to the sides of the main body of the robot. Through the constriction, the robot moved at a speed of 0.6 mm/s. Prior to the test, we anticipated that dragging the deflated legs behind the total would provide no benefit. Instead, it seemed to provide some benefit via either directional friction or by pushing off the interior of the cylindrical constriction.

5.5 Conclusions

We found that incorporating jamming reinforcement into inflatable beams provided improved stiffness and graceful failure rather than the catastrophic buckling that normally characterizes inflated cylindrical beams. These benefits are achieved while maintaining low stiffness while deflated. For inflatable beams with large radii and relatively short lengths, jamming provided a pressure-dependent improvement in stiffness, but this increase was not significant as compared to the stiffness contributed by the base inflated structure. For cantilever inflatable beams with small radii and longer lengths, jamming did not prevent buckling, but rather reduced the total experienced deflection.

For the locomotion test with pressurized legs, we inflated the legs using an off-board pump. By choosing to use pneumatics to inflate the base structure rather than actuate it, we sidestepped the slower actuation speeds associated with pneumatics at large scale. If the mobile

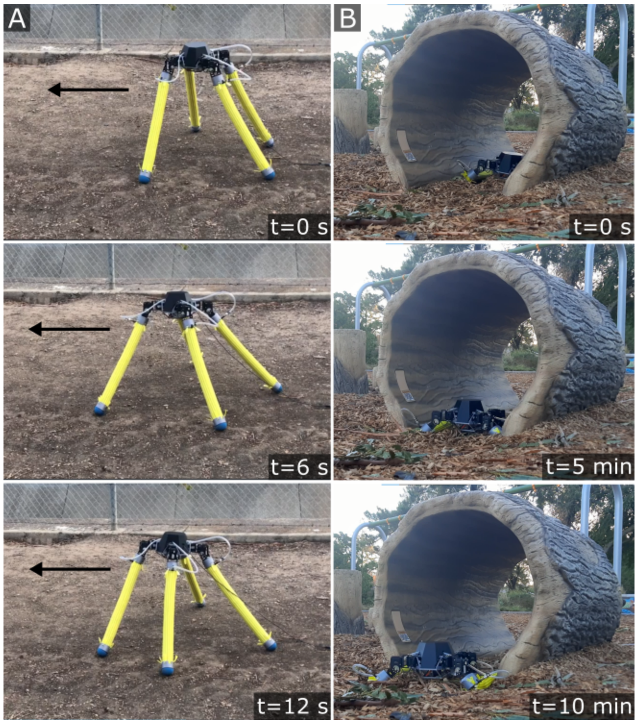

Figure 5.8. Comparison of locomotion for the pressurized and depressurized state. (A) Pressurized state moving over an uneven dirt surface (B) Depressurized state moving through an environmental constriction on a wood chip surface.

system needed to autonomously switch between an inflated and deflated state, a small onboard compressor could be added. If each leg had individual pressurized control, it could be possible to selectively deflate the legs during the swing phase of the gait to more easily pass through obstacle laden environments. By inflating or deflating the legs, we can drastically change the locomotion speed of the mobile platform.

There are several areas of potential future work for both the single inflatable beam leg and the mobile robotic system implementation. We anticipate that altering the base leg geometry to a truncated cone would delay the onset of buckling failure and improve the corresponding contribution to the stiffness from the jamming layers. As discussed previously in the results section, in certain loading cases the legs tended to shift in their sockets rather than buckle. This behavior could be mitigated by changing the method of fastening the leg to the rigid base and/or the method of fastening the actuators to the inflatable structure. Previous work has addressed this limitation in a variety of ways: incorporating cable driven actuation that anchors to the inflatable structure itself [51, 111], and inclusion a rigid collar to prevent buckling at an attachment point [50]. Adding more legs or changing the gait could also improve the base locomotion speed, change the maximum load that each leg experiences, and also open up the possibility for using extra limbs to provide balance during locomotion over uneven terrain. Treating variable stiffness structures as drop-in replacements for rigid links, while an appealing first step, does not appear to be a feasible way to design variable stiffness mobile robotic systems. Instead, we present a potential third option utilizing layer jamming to provide nuanced soft to stiff capabilities depending on the desired environment and terrain.

Chapter 5, in part, has been submitted for publication of the material as it may appear in International Design Engineering Technical Conferences & Computers and Information in Engineering Conference, 2022, Weston-Dawkes, W.P.; Tolley, M.T. The dissertation author was the primary investigator and author of this paper.

Chapter 6

Conclusions and Future Work

6.1 Conclusions

Mechanical reprogrammability allows researchers building robots the ability to incorporate multiple disparate capabilities within a single robotic system. There are many opportunities both within robotics and beyond that benefit from being able to transition from soft to hard, undeployed to deployed, or static to dynamic. Laminate manufacturing, as applied in these works, provides a fabrication methodology that applies across length scales, from several centimeters to almost a meter. Actuating laminate structures using vibration appears to have promise for low mass systems, especially if special care is taken to efficiently transfer vibrational energy to structures responsible for locomotion or adhesion. Pneumatic-based jamming techniques are inherently suited to intracorporeal use, but provide modest improvement in stiffness, limited primarily by atmospheric conditions. The maximum and minimum stiffness required for other applications will dictate the suitability of this approach.

Mechanical Customization of Self-Folding Robots

This work presented a characterization of the locomotion for a self-folding laminate bristle-bot design. The presented model provided qualitative information about velocity trends that can be used to guide the design of a heterogeneous robotic swarm. We additionally presented a self-folding technique that used an SMP actuated linear compression laminate structure to achieve consistent leg folding for an individual swarm robot.

Gas-Lubricated Vibration Adhesion in Robots

In this work, we presented and characterized a novel, controllable adhesion method for robots with high specific normal adhesive stress (i.e. $\sigma_{max}/m_{assembly} = 26.2$ KPa/Kg for our prototype system), comparable to other methods (active suction: $\sigma_{max}/m_{assembly} = 25.1$ KPa/Kg [15] and hybrid electrostatic and gecko-inspired adhesive: $\sigma_{max}/m_{assembly} = 25.7$ KPa/Kg [85]). In contrast to other controllable adhesion techniques in the literature (e.g., those based on dry fribrillar adhesives, magnetorheological fluids, or electroadhesives), the system was simple to manufacture and leveraged commercially available components to generate high specific normal adhesive stresses with low resistance to shear motion. In our experiments measuring pressure distribution, we observed that the negative pressure produced in a small central region of the vibrating disk balanced the applied load. In the experiments measuring the displacement of the disk, we saw that the delineation of the inner region and outer region approximately matched the location of the minimum fluid film thickness. Additionally, we experimentally observed that axisymmetric vibrational patterns are not a necessary condition for adhesion. We hypothesize that the flexibility of the disk allows for the formation of these nodal patterns under a relatively small excitation force, and that these nodal regions enable the generation of a small adhesive region at the center of the disk by limiting the flow of air between the inner and outer regions.

Variable Stiffness Retractor

In this work, we investigated the novel application of origami-inspired device to retraction in laparoscopic surgery. While previous work has investigated using layer jamming [92] for similar surgical use cases, it focused on the capability of the device to perform retraction during the operation. While soft and variable stiffness systems can provide some key advantages over rigid surgical tools, none of the previous work addressed the intrinsic challenges and limitations imposed by getting such a device into and out of a patient's body. In the presented work, we have shown that the geometric constraints of the trocar necessitate a folding approach for a layer jamming device that leaves little room for both jamming and secondary actuation. With the overall goal of improving the capabilities of surgeons while minimizing trauma, we investigated how to atraumatically anchor our self-folding layer jammed retractor within the body. To this end, we leveraged inspiration from biological systems as well as the inherent compliance in the underlying structure to develop a novel anchoring solution that has the potential to reduce trauma as compared to other proposed soft robotic approaches. We found that adding a taper to the end our our device, enabled the retractor to fold back to it's undeployed shape when pulled against the beveled end of a trocar. Rather than adding internal actuation, which would limit the amount of space we could devote to jamming layers, removing material from the device enabled a whole new behavior.

Jamming Reinforced Inflatable Beams

We found that incorporating jamming reinforcement into inflatable beams can provide improved stiffness and graceful failure rather than the catastrophic buckling that normally characterizes inflated cylindrical beams. These benefits were achieved while maintaing low stiffness while deflated. For inflatable beams with large radii and relatively short lengths, we found that jamming would provide a pressure-dependent improvement in stiffness, but this increase was not significant as compared to the stiffness contributed by the base inflated structure. For cantilever inflatable beams with small radii and longer lengths, we found that jamming would not prevent buckling, but rather would reduce the total deflection.

For the locomotion test with pressurized legs, we inflated the legs using an off-board pump. By choosing to use pneumatics to inflate the base structure rather than actuate it, we sidestepped the slower actuation speeds associated with pneumatics at large scale. If the mobile system needed to autonomously switch between an inflated and deflated state, a small onboard compressor could be added. If each leg had individual pressurized control, it could be possible to selectively deflate the legs during the swing phase of the gait to more easily pass through obstacle laden environments. By inflating or deflating the legs, we were able to drastically change the locomotion speed of the mobile platform.

6.2 Future Work

Mechanical Customization of Self-Folding Robots

Future work will investigate how the robot structure can be tailored to a given payload or environment. For example, by increasing or decreasing the mass of the system, the resonant frequency will shift resulting in a change of peak locomotion speed. Parameters such as leg length and material can be used to keep the resonant frequency within the operating range of the motors. To better understand how these parameters affect resonant frequency, we plan to look at the frequency response of the average linear locomotion.

Better predictions of locomotion behavior could be achieved by using alternative damping and friction models. For instance, in this model we assumed viscous damping and Coulomb dry friction. Given different leg materials and surface frictions these assumptions might not hold up.

Additional work includes further developing the capability to deploy several self-folding laminate robots simultaneously and have them complete a coverage or search task with on-board sensing. We plan to investigate different wireless communication modalities, localization algorithms, and swarm control techniques as steps towards this goal.

Gas-Lubricated Vibration Adhesion in Robots

Further work remains to be done to fully quantify the effects of surface roughness and curvature on adhesion. To allow for this adhesion technique to support larger loads for applications such as warehouse fulfillment or in-home automation, a better understanding of the scalability of this effect with the size and number of adhesive disks is needed.

This phenomena bears similarity to near-field ultrasonic levitation [112, 113], where rigid materials can be supported with high-frequency vibrations. We anticipate that much of the work done to fine-tune the performance of ultrasonic systems[114, 115] could be leveraged when designing mobile systems with flexible disks.

Variable Stiffness Retractor

In this work, we focused on the retraction of the liver as it is the largest internal organ in the body and thus pushed the load bearing capabilities of our device to its limits. However, there is nothing in the design of our device that especially targets the liver. We anticipate that as long as the surgical team has a clear idea of viable anchoring points in the abdominal cavity, this device could be used in a much wider variety of laparoscopic procedures.

In future work, a better estimate of the liver's load on the device would be useful. We assumed that the device was loaded at its center point and the weight of the liver was equal on either side. Further tests of the device with liver phantoms in high-fidelity surgical simulators or in cadaver models would give us a much better sense of the performance of the device. In our model, we did not account for the fact that the patient is usually placed in a steep reverse Trendelenburg position during operations such as laparoscopic sleeve gastrectomy [102], which would change the direction of loading, of the liver, on the retractor. As far as anchoring and pattern design goes, future work should investigate how substrates with different stiffness (matched to what we expect to see in the human body), affect the static shear stress. Also it would be valuable to assess how stable different patterns are to twisting loads, combined loading conditions, and adhesion to surfaces with curvature.

Jamming Reinforced Inflatable Beams

There are several areas of potential future work for both the single inflatable beam leg and the mobile robotic system implementation. We anticipate that altering the base leg geometry to a truncated cone would delay the onset of buckling failure and improve the corresponding contribution to the stiffness from the jamming layers. As discussed previously in the results section, in certain loading cases the legs tended to shift in their sockets rather than buckle. This behavior could be mitigated by changing the method of fastening the leg to the rigid base and/or the method of fastening the actuators to the inflatable structure. Previous work has addressed this limitation in a variety of ways: incorporating cable driven actuation that anchors to the inflatable structure itself [51, 111], and inclusion a rigid collar to prevent buckling at an attachment point [50]. Adding more legs or changing the gait could also improve the base locomotion speed, change the maximum load that each leg experiences, and also open up the possibility for using extra limbs to provide balance during locomotion over uneven terrain. Treating variable stiffness structures as drop-in replacements for rigid links, while an appealing first step, does not appear to be a feasible way to design variable stiffness mobile robotic systems. Instead, we present a potential third option utilizing layer jamming to provide nuanced soft to stiff capabilities depending on the desired environment and terrain.

Bibliography

[1] S. Felton, M. Tolley, E. Demaine, D. Rus, and R. Wood, "A method for building self-folding machines," *Science*, vol. 345, no. 6197, pp. 644–646, 2014.

[2] M. T. Tolley, S. M. Felton, S. Miyashita, L. Xu, B. Shin, M. Zhou, D. Rus, and R. J. Wood, "Self-folding shape memory laminates for automated fabrication," in *Intelligent Robots and Systems (IROS), 2013 IEEE/RSJ International Conference on*, pp. 4931–4936, IEEE, 2013.

[3] A. M. Hoover, E. Steltz, and R. S. Fearing, "Roach: An autonomous 2.4 g crawling hexapod robot," in *Intelligent Robots and Systems, 2008. IROS 2008. IEEE/RSJ International Conference on*, pp. 26–33, IEEE, 2008.

[4] S. M. Felton, M. T. Tolley, C. D. Onal, D. Rus, and R. J. Wood, "Robot self-assembly by folding: A printed inchworm robot," in *Robotics and Automation (ICRA), 2013 IEEE International Conference on*, (Karlsruhe, Germany), pp. 277–282, 2013.

[5] Y. Mulgaonkar, B. Araki, J.-s. Koh, L. Guerrero, D. M. Aukes, A. Makineni, M. T. Tolley, D. Rus, R. J. Wood, and V. Kumar, "The Flying Monkey : a multifunctional mesoscale robot that can run , fly , and grasp," *2016 IEEE International Conference on Robotics and Automation*, pp. 4672–4679, 2016.

[6] A. M. Mehta, D. Rus, K. Mohta, Y. Mulgaonkar, M. Piccoli, and V. Kumar, *A Scripted Printable Quadrotor: Rapid Design and Fabrication of a Folded MAV*, pp. 203–219. Cham: Springer International Publishing, 2016.

[7] M. Rubenstein, C. Ahler, and R. Nagpal, "Kilobot: A low cost scalable robot system for collective behaviors," in *Robotics and Automation (ICRA), 2012 IEEE International Conference on*, pp. 3293–3298, IEEE, 2012.

[8] P. Vartholomeos and E. Papadopoulos, "Analysis, design and control of a planar microrobot driven by two centripetal-force actuators," in *Robotics and Automation (ICRA), 2006 IEEE International Conference on*, pp. 649–654, IEEE, 2006.

[9] M. E. W. Nisser, S. M. Felton, M. T. Tolley, M. Rubenstein, and R. J. Wood, "Feedback-Controlled Self-Folding of Autonomous Robot Collectives," in *Intelligent Robots and Systems (IROS), 2016 IEEE International Conference on*, pp. 1254–1261, 2016.

[10] A. Brusell, G. Andrikopoulos, and G. Nikolakopoulos, "A survey on pneumatic wall-climbing robots for inspection," in *24th Mediterranean Conference on Control and Automation, MED 2016*, pp. 220–225, IEEE, 2016.

[11] M. P. Murphy and M. Sitti, "Waalbot: An agile small-scale wall-climbing robot utilizing dry elastomer adhesives," *IEEE/ASME Transactions on Mechatronics*, vol. 12, no. 3, pp. 330–338, 2007.

[12] T. Miyake, H. Ishihara, and T. Tomino, "Vacuum-based wet adhesion system for wall climbing robots -Lubricating action and seal action by the liquid-," *2008 IEEE International Conference on Robotics and Biomimetics, ROBIO 2008*, pp. 1824–1829, 2008.

[13] H. Yang, R. Liu, Q. Hong, and N. S. B. He, "A miniature multi-joint wall-climbing robot based on new vibration suction robotic foot," *Proceedings of the IEEE International Conference on Automation and Logistics, ICAL 2008*, no. September, pp. 1160–1165, 2008.

[14] L. P. Kalra, J. Gu, and M. Meng, "A wall climbing robot for oil tank inspection," *2006 IEEE International Conference on Robotics and Biomimetics, ROBIO 2006*, pp. 1523–1528, 2006.

[15] K. Shi and X. Li, "Vacuum suction unit based on the zero pressure difference method," *Physics of Fluids*, vol. 32, no. 1, 2020.

[16] K. Autumn, M. Sitti, Y. A. Liang, A. M. Peattie, W. R. Hansen, S. Sponberg, T. W. Kenny, R. Fearing, J. N. Israelachvili, and R. J. Full, "Evidence for van der Waals adhesion in gecko setae," *Proceedings of the National Academy of Sciences of the United States of America*, vol. 99, no. 19, pp. 12252–12256, 2002.

[17] G. Hanna and W. J. Barnes, "Adhesion and detachment of the toe pads of tree frogs," *Journal of Experimental Biology*, vol. 155, pp. 103–125, 1991.

[18] A. Carlson, S. Wang, P. Elvikis, P. M. Ferreira, Y. Huang, and J. A. Rogers, "Active, programmable elastomeric surfaces with tunable adhesion for deterministic assembly by transfer printing," *Advanced Functional Materials*, vol. 22, no. 21, pp. 4476–4484, 2012.

[19] C. Linghu, C. Wang, N. Cen, J. Wu, Z. Lai, and J. Song, "Rapidly tunable and highly reversible bio-inspired dry adhesion for transfer printing in air and a vacuum," *Soft Matter*, vol. 15, no. 1, pp. 30–37, 2019.

[20] C. Menon, M. Murphy, and M. Sitti, "Gecko inspired surface climbing robots," in *Proceedings - 2004 IEEE International Conference on Robotics and Biomimetics, IEEE ROBIO 2004*, pp. 431–436, 2004.

[21] P. Glick, S. A. Suresh, D. Ruffatto, M. Cutkosky, M. T. Tolley, and A. Parness, "A Soft Robotic Gripper with Gecko-Inspired Adhesive," *IEEE Robotics and Automation Letters*, vol. 3, no. 2, pp. 903–910, 2018.

[22] H. Marvi, Y. Han, and M. Sitti, “Actively controlled fibrillar friction surfaces,” *Applied Physics Letters*, vol. 106, no. 5, 2015.

[23] E. W. Hawkes, E. V. Eason, D. L. Christensen, and M. R. Cutkosky, “Human climbing with efficiently scaled gecko-inspired dry adhesives,” *Journal of the Royal Society Interface*, vol. 12, no. 102, 2015.

[24] S. Song, D. M. Drotlef, J. Paik, C. Majidi, and M. Sitti, “Mechanics of a pressure-controlled adhesive membrane for soft robotic gripping on curved surfaces,” *Extreme Mechanics Letters*, vol. 30, 2019.

[25] A. Saunders, D. I. Goldman, R. J. Full, and M. Buehler, “The RiSE climbing robot: body and leg design,” in *Unmanned Systems Technology VIII* (G. R. Gerhart, C. M. Shoemaker, and D. W. Gage, eds.), vol. 6230, pp. 401 – 413, SPIE, 2006.

[26] S. Kim, M. Spenko, S. Trujillo, B. Heyneman, V. Mattoli, and M. R. Cutkosky, “Whole body adhesion: Hierarchical, directional and distributed control of adhesive forces for a climbing robot,” *Proceedings - IEEE International Conference on Robotics and Automation*, no. April, pp. 1268–1273, 2007.

[27] M. P. Murphy, C. Kute, Y. Mengüç, and M. Sitti, “Waalbot II: Adhesion recovery and improved performance of a climbing robot using fibrillar adhesives,” *International Journal of Robotics Research*, vol. 30, no. 1, pp. 118–133, 2011.

[28] Y. Chen, N. Doshi, and R. Wood, “Inverted and inclined climbing using capillary adhesion in a quadrupedal insect-scale robot,” *IEEE Robotics and Automation Letters*, vol. 5, no. 3, pp. 1–1, 2020.

[29] J. K. Langowski, D. Dodou, M. Kamperman, and J. L. van Leeuwen, “Tree frog attachment: Mechanisms, challenges, and perspectives,” *Frontiers in Zoology*, vol. 15, no. 1, pp. 1–21, 2018.

[30] T. Kim, J. Park, S. J. Yoon, D. H. Kong, H.-W. Park, and Y.-L. Park, “Design of a lightweight inflatable sensing sleeve for increased adaptability and safety of legged robots,” in *2019 2nd IEEE International Conference on Soft Robotics (RoboSoft)*, pp. 257–264, 2019.

[31] M. T. Tolley, R. F. Shepherd, B. Mosadegh, K. C. Galloway, M. Wehner, M. Karpelson, R. J. Wood, and G. M. Whitesides, “A Resilient, Untethered Soft Robot,” *Soft Robotics*, vol. 1, no. 3, pp. 213–223, 2014.

[32] D. Drotman, M. Ishida, S. Jadhav, and M. T. Tolley, “Application-driven design of soft, 3-d printed, pneumatic actuators with bellows,” *IEEE/ASME Transactions on Mechatronics*, vol. 24, no. 1, pp. 78–87, 2019.

[33] C. Laschi, B. Mazzolai, and M. Cianchetti, “Soft robotics: Technologies and systems pushing the boundaries of robot abilities,” *Science Robotics*, vol. 1, no. 1, pp. 1–12, 2016.

[34] L. Wang, Y. Yang, Y. Chen, C. Majidi, F. Iida, E. Askounis, and Q. Pei, "Controllable and reversible tuning of material rigidity for robot applications," *Materials Today*, vol. 21, no. 5, pp. 563–576, 2018.

[35] A. Firouzeh, M. Salerno, and J. Paik, "Stiffness Control with Shape Memory Polymer in Underactuated Robotic Origamis," *IEEE Transactions on Robotics*, vol. 33, no. 4, pp. 765–777, 2017.

[36] E. Brown, N. Rodenberg, J. Amend, A. Mozeika, E. Steltz, M. R. Zakin, H. Lipson, and H. M. Jaeger, "Universal robotic gripper based on the jamming of granular material," *Proceedings of the National Academy of Sciences*, vol. 107, no. 44, pp. 18809–18814, 2010.

[37] S. Jadhav, M. R. A. Majit, B. Shih, J. P. Schulze, and M. T. Tolley, "Variable Stiffness Devices Using Fiber Jamming for Application in Soft Robotics and Wearable Haptics," *Soft Robotics*, vol. 00, no. 00, pp. 1–14, 2021.

[38] Y. S. Narang, J. J. Vlassak, and R. D. Howe, "Mechanically Versatile Soft Machines through Laminar Jamming," *Advanced Functional Materials*, vol. 28, no. 17, 2018.

[39] I. Choi, N. Corson, L. Peiros, E. W. Hawkes, S. Keller, and S. Follmer, "A Soft, Controllable, High Force Density Linear Brake Utilizing Layer Jamming," *IEEE Robotics and Automation Letters*, vol. 3, no. 1, pp. 450–457, 2018.

[40] J. Ou, L. Yao, D. Tauber, J. Steimle, R. Niiyama, and H. Ishii, "jamSheets: Thin Interfaces with Tunable Stiffness Enabled by Layer Jamming," in *Proceedings of the 8th International Conference on Tangible, Embedded and Embodied Interaction - TEI '14*, pp. 65–72, 2014.

[41] Y. J. Kim, S. Cheng, S. Kim, and K. Iagnemma, "A novel layer jamming mechanism with tunable stiffness capability for minimally invasive surgery," *IEEE Transactions on Robotics*, vol. 29, no. 4, pp. 1031–1042, 2013.

[42] B. H. Do, V. Banashek, and A. M. Okamura, "Dynamically reconfigurable discrete distributed stiffness for inflated beam robots," in *2020 IEEE International Conference on Robotics and Automation (ICRA)*, pp. 9050–9056, 2020.

[43] D. S. Shah, E. J. Yang, M. C. Yuen, E. C. Huang, and R. Kramer-Bottiglio, "Jamming Skins that Control System Rigidity from the Surface," *Advanced Functional Materials*, vol. 31, no. 1, pp. 1–8, 2021.

[44] A. Stilli, H. A. Wurdemann, and K. Althoefer, "A Novel Concept for Safe, Stiffness-Controllable Robot Links," *Soft Robotics*, vol. 4, no. 1, pp. 16–22, 2017.

[45] S. Sanan, P. S. Lynn, and S. T. Griffith, "Pneumatic torsional actuators for inflatable robots," *Journal of Mechanisms and Robotics*, vol. 6, Apr. 2014.

[46] M. T. Gillespie, C. M. Best, and M. D. Killpack, “Simultaneous position and stiffness control for an inflatable soft robot,” in *Proceedings - IEEE International Conference on Robotics and Automation*, vol. 2016-June, pp. 1095–1101, IEEE, 2016.

[47] W. Fichter, “A Theory for Inflated Thin-Wall Cylindrical Beams,” tech. rep., National Aeronautics and Space Adminstration, 1966.

[48] G. Brown, R. Haggard, and B. Norton, “Inflatable structures for deployable wings,” in *16th AIAA Aerodynamic Decelerator Systems Technology Conference and Seminar*, American Institute of Aeronautics and Astronautics, May 2001.

[49] E. W. Hawkes, L. H. Blumenschein, J. D. Greer, and A. M. Okamura, “A soft robot that navigates its environment through growth,” *Science Robotics*, vol. 2, no. 8, pp. 1–8, 2017.

[50] N. S. Usevitch, Z. M. Hammond, M. Schwager, A. M. Okamura, E. W. Hawkes, and S. Follmer, “An untethered isoperimetric soft robot,” *Science Robotics*, vol. 5, no. 40, pp. 1–15, 2020.

[51] M. Takeichi, K. Suzumori, G. Endo, and H. Nabae, “Development of giacometti arm with balloon body,” *IEEE Robotics and Automation Letters*, vol. 2, no. 2, pp. 951–957, 2017.

[52] G. H. Ballantyne, “The pitfalls of laparoscopic surgery: Challenges for robotics and telerobotic surgery,” *Surgical Laparoscopy Endoscopy & Percutaneous Techniques*, vol. 12, no. 1, 2002.

[53] J. D. Raman, D. J. Scott, and J. A. Cadeddu, “Role of magnetic anchors during laparoendoscopic single site surgery and NOTES,” *Journal of Endourology*, vol. 23, pp. 781–786, May 2009.

[54] Y. Kinjo, H. Okabe, K. Obama, S. Tsunoda, E. Tanaka, and Y. Sakai, “Elevation of liver function tests after laparoscopic gastrectomy using a nathanson liver retractor,” *World Journal of Surgery*, vol. 35, pp. 2730–2738, Dec 2011.

[55] V. Vitiello, S. L. Lee, T. P. Cundy, and G. Z. Yang, “Emerging robotic platforms for minimally invasive surgery,” *IEEE Reviews in Biomedical Engineering*, vol. 6, pp. 111–126, 2013.

[56] R. J. Lang, K. A. Tolman, E. B. Crampton, S. P. Magleby, and L. L. Howell, “A Review of Thickness-Accommodation Techniques in Origami-Inspired Engineering,” *Applied Mechanics Reviews*, vol. 70, no. 1, pp. 1–20, 2018.

[57] S. M. Felton, M. T. Tolley, B. Shin, C. D. Onal, E. D. Demaine, D. Rus, and R. J. Wood, “Self-folding with shape memory composites,” *Soft Matter*, vol. 9, no. 32, pp. 7688–7694, 2013.

[58] M. T. Tolley, S. M. Felton, S. Miyashita, D. Aukes, D. Rus, and R. J. Wood, “Self-folding origami: shape memory composites activated by uniform heating,” *Smart Materials and Structures*, vol. 23, no. 9, p. 094006, 2014.

[59] A. T. Baisch, C. Heimlich, M. Karpelson, and R. J. Wood, "HAMR3: An autonomous 1.7 g ambulatory robot," *Intelligent Robots and Systems (IROS), 2011 IEEE/RSJ International Conference on*, pp. 5073–5079, 2011.

[60] J. S. Koh and K. J. Cho, "Omegabot : Biomimetic Inchworm Robot Using SMA Coil Actuator," in *International Conference on Robotics and Biomimetics*, pp. 1154–1159, 2009.

[61] S. Miyashita, S. Guitron, M. Ludersdorfer, C. R. Sung, and D. Rus, "An untethered miniature origami robot that self-folds, walks, swims, and degrades," *2015 IEEE International Conference on Robotics and Automation (ICRA)*, pp. 1490–1496, 2015.

[62] J. Lee, Y. S. Lee, and W. Park, "Vimbot: Design and control of a new magnet robot actuated by an external vibrating magnetic field," in *Robotics and Automation (ICRA), 2015 IEEE International Conference on*, pp. 5358–5363, IEEE, 2015.

[63] F. Becker, S. Börner, V. Lysenko, I. Zeidis, and K. Zimmermann, "On the mechanics of bristle-bots - modeling , simulation and experiments," in *Robotics (ISR Robotik), 2014 IEEE International Symposium on*, pp. 2–7, IEEE, 2014.

[64] L. Giomi, N. Hawley-Weld, and L. Mahadevan, "Swarming, swirling and stasis in sequestered bristle-bots," in *Proceedings of the Royal Society of London A: Mathematical, Physical and Engineering Sciences*, vol. 469, p. 20120637, The Royal Society, 2013.

[65] D. Raviv, W. Zhao, C. McKnelly, A. Papadopoulou, A. Kadambi, B. Shi, S. Hirsch, D. Dikovsky, M. Zyracki, C. Olguin, R. Raskar, and S. Tibbits, "Active printed materials for complex self-evolving deformations.," *Scientific reports*, vol. 4, p. 7422, 2014.

[66] J. Whitney, P. Sreetharan, K. Ma, and R. Wood, "Pop-up book mems," *Journal of Micromechanics and Microengineering*, vol. 21, no. 11, p. 115021, 2011.

[67] T. G. Leong, P. A. Lester, T. L. Koh, E. K. Call, and D. H. Gracias, "Surface tension-driven self-folding polyhedra," *Langmuir*, vol. 23, no. 17, pp. 8747–8751, 2007.

[68] B. An, S. Miyashita, M. T. Tolley, D. M. Aukes, L. Meeker, E. D. Demaine, M. L. Demaine, R. J. Wood, and D. Rus, "An end-to-end approach to making self-folded 3d surface shapes by uniform heating," in *Robotics and Automation (ICRA), 2014 IEEE International Conference on*, pp. 1466–1473, IEEE, 2014.

[69] D. M. Aukes, B. Goldberg, M. R. Cutkosky, and R. J. Wood, "An analytic framework for developing inherently-manufacturable pop-up laminate devices," *Smart Materials and Structures*, vol. 23, no. 9, p. 094013, 2014.

[70] X. Sun, S. M. Felton, R. Niiyama, R. J. Wood, and S. Kim, "Self-folding and Self-actuating Robots : a Pneumatic Approach," in *2015 IEEE International Conference on Robotics and Automation (ICRA)*, pp. 3160–3165, 2015.

[71] D. J. Laser and J. G. Santiago, “A review of micropumps,” *Journal of Micromechanics and Microengineering*, vol. 14, no. 6, 2004.

[72] E. Navarro, Y. Bréchet, R. Moreau, T. Pardoen, J. P. Raskin, A. Barthelemy, and I. Radu, “Direct silicon bonding dynamics: A coupled fluid/structure analysis,” *Applied Physics Letters*, vol. 103, no. 3, 2013.

[73] S. D. De Rivaz, B. Goldberg, N. Doshi, K. Jayaram, J. Zhou, and R. J. Wood, “Inverted and vertical climbing of a quadrupedal microrobot using electroadhesion,” *Science Robotics*, vol. 3, no. 25, 2018.

[74] Q. Wu, V. Pradeep, and X. Liu, “A paper-based wall-climbing robot enabled by electrostatic adhesion,” *2018 IEEE International Conference on Soft Robotics, RoboSoft 2018*, pp. 315–320, 2018.

[75] M. A. Graule, P. Chirarattananon, S. B. Fuller, N. T. Jafferis, K. Ma, M. Spenko, R. Kornbluh, and R. J. Wood, “Perching and takeoff of a robotic insect on overhangs using switchable electrostatic adhesion,” *Science*, vol. 352, no. 6288, pp. 978–982, 2016.

[76] J. Guo, T. Hovell, T. Bamber, J. Petzing, and L. Justham, “Symmetrical electroadhesives independent of different interfacial surface conditions,” *Applied Physics Letters*, vol. 111, no. 22, 2017.

[77] H. Prahlad, R. Pelrine, S. Stanford, J. Marlow, and R. Kornbluh, “Electroadhesive robots - Wall climbing robots enabled by a novel, robust, and electrically controllable adhesion technology,” *Proceedings - IEEE International Conference on Robotics and Automation*, pp. 3028–3033, 2008.

[78] V. Alizadehyazdi, M. Modabberifar, S. M. J. Mahmoudzadeh, and M. Spenko, “Electrostatic self-cleaning gecko-like adhesives,” *Journal of The Royal Society Interface*, 2018.

[79] D. Ruffatto III, A. Parness, and M. Spenko, “Improving controllable adhesion on both rough and smooth surfaces with a hybrid electrostatic/gecko-like adhesive,” *Journal of The Royal Society Interface*, vol. 11, no. 20131089, 2014.

[80] S. Wang, L. Li, Y. Chen, Y. Wang, W. Sun, J. Xiao, D. Wainwright, T. Wang, R. J. Wood, and L. Wen, “A bio-robotic remora disc with attachment and detachment capabilities for reversible underwater hitchhiking,” *Proceedings - IEEE International Conference on Robotics and Automation*, vol. 2019-May, pp. 4653–4659, 2019.

[81] J. A. Sandoval, S. Jadhav, H. Quan, D. D. Deheyn, and M. T. Tolley, “Reversible adhesion to rough surfaces both in and out of water, inspired by the clingfish suction disc,” *Bioinspiration & biomimetics*, vol. 14, no. 6, p. 066016, 2019.

[82] W. H. Banks and C. C. Mill, “Tacky adhesion-A preliminary study,” *Journal of Colloid Science*, vol. 8, no. 1, pp. 137–147, 1953.

[83] W. A. Gross, "Gas bearings: A survey," *Wear*, vol. 6, no. 6, pp. 423–443, 1963.

[84] S. Timoshenko and S. Woinowsky-Krieger, *Theory of Plates and Shells*. Engineering mechanics series, McGraw-Hill, 1959.

[85] D. Ruffatto III, P. E. Glick, M. T. Tolley, and A. Parness, "Long-Duration Surface Anchoring with a Hybrid Electrostatic and Gecko-Inspired Adhesive," *IEEE Robotics and Automation Letters*, vol. 3, no. 4, pp. 4201–4208, 2018.

[86] A. R. C. Baijon and M. Robbins, "Energy Dissipation during Rupture of Adhesive Bonds," *Science*, vol. 271, no. 5248, pp. 482–484, 1996.

[87] O. Reynolds, "On the Theory of Lubrication and Its Application to Mr. Lowe's Experiments," *Philosophical Transactions of the Royal Society of London*, vol. 177, pp. 157–234, 1886.

[88] M. D. Waller, "Vibrations of free circular plates. Part 1: Normal Modes," *Proceedings of the Physical Society*, vol. 50, no. 1, pp. 77–82, 1938.

[89] T. Ranzani, M. Cianchetti, G. Gerboni, I. D. Falco, and A. Menciassi, "A Soft Modular Manipulator for Minimally Invasive Surgery: Design and Characterization of a Single Module," *IEEE Transactions on Robotics*, vol. 32, no. 1, pp. 187–200, 2016.

[90] M. Cianchetti, T. Ranzani, G. Gerboni, T. Nanayakkara, K. Althoefer, P. Dasgupta, and A. Menciassi, "Soft Robotics Technologies to Address Shortcomings in Today's Minimally Invasive Surgery: The STIFF-FLOP Approach," *Soft Robotics*, vol. 1, no. 2, pp. 122–131, 2014.

[91] Y. J. Kim, S. Cheng, S. Kim, and K. Iagnemma, "Design of a tubular snake-like manipulator with stiffening capability by layer jamming," in *IEEE International Conference on Intelligent Robots and Systems*, pp. 4251–4256, 2012.

[92] S. Tognarelli, M. Brancadoro, V. Dolosor, and A. Menciassi, "Soft Tool for Gallbladder Retraction in Minimally Invasive Surgery Based on Layer Jamming," *Proceedings of the IEEE RAS and EMBS International Conference on Biomedical Robotics and Biomechatronics*, vol. 2018-Augus, pp. 67–72, 2018.

[93] S. Miyashita, S. Guitron, K. Yoshida, S. Li, D. D. Damian, and D. Rus, "Ingestible, controllable, and degradable origami robot for patching stomach wounds," *Proceedings - IEEE International Conference on Robotics and Automation*, vol. 2016-June, no. 5, pp. 909–916, 2016.

[94] K. P. Becker, N. W. Bartlett, M. J. D. Malley, P. M. Kjeer, and R. J. Wood, "Tunable friction through constrained inflation of an elastomeric membrane," in *2017 IEEE International Conference on Robotics and Automation (ICRA)*, pp. 4352–4357, 2017.

[95] Z. Zhakypov and J. Paik, "Design Methodology for Constructing Multimaterial Origami Robots and Machines," *IEEE Transactions on Robotics*, vol. 34, no. 1, pp. 151–165, 2018.

[96] D. Rus and M. T. Tolley, "Design, fabrication and control of origami robots," *Nature Reviews Materials*, vol. 3, pp. 101–112, Jun 2018.

[97] Y. Lin, G. Yang, Y. Liang, C. Zhang, W. Wang, D. Qian, H. Yang, and J. Zou, "Controllable Stiffness Origami "Skeletons" for Lightweight and Multifunctional Artificial Muscles," *Advanced Functional Materials*, vol. 30, no. 31, pp. 1–10, 2020.

[98] H. Banerjee, T. K. Li, G. Ponraj, S. K. Kirthika, C. M. Lim, and H. Ren, "Origami-Layer-Jamming Deployable Surgical Retractor With Variable Stiffness and Tactile Sensing," *Journal of Mechanisms and Robotics*, vol. 12, no. 3, 2020.

[99] S. Liu, M. R. A. Majit, S. Horgan, M. Tolley, W. Weston-Dawkes, and E. Ochoa, "Programmable stiffness tissue displacement device."

[100] W. Federle, W. J. P. Barnes, W. Baumgartner, P. Drechsler, and J. M. Smith, "Wet but not slippery : boundary friction in tree frog adhesive toe pads," *Journal of The Royal Society Interface*, no. May, pp. 689–697, 2006.

[101] W. C. Young and R. G. Budynas, *Roark's Formulas for Stress and Strain*, vol. 4. McGraw-Hill, seventh ed., 1980.

[102] M. M. H. Ozanan R. Meireles, Eric G. Sheu, *Operative techniques in surgery*, ch. Chapter 19: Laparoscopic Sleeve Gastrectomy. Wolters Kluwer, 2015 - 2015.

[103] J. Luong, P. Glick, A. Ong, M. S. DeVries, S. Sandin, E. W. Hawkes, and M. T. Tolley, "Eversion and retraction of a soft robot towards the exploration of coral reefs," in *RoboSoft 2019 - 2019 IEEE International Conference on Soft Robotics*, pp. 801–807, IEEE, 2019.

[104] M. Rybski, M. Shoham, and G. Grossman, "Robotic manipulators based on inflatable structures," *Robotics and Computer-Integrated Manufacturing*, vol. 12, no. 1, pp. 111–120, 1996.

[105] R. L. Comer and S. Levy, "Deflections of an inflated circular-cylindrical cantilever beam," *AIAA Journal*, vol. 1, no. 7, pp. 1652–1655, 1963.

[106] A. S. Jayes and R. M. N. Alexander, "The gaits of chelonians: walking techniques for very low speeds," *Journal of Zoology*, vol. 191, no. 3, pp. 353–378, 1980.

[107] B. G. Katz and K. Benjamin G., *A low cost modular actuator for dynamic robots*. PhD thesis, Massachusetts Institute of Technology, 2018.

[108] M. Chellapurath, S. Stefanni, G. Fiorito, A. M. Sabatini, C. Laschi, and M. Calisti, "Locomotory behaviour of the intertidal marble crab (Pachygrapsus marmoratus) supports the underwater spring-loaded inverted pendulum as a fundamental model for punting in animals," *Bioinspiration and Biomimetics*, vol. 15, no. 5, 2020.

[109] G. Picardi, M. Chellapurath, S. Iacoponi, C. Laschi, and M. Calisti, "Surveying and cleaning plastic pollution in the sediment: Silver+ approach," in *OCEANS 2019 - Marseille*, pp. 1–8, 2019.

[110] S. Li, S. A. Awale, K. E. Bacher, T. J. Buchner, C. Della Santina, R. J. Wood, and D. Rus, "Scaling Up Soft Robotics: A Meter-Scale, Modular, and Reconfigurable Soft Robotic System," *Soft Robotics*, vol. 00, no. 00, pp. 1–13, 2021.

[111] R. Qi, T. L. Lam, and Y. Xu, "Kinematic modeling and control of a multi-joint soft inflatable robot arm with cable-driven mechanism," in *2014 IEEE International Conference on Robotics and Automation (ICRA)*, pp. 4819–4824, 2014.

[112] T. Ide, J. Friend, K. Nakamura, and S. Ueha, "A low-profile design for the noncontact ultrasonically levitated stage," *Japanese Journal of Applied Physics*, vol. 44, no. 6B, pp. 4662 – 4665, 2005.

[113] T. Ide, J. Friend, K. Nakamura, and S. Ueha, "A non-contact linear bearing and actuator via ultrasonic levitation," *Sensors and Actuators, A: Physical*, vol. 135, no. 2, pp. 740 – 747, 2007.

[114] D. Koyama, T. Ide, J. Friend, K. Nakamura, and S. Ueha, "An ultrasonically levitated noncontact stage using traveling vibrations on precision ceramic guide rails," *IEEE Transactions on Ultrasonics, Ferroelectrics and Frequency Control*, vol. 54, pp. 597–604, Mar. 2007.

[115] J. Saito, J. Friend, K. Nakamura, and S. Ueha, "Resonant mode design for noncontact ultrasonic motor with levitated rotor," *Japanese Journal of Applied Physics*, vol. 44, no. 6B, pp. 4666 – 4668, 2005.